Doctoral Dissertation
Doctoral Program in Electrical, Electronics and Communications Engineering
(37$^{th}$cycle)

# Approaches for electromagnetic and loss analysis in electrical machines with superconducting AC windings

By

**Inês Santos Perdigão Peixoto**

******

**Supervisor(s):**
Prof. Silvio Vaschetto, Supervisor
Prof. João Filipe Pereira Fernandes, Co-Supervisor

**Doctoral Examination Committee:**
Prof. João Miguel Murta Pina, Referee, Universidade Nova de Lisboa
Prof. Fabrizio Marignetti, Referee, Università degli Studi di Cassino e del Lazio Meridionale

Politecnico di Torino
2025

UNIONE EUROPEA
Fondo Sociale Europeo

Ministero dell'Università
e della Ricerca

PON
RICERCA
E INNOVAZIONE
2014 - 2020

REACT EU

This doctoral thesis was written at the conclusion of the doctoral course funded under PON REACT-EU 2014-2020 - action IV.4 “Doctorates and research contracts on innovation issues” and action IV.5 “Doctorates on green issues” under Ministerial Decree of August 10, 2021, no. 1061.

La presente tesi di dottorato è stata redatta a conclusione del corso di dottorato finanziato nell’ambito del PON REACT-EU 2014-2020 - azione IV.4 “Dottorati e contratti di ricerca sui temi dell’innovazione” e azione IV.5 “Dottorati sui temi green” ai sensi del D.M. 10 agosto 2021, n. 1061.

# Declaration

I hereby declare that, the contents and organization of this dissertation constitute my own original work and does not compromise in any way the rights of third parties, including those relating to the security of personal data.

Inês Santos Perdigão Peixoto
2025

* This dissertation is presented in partial fulfillment of the requirements for **Ph.D. degree** in the Graduate School of Politecnico di Torino (ScuDo).

# Acknowledgements

I would like to express my gratitude to my supervisors, Professor Silvio Vaschetto and Professor João Filipe Pereira Fernandes, for their guidance, support, and encouragement throughout my doctoral studies. I have greatly benefited from your expertise and constructive feedback, which have been fundamental to my academic journey and the successful completion of this project. It has been a privilege to work under your supervision.

I am also sincerely thankful to Professor Naoyuki Amemiya and Professor Yusuke Sogabe at Kyoto University, who welcomed me with great generosity during my research stay abroad. Their guidance and experience have had a meaningful impact on both my research and personal growth.

My warmest thanks to my friends and colleagues, who have shared this experience with me. Your support, thoughtful conversations, and the moments we've shared along the way have made this journey all the more meaningful.

To my parents, thank you for your constant support, love, and patience. Your encouragement has sustained me through every challenge, and I am profoundly grateful for the strength and reassurance you have always given me.

Finally, I want to thank my partner for his support, understanding, and love. Your belief in me has been a source of strength and comfort, and I am endlessly grateful to have you by my side.

This achievement is not mine alone but a reflection of all those who have walked this path with me. I'm truly grateful to each of you.

# Abstract

This thesis investigates the modelling and performance estimation of high-temperature superconductors in rotating electrical machines. Conventional ferromagnetic and superconducting materials are characterized, and methodologies are developed for accurate and time-efficient finite element modelling. These calibrated models are then used to evaluate the performance of HTS coils in armature windings of electrical machines.

This work uses finite element models employing the $T-A$ formulation with the thin sheet approximation to predict the performance of coated superconductors (Rare Earth Barium Copper Oxide tapes) in different operating conditions. Experimental activities were conducted on a $2^{\text{nd}}$ generation coated superconductor to calibrate and validate the electromagnetic models. The experimental setups for AC and DC supply measurements (77 K) were investigated and constructed.

Tests with DC supply were performed to measure the non-linear resistivity characteristic of the superconductors and their transition from the superconducting to the resistive state. Under AC supply, the hysteretic behaviour and AC loss characteristics of HTS materials were observed. Material parameters from these experiments were integrated into the models to represent superconducting behaviour accurately. The experimental and simulation results were used to develop an analytical method for transport loss estimation for superconducting tapes operating in the overcritical regime ($I>I_c$) when the superconducting layer manifests resistivity and losses in the copper stabilizing layers become impactful. A 2D $T-A$ electromagnetic multi-layered tape model was also proposed to estimate the coated conductor losses. Simulation results were compared to homogenized models, as well as analytical results and experimental data, showing good agreement for transport current and magnetization loss calculations. To better describe materials in electrical machine simulations, experiments were performed in different ferromagnetic samples at ambient and cryogenic temperatures to accurately characterize the properties of ferromagnetic materials in alternate operating conditions. The results were applied to calibrate multiphysics models of ferromagnetic cores in rotating electrical machines.

The measured material characteristics were applied to the 3D model of a case-study axial flux permanent magnet machine to estimate superconductor losses. Due to the different dimensional scales and non-linearities that have to be considered when modelling superconductors in complex electromagnetic devices, the simulations are highly demanding and, therefore, incompatible with electrical machine design methodologies. Hence, the synchronous machine 3D model was used to construct a 2D model of a machine slot for faster analyses in the superconducting tapes. The model is based on replicating the machine armature slot magnetic field in a 2D environment, where the superconductor formulations are added, significantly reducing model computation time and complexity. The proposed methodology was validated through comparison with a 3D model and analytical results available in the literature. The 2D model was used to estimate losses for spiral copper-plated striated coated conductor cables, which, due to their low AC losses, high current carrying capacity and mechanical flexibility, show promise for application in electrical machines. The losses in the SCSC cables are compared to those for REBCO tapes, and their applicability in electrical machine armature windings was demonstrated by the reduced impact of external field direction on cable losses. A complementary thermal slot model was developed to estimate superconducting armature windings' cooling requirements and efficiency. An experimental setup was designed to calibrate and validate the thermal model, showing good agreement between experimental and simulation results.

# Contents

# List of Figures

# List of Tables

# List of Acronyms

| | |
|---|---|
| 1*G* | first-generation |
| 2*G* | second-generation |
| *AFPM* | Axial Flux Permanent Magnet |
| *BSCCO* | Bismuth Strontium Calcium Copper Oxide |
| *CC* | Coated Conductor |
| *CORC* | Conductor on Round Core |
| *EMs* | Electrical Machines |
| *EU* | European Union |
| *FEM* | Finite element method |
| *GdBCO* | Gadolinium Barium Copper Oxide |
| *GRFP* | Glass Fibre Reinforced Plastic |
| *HTS* | High-Temperature Superconductors |
| *LTS* | Low-Temperature Superconductors |
| *PbSCCO* | Lead Strontium Calcium Copper Oxide |
| *PUR* | polyurethane |
| *SCs* | Superconductors |

*SCSC* Spiral Copper-plated Striated Coated conductor

*YBCO* Yttrium Barium Copper Oxide

# Chapter 1

# Introduction

## 1.1 Research Background

According to the EU climate-neutral target requirements by 2050, high electricity production and usage efficiencies are critical for maximizing energy savings and minimizing greenhouse gas emissions [14, 15]. To achieve this goal, high power-to-weight ratios are essential for enabling the electrification of diverse sectors, including offshore renewable energy, transportation, and industrial processes. [16, 17]. In offshore generation, this involves the deployment of lightweight, high-capacity wind turbines and efficient energy storage systems to harness and distribute renewable energy effectively [16, 18]. In transportation, enhancing power-to-weight ratios is essential for developing electric vehicles, ensuring they are both energy-efficient and capable of meeting performance demands [19]. Hence, to reduce emissions and support the EU vision of a modern, competitive, and sustainable economy, electrical machines (EMs), a key component in industry, energy generation, and transportation sectors, must become highly efficient and power-dense.

Electric machines working at cryogenic temperatures have gathered attention for applications requiring challenging specific power values in recent years. This is particularly true if cryogenic fluids are already part of the system or are investigated as critical enabling technologies for improving the performance of the system. In cryogenic conditions, electrical resistivity decreases, and the remanent flux density of permanent magnets can increase up to 20% [20]. Besides, thanks to the enhanced heat extraction provided by the extremely low-temperature operation, cryogenic machines can achieve higher electrical loading compared to ambient temperature conditions [21]. The literature shows that conventional electrical machines working submersed in a cryogenic fluid can reduce the machine size by up to 40% compared to air-cooled designs of the same rating [22, 23].

Since very low temperatures are already a prerequisite for the superconducting state transition, applied superconductivity stands out among cryogenic applications. Superconductivity manifests in some elements and alloys, which exhibit a near-zero DC electric resistivity when operated in their superconducting state. According to their admissible operating temperature, superconductors (SCs) can be categorized as Low-Temperature Superconductors (LTS) , with operating temperatures up until 30 K and High-Temperature Superconductors (HTS) operating above the 30-35 K threshold [24].

The development of electrical equipment employing Low-Temperature Superconductors became possible in the 1960s with the discovery of $Nb_3Sn$. This material could carry high currents in the presence of high magnetic fields [25]. The very low operating temperature of LTS makes their application to energy conversion devices challenging [26]. Nonetheless, LTS materials are still used nowadays in several applications, such as magnetic fusion energy and high-energy physics accelerators [27].

The discovery of high-temperature superconductors operating above 35 K enabled overcoming the challenges associated with LTS technology, mainly related to the system complexity for such extremely low temperatures [28]. In 1987, a breakthrough was made with the discovery of $YBa_2Cu_3O_7$, Yttrium Barium Copper Oxide (YBCO), a high-temperature superconductor compound that operates above the boiling point of liquid nitrogen at 77 K [29]. The discovery of superconductors functioning well above 77 K marked a new era for electric power applications. Today, many demonstrators utilize silver-sheathed HTS conductors made of $(Bi, Pb)_2Sr_2Ca_2Cu_3O_{10}$, BSCCO, or PbSCCO, which exhibit superconductivity at temperatures up to approximately 110 K. In 2001, the $MgB_2$ binary compound was found to superconduct at 39 K. A very strong interest has grown in its use in electric applications because of its reduced production cost and easy manufacturability [30], as well as the possibility of coupling liquid $H_2$ cooling (30 K) and fuel cells in the same system. The exceptional characteristics of superconducting materials, such as their intrinsic near-zero DC resistivity and the ability to carry high currents at high magnetic field levels, can lead to a significant increase in magnetic loading. In this way, electrical machines with decreased volume and increased efficiency can be designed.

The expectation that HTS can be decisive in achieving high torque density energy conversion devices has led, in recent years, to the emergence of several research projects in superconducting machines funded by the EU. The project SUPRAPOWER developed a generator with superconducting field coils for offshore wind turbines that are 25% lighter than a conventional permanent magnet counterpart [31]. Similarly, the EcoSwing project, applying HTS on the rotor side, successfully demonstrated the first-ever 3.6 MW HTS generator for a direct-drive wind turbine [32]. ASuMED project focused on fully SC electric machines for hybrid-electric distributed propulsion for aircraft [33]. International entities, including NASA, Airbus, and Siemens, have also taken an interest in SC electric machines and funded dedicated research projects. For instance, CHEETA and STARC-ABL from NASA target electric machines for future all-electric airplanes [34, 35].

Although remarkable efforts have been made in the field of superconducting electrical machines, present-day HTS technology still faces limitations such as the non-negligible superconducting loss in time-varying conditions and material strain/bending limitations [36, 37]. Energy conversion devices such as motors, generators, and transformers operate with varying magnetic fields and currents, leading to numerous studies focused on reducing energy loss [38, 39]. Despite these efforts, the extensive work on developing superconducting machines and devising loss mitigation methods in the superconducting components emphasizes that superconducting materials have the potential to surpass the limitations of conventional materials. This could enable the creation of compact, lightweight devices with high torque and efficiency [40, 41].

## 1.2 Research Objectives

Considerable efforts have been devoted to investigating the feasibility of superconducting windings in electrical machines due to the promising characteristics of HTS materials. The application of SC materials in electrical machines can be a solution to overcome power density limits by increasing their magnetic loading and allowing lightweight or air-core typologies.

Some superconducting prototypes prioritize using HTS in field coils to leverage their near-zero DC resistivity [28, 42]. These are called partially superconducting machines, as superconductors are used only in one part of the machine circuit (i.e., the stator or rotor). However, incorporating superconductors into the rotor of electrical machines poses construction challenges, often requiring rotating cryocoolers. If superconductors are applied in the armature winding on the stator side of the machine, the cooling system can be made static, which would prove advantageous from both the construction and maintenance points of view. Alternatively, rotating electrical machines can be built employing SCs in both the stator and rotor circuits — known as fully superconducting machines — which may allow a further increase in the machine torque density. Nonetheless, the AC loss in HTS working in alternate fields and supplied with AC currents, which must be dissipated for the safe operation of the conductors, is still one of the main limiting factors for the application of superconductors in energy conversion devices.

Superconductors introduced in AC windings require extensive electromagnetic studies to analyse the working conditions of the materials, which are heavily influenced by the imposed time-varying current and surrounding magnetic fields. The accurate estimation of superconductor performance and AC losses is indispensable for realizing practical designs since excessive heating of the SC coils risks the disruption of the superconducting state, otherwise known as *quench*, and can potentially cause irreversible damage to the superconductors. The chosen cryocooling system must deliver the required cooling power to extract the heat incurred by the windings and maintain the superconductors within cryogenic temperatures. Therefore, methods for precisely estimating AC losses in SCs are essential in achieving feasible designs that optimize both the functionality of the superconductors and the overall machine performance.

Superconductors are characterized by non-linear electrical resistivity, and their performance is highly dependent on the surrounding magnetic field intensity and direction. Thus, the performance of superconducting elements inserted in complex electromagnetic environments, such as rotating electrical machines, often requires finite element method (FEM) tools to be accurately assessed. Many formulations have been presented in the literature to model superconducting materials based on their resistivity laws and magnetic field dependence [43, 44]. However, these models are computationally demanding and time-consuming, mainly due to the high detail that is imperative to accurately compute power losses in superconducting materials. The reduced dimensions of SCs (with a few millimetres width and micrometre thickness), together with their high width over thickness aspect ratio, further exacerbates this non-linear models complexity when SCs are to be applied in (FEM) simulations of rotating electrical machines [45]. This complexity in machine analyses indicates that FEM models that include the non-linear superconducting formulations might not be adequate in machine design methodologies that typically involve optimization processes requiring several thousand simulations.

HTS materials have intrinsic fragility and brittleness, so they must not be bent in specific directions or beyond their minimum bending radius. Furthermore, they are intrinsically anisotropic in their sensitivity to varying external magnetic fields. This means that specific winding configurations are more suitable for their introduction in electrical machines than others. In this work, superconductors are applied in axial flux permanent magnet machines since this topology allows toroidal core wound stator windings, which are appropriate for easily respecting the bending constraints of the materials. Additionally, throughout this work, it will be shown that these windings allow taking advantage of the anisotropic response of SCs to external fields to significantly decrease AC losses in the materials during standard motor operation, making this machine particularly suitable for the application of superconducting stator windings. This machine typology, however, is exceedingly complex and time-consuming to model in FEM models that also include superconducting formulations since 3D geometries and moving meshes are mandatorily required. There is, therefore, a critical need for faster yet accurate methods to facilitate efficient machine design processes.

This thesis intends to investigate novel approaches and develop tools for accurate electromagnetic analyses in electrical machines with superconducting AC windings. The investigation focuses on modelling and efficiently applying superconducting tapes and wires to augment the performance and specific power values of electric machines for energy conversion and propulsion applications. The research objectives are summarized as follows:

1. Experimentally investigate the influence of very low-temperature (77 K) operation in both normal conducting, ferromagnetic and superconducting materials.
2. Effectively use experimental data to characterize and develop FEM models to provide an accurate description of material electromagnetic properties and loss behaviour.

3. Design HTS stator windings in axial flux machines and estimate their performance.
4. Develop suitable design methodologies for HTS machines using FEM analysis.
5. Analyse the impact of time-varying regimes, i.e., imposed AC currents and alternate external fields on superconducting losses, and identify suitable mitigation methods.
6. Accurately estimate HTS winding losses and cooling requirements when implemented in armature windings of rotating electrical machines.

## 1.3 Contributions of the Thesis

This thesis presents a methodology to construct multiphysics FEM models that enable the efficient assessment of the feasibility of superconducting windings in electrical machines through electromagnetic and thermal analyses.

To accurately calibrate the presented FEM models, experiments were performed on ferromagnetic, conducting, and superconducting materials. Conventional laminated ferromagnetic toroidal samples used for the core realization of electrical machines operated at ambient temperature were tested to explore their behaviour at cryogenic temperatures. Different superconducting material samples, such as tapes, wires, and bulks, were tested at cryogenic (77 K) conditions with both DC and AC supply. The data obtained from the materials regarding their electrical and magnetic characteristics, such as the BH curve and specific core loss temperature dependence in ferromagnetic samples and electric field characteristics and AC losses in superconducting samples, was used to describe the material properties in multiphysics models.

The test setups of DC and AC experiments with superconducting tapes to characterize and validate the superconducting models are explained in detail. A new FEM method for implementing the $T-A$ formulation is proposed to consider the impact of the copper layers in the superconducting losses without recurring to a coupled electrical circuit. Experimental results were also used to develop an analytical study that considers the presence of both hysteretic and resistive losses in superconducting first-generation (1G) and second-generation (2G) tapes in the overcritical current regimes. The presented models are validated by comparison with the results of other models, experimental data, and analytical formulations available in the literature.

Due to the high computational complexity of 3D models of practical superconducting devices, a new methodology is presented to perform more expedited analyses on the machine HTS armature using both 3D and 2D models. To develop and test the proposed methodology, 3D electromagnetic simulations of two case-study machines are performed, where the conditions on the armature slots are examined to estimate losses in the superconducting coils. The approach is based on the separation of the models of electrical machines and superconducting windings, which allows them to be studied using different electromagnetic formulations. First, the motor performance is estimated by modelling a conventional electrical machine where the superconductors are represented as flat conducting surfaces with an imposed current, without considering the superconducting non-linear behaviour. Through the motor/generator study, the machine performance and design are demonstrated (for the selected mmf), and information on the magnetic flux density in the armature slots is provided. Considering that the non-linear characteristics of superconductors are neglected at this stage, it is feasible to include the non-linear description of the ferromagnetic materials that can provide a more realistic representation of the magnetic flux density in the FEM model.

With the magnetic field information obtained in the rotating electrical machine simulation, a separate model is constructed to represent only the interior of a single slot of the armature winding of the machine and the superconducting elements (either in 2D or 3D configurations) where the superconducting formulations can be imposed. The proposed methodology can significantly reduce the computational complexity of the simulation and time and memory requirements. This means that the 2D single slot model can be efficiently used to estimate superconducting winding performance and to investigate practical methods to mitigate the effects of the applied magnetic field on the SC tapes, such as shields, flux diverters, and different tape positioning on the armature slot. The methodology is expanded to consider the cooling fluid and flow rate requirement of each superconducting coil with a preliminary stage slot thermal model. The proposed methodology provides a complete procedure for performing efficient analyses on superconducting loss estimation and respective cooling requirements for the design of superconducting AC electrical machines.

## 1.4 Outline of the Thesis

The first Chapter of this thesis presents the introduction, motivation, and contributions to the theme of superconducting electrical machines. In Chapter 2, the subject of superconductivity and relevant phenomena are explained in more detail, and a short literature review is provided on working prototypes of electrical machines and their respective challenges. Since it is also in the scope of cryogenic and superconducting energy conversion devices, the effects of cryogenic temperatures in conventional conducting, soft, and hard ferromagnetic materials are briefly described.

Chapter 3 describes the models used to simulate superconducting materials, characterized by their non-linear resistivity $E$-$J$ law and magnetic field dependence. The $T-A$ formulation is introduced, and the HTS tape numerical models and calibration procedure with experimental measurements at 77 K are described. A model based on the $T-A$ formulation is proposed to consider the influence of the copper layers, which can become significant in overcritical (high current) and high-frequency regimes to determine the coated superconductor losses. A new analytical formulation considering the hysteretic and resistive losses of superconducting 1G and 2G tapes is presented, and FEM models are validated by comparison with experiments and analytical results reported in the literature.

In Chapter 4, a case study axial flux permanent magnet machine (AFPM) is designed to investigate the applicability of superconductors when inserted in electrical machines armature windings carrying AC currents and subject to AC fields. A 2D slot model for expedited analyses of the superconductors, taking into account the first time-harmonic of the magnetic field generated by the rotor of the AFPM machine, is described in detail, and results are presented.

Chapter 5 expands the developed slot model to describe the full harmonic content of the magnetic field surrounding the superconductors in the armature slots of electrical machine windings. The model takes into account the full spatial and temporal distribution of the magnetic field inside the electrical machine stator coils to determine the superconductor AC losses and estimate their performance more accurately and for any machine typology, given its FEM model. To test the applicability of the extended model, a toroidal double-rotor non-optimized AFPM is designed to apply superconductors in the armature windings. The slot model is verified with analytical solutions for transport and magnetization losses in superconductors, with good agreement between analytical and simulation results.

In Chapter 6, a preliminary thermal model is then developed and applied to estimate the cooling requirements of the case-study AFPM. A setup to measure the temperature of a superconducting coil is developed and used to experimentally verify the thermal model.

Chapter 7 presents the conclusions for the thesis and outlines possible future work based on the proposed methodologies.

## 1.5 List of Publications

### Journal Papers

[43] I. S. P. Peixoto, F. F. da Silva, J. F. P. Fernandes, S. Vaschetto and P. J. C. Branco, "A Distributed Equivalent-Permeability Model for the 3-D Design Optimization of Bulk Superconducting Electromechanical Systems," in IEEE Trans. Appl. Supercond., vol. 33, no. 6, pp. 1-10, Sept. 2023, Art no. 3601610

[13] J. F. P. Fernandes, L. F. D. Bucho, F Ferreira da Silva, I. S P Peixoto, S. Vaschetto and P J Costa Branco, “Alternative analytical models for HTS tapes considering their AC hysteretic and resistive losses,” Supercond. Sci. Technol. vol. 37 pp. 035004

[46] I. S. P. Peixoto, S. Viarengo, J. F. P. Fernandes, F. Freschi, L. Savoldi and S. Vaschetto, "Electromagnetic modelling of the copper layers influence for AC losses in ReBCO coated conductors based on T-A formulation," in IEEE Trans. Appl. Supercond., 2024

[47] I. S. P. Peixoto, Y. Sogabe, J. F. P. Fernandes, S. Vaschetto and N. Amemiya, "Mitigation of Superconducting AC Losses in Axial Flux Synchronous Machines With Multifilament Coated Superconductors," in IEEE Transactions on Applied Superconductivity, vol. 35, no. 5, pp. 1-5, Aug. 2025, Art no. 5901505,

### Conference Papers

[48] M. Biasion, I. S. P. Peixoto, J. F. P. Fernandes, S. Vaschetto, G. Bramerdorfer and A. Cavagnino, "Iron Loss Characterization in Laminated Cores at Room and Liquid Nitrogen Temperature," 2022 IEEE Energy Conversion Congress and Exposition (ECCE), Detroit, MI, USA, 2022, pp. 1-8.

[49] I. S. P. Peixoto, S. Vaschetto, J. F. P. Fernandes, P. J. Da Costa Branco, A. Tenconi and A. Cavagnino, ”Modeling Approach for Superconducting AC Windings: Case Study on Axial Flux PM Machines,” 2023 IEEE Energy Conversion Congress and Exposition (ECCE), Nashville, TN, USA, 2023, pp. 3790-3795.

[50] A. Uosef et al., "Superconducting AC Machines and Cryogenic Power Electronics for Reliable and Power-Dense Energy Conversion," 2024 International Conference on Electrical Machines (ICEM), Torino, Italy, 2024, pp. 1-8.

[51] I. S. P. Peixoto, L. Perilli, F. Graffeo, J. F. P. Fernandes, P. J. da Costa Branco and S. Vaschetto, "A Slot Model for Loss Estimation in Superconducting AC Electrical Machine Windings," 2024 International Conference on Electrical Machines (ICEM), Torino, Italy, 2024, pp. 1-7.

# Chapter 2

# Superconductors and Their Application to Electrical Machines

## 2.1 Introduction

This chapter introduces properties of superconductors and the challenges associated with their application in electrical machine windings. The characteristics and phenomena of superconducting materials and practical applications are described. The discussion primarily focuses on type II superconductors, with specific emphasis on HTS conductors such as cables, wires, and coated conductors (CC) which are investigated throughout this work. Given the critical importance of AC losses in superconducting applications, this topic is introduced, and its relevance to energy conversion devices is highlighted. The effects of cryogenic temperatures on conventional materials often used in electrical machines, including conducting, hard, and soft ferromagnetic materials, are stated. Finally, the application of superconductors in electrical machine windings and their challenges are discussed to propose the motivation for the research presented in this thesis.

## 2.2 Superconductivity

### 2.2.1 Superconductors and Their Main Characteristics

Superconductivity was first discovered by the Dutch physicist H. Kamerlingh Onnes following his successful experiments in liquefying helium. In 1911, while investigating the properties of metals at very low temperatures, Onnes observed a sudden drop to immeasurable values in the resistivity of mercury at the boiling temperature of helium (4.2 K) [52]. The temperature at which this transition occurred was termed the critical temperature of the material, $T_c$. Subsequently, Onnes verified that this near resistance-free current conduction could only be sustained up to a specific current density threshold value, dependent on the material, which increased with decreasing temperature. Hence, the second parameter of the superconducting state is defined as the critical current density, $J_c$ [53, 54].

In addition to exhibiting almost vanishing DC resistance at very low temperatures, superconductors were found to spontaneously expel externally applied magnetic fields when maintained below their critical temperature. This field expulsion, caused by the appearance of screening currents flowing at the surface of the material, which generate an opposing magnetic field, was discovered in 1933 by W. Meissner and R. Ochsenfeld and became known as the Meissner effect [55]. This discovery also indicated that superconductivity could not be sustained when external magnetic fields were above a certain amplitude $H_c$, thereby defining the third critical parameter of the superconducting state.

These parameters were later found to be interdependent, delineating a critical surface enclosing the superconducting state. H. London and F. London first attempted to describe the complete expulsion of the magnetic field in 1935 [56]. However, a comprehensive explanation of the superconductivity phenomenon was only published in 1957 by J. Bardeen, L. Cooper, and J. R. Schrieffer, known as the BCS theory [57]. According to this theory, at very low temperatures, electrons can be found in the BCS ground state, where they form pairs of opposite spin and momenta, known as *cooper pairs*. This implies that rather than normal electrons, *cooper pairs* carry the supercurrents within the material. The sample will retain its superconducting state if the energy entering the system does not exceed the gap between the BCS ground state and the single electron (normal conductive) state. This means that the critical parameters defining the superconducting state limits, such as the critical temperature $T_c$, critical magnetic field $H_c$, and critical current density $J_c$, are, in fact, different measures of the maximum energy that can be supplied to the material before it reverts to its resistive state. While BCS theory successfully explains superconductivity in some elements at sufficiently low temperatures, it does not fully account for the superconductivity observed in high-temperature or type II superconductors.

### Type I and Type II Superconductors

According to their response to external magnetic fields, Superconductors are categorized into type I or type II. Type I superconductors completely expel external magnetic fields up to a critical field $H_c$, after which superconductivity vanishes. They are typically natural elements such as aluminium and lead, whereas type II superconductors are usually alloys. Type-II superconductors also expel all fields below a critical lower field $H_{c1}$ exhibiting the Meissner state. However, their characteristics allow them to sustain a mixed state where magnetic flux tubes (or fluxoids) penetrate the material at fields $H_{c1}<H<H_{c2}$ [58]. These resistive fluxoid regions appear as small tubes carrying a quantized magnetic flux $\phi_0$ given by $h/2e$ or $2.07\times10^{-15}$ Wb [59, 60], where $h$ is the Planck constant $6.55\times10^{-34}$ J·s and $e$ is the fundamental electron charge, $1.602\times10^{19}$ C. The flux penetrated regions become resistive while the sample remains superconducting, hence the denomination of mixed state. When $H_{c2}$ is surpassed, the magnetic field fully penetrates the superconductor, and the material reverts to its normal resistive state [61]. In Fig. 2.1, an illustration

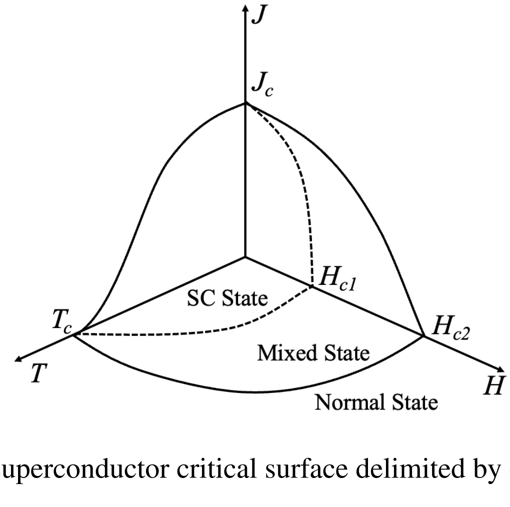

Fig. 2.1 Type II superconductor critical surface delimited by critical parameters

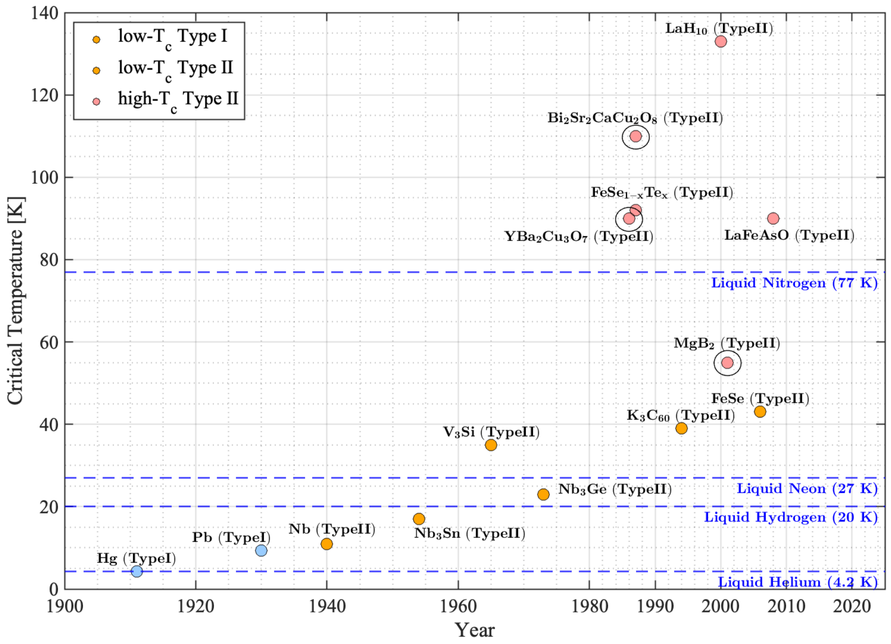

Fig. 2.2 Superconducting critical temperatures with respective year of discovery, from 1911 until 2015, and cooling materials, circled are the most commonly used HTS in electrical machines

of the type II superconductor critical surface demonstrates the possible states of the material.

Compounds like YBCO and BSCCO-2223 are examples of these materials and present a mixed state between 10-20 mT and 100 T [62]. Throughout the years, research led to the discovery of several superconducting materials; some can be found in Fig. 2.2 where appropriate cooling fluids are stated. Given the dependency of the critical current density and critical magnetic field on the temperature, superconductors are typically handled at temperatures significantly lower than their critical limits to ensure sufficient cooling and increased current-carrying capacity [63].

### 2.2.2 Dissipative Processes in Type II Superconductors

The fluxoids appear in Type II superconductors supplied with currents and/or exposed to magnetic fields. A fluxoid is a region with a magnetic field penetration and, therefore, in this region, a Lorentz force will manifest $F_L$, (2.1) when there is a

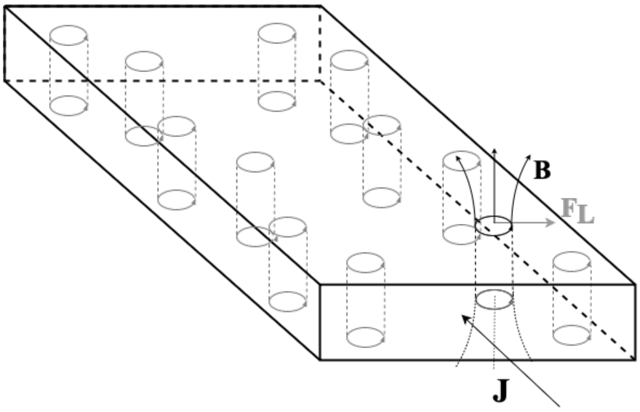

Fig. 2.3 Flux pinning in superconductors fluxoids in type II superconductors, and statement of fluxoid movement direction under current influence

current in the superconductor, as depicted in Fig. 2.3. The motion of the fluxoids is typically opposed by irregularities in the SC material, such as defects or precipitates that act as pinning centres and provide a pinning force for the fluxoids $F_P$ [64].

$$\mathbf{F}_L = \mathbf{J} \times \mathbf{B} \tag{2.1}$$

The HTS materials to which impurities (such as residues) are added are called hard superconductors. These materials are especially suitable for practical applications, such as magnets, motors, and generators, where they must maintain their superconducting properties under high magnetic fields and current densities. When the Lorentz force is such that $F_L < F_P$, the superconductor is said to be in flux pinning regime. However, if the supply current or the external field becomes large enough so that $F_L > F_P$, the fluxoids will move along the width of the slab, generating dissipation. In this situation, the superconductor will enter a flux-flow state, where it exhibits resistivity.

### Hysteresis Losses

Precipitates or pinning centres that oppose the fluxoid movement prevent energy dissipation (and heating) and allow the material to withstand large transportation currents in high magnetic fields. However, the existence of these pinning centres in the material that "trap" the fluxoids also makes the magnetization process in superconductors irreversible. Consequently, although hard superconductors are

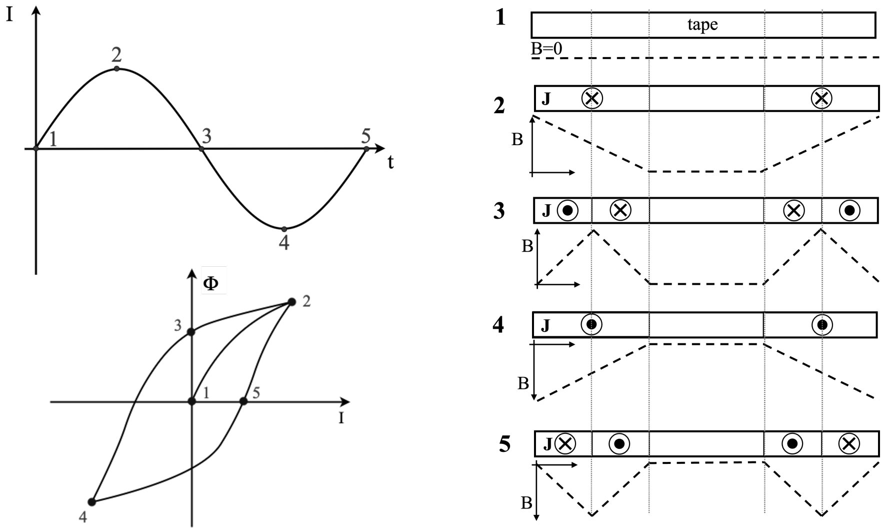

Fig. 2.4 Magnetization of a superconducting slab with an alternate current excitation, on the left, the imposed current waveform and hysteresis cycle are shown. The current and field variation is shown for specified cycle points on the right side.

suitable for practical applications, they also feature non-negligible superconducting loss under time-varying regimes [65]. The magnetization process of a SC slab is illustrated in Fig. 2.4.

AC losses in HTS can be separated into several components depending on their origin: hysteresis, coupling, and eddy current losses.

Superconductors manifest hysteresis losses when supplied with transport currents or when currents are induced from external magnetization. Initially, a fluxoid pattern appears as an externally applied magnetic field penetrates the superconductor. The fluxoid pattern rearranges over time if the magnetic field is time-variant according to the change in field penetration [66]. Similarly, when a superconductor is supplied with a transport current, a magnetic field is generated, known as *self-field.* When the current is time-variant, the self-field it generates and eventually penetrates the superconductor will also vary in time. In both situations, the movement of flux lines that causes a variation of the internal magnetic field of the material drives an electric field **E** according to Faraday's law in (2.2).

$$\nabla \times \mathbf{E} = -\frac{\partial \mathbf{B}}{\partial t} \tag{2.2}$$

The dissipation power density in the material can be determined by the dot product between the current and electric field $\mathbf{E} \cdot \mathbf{J}$. This is both the principle of magnetization loss and transport loss in superconductors. The main difference between these two cases is whether the energy source is an external magnetic field or a current source. Since the energy dissipation in the hysteresis regime increases with increasing tape width, thinner or multifilament conductors are often used to reduce SC losses in electrical devices [67].

#### Eddy Current and Coupling Losses

Superconducting wires and tapes for practical applications consist of both HTS and standard conducting materials for stable operation and enhanced cooling. When exposed to an external magnetic field, these conductors naturally induce eddy currents, causing ohmic dissipation. The presence of eddy currents in the materials and the superconductor can be critical when the wires and tapes consist of multiple superconducting strands or filaments surrounded by a resistive matrix. In this situation, when the induced currents flow from one superconducting filament to another, they will also flow through the surrounding resistive path that separates the filaments, generating coupling losses [68].

Since all these processes dissipate energy and cause an increase in temperature, the operation conditions of the superconductors are usually analyzed carefully before they are introduced into electrical devices.

## 2.3 HTS for Electrical Machine Applications

### 2.3.1 HTS Materials

As introduced in Chapter 1, among superconducting materials, HTS are the most suitable to be applied in energy conversion devices due to their higher operating temperatures and high current carrying capability. HTS can be introduced in electrical machines in several forms. In windings, superconducting wires/tapes are introduced as coils. These coils are mainly fabricated from three materials: 1G and 2G tapes/wires and $MgB_2$. Some of the most commonly used HTS materials for electrical applications are shown in Fig. 2.5.

Multifilament composites are defined as first-generation (1G) HTS wires. An alloy matrix, such as nickel or silver, usually surrounds the superconducting filaments in these wires/tapes. Examples of these conductors are $MgB_2$ and BSCCO, shown in Figs. 2.5a and 2.5c [1, 2]. As outlined in section 2.2.1, (see Fig. 2.2), $MgB_2$ has a very low critical temperature among HTS. Although it requires lower cooling temperatures ($T_c = 39$ K), and its typical bending radius is high (>10 cm) [69], its main advantage derives from the low cost of both Mg and B raw materials and low AC losses [70]. These characteristics make it suitable for electrical machine windings, where the materials are subject to alternate currents and fields [70]. $MgB_2$ superconductors can be realized as multifilament wire as shown in Fig. 2.5a [1] or as tapes and bulks. $Bi_2Sr_2Ca_2Cu_3O_x$ can be fabricated into BSCCO-2223 and BSCCO-2212, where the former ($T_c = 110$ K) is usually manufactured into tapes and the latter into round wires ($T_c$ up to 95 K) [71]. Their main advantages are mechanical and thermal robustness and higher operating temperature [62].

2G HTS tapes are made of rare-earth barium copper oxides (REBCO) where the rare-earth element is usually Yttrium (Y) or Gadolinium (Gd) [72]. The tapes comprise several layers as depicted in Fig. 2.5b. They are fabricated by thin film deposition on a metallic substrate; the tape has an overall thickness of typically 0.1 mm and can carry critical currents up to 160 A/4 mm tape at 77 K [36, 73]. While the substrate provides mechanical strength, the silver and copper layers provide an alternative low-resistivity current path if a quench occurs in the SC layer. The stabilyzing normal conducting layers also contribute to enhance heat dissipation in the tape due to the material high thermal conductivity. The current density variation of the tape with the surrounding magnetic field is strongly anisotropic due to its high aspect ratio between thickness and width. It is mainly sensitive to magnetic fields applied in the transverse direction to its flat face.

Besides wires and cables, SCs such as YBCO and $GdBa_2Cu_3O_7$, Gadolinium Barium Copper Oxide (GdBCO) (shown in Fig. 2.5e and 2.5f) are also used as bulks to store high magnetic flux density values in superconducting magnets, substituting permanent magnets as shields in levitation systems and magnetic bearings [42].

Recently, cables consisting of REBCO tapes wounded at short twist pitches have gained interest for electrical applications because of their improved mechanical flexibility [74, 75] (shown in Fig. 2.5d [3]). They mainly find application in high-field magnets and power cable systems. Examples are the Conductor on Round

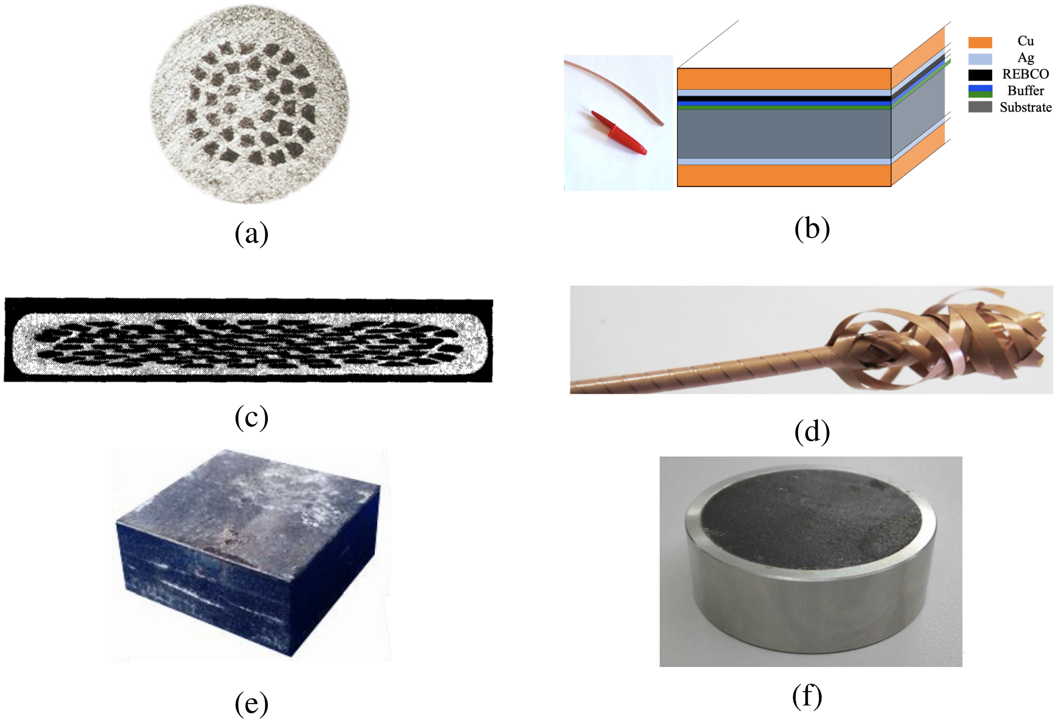

(a) (b) (c) (d) (e) (f)

Fig. 2.5 HTS materials for electrical applications. (a) MgB2 wire filaments, in black, are surrounded by a Monel outer sheath and a and Nickel matrix, resistive alloys [1], (b) REBCO coated conductor on the left with illustration of tape several layers (right), (c) 85 filament BSCCO-2223 tape-shaped wire the filaments are embedded in a silver alloy matrix, acting as a stabilizer [2], (d) CORC® cable [3], (e) YBCO bulk superconductor [4], (f) GdBCO bulk superconductor [4]. The electric current path lies perpendicular to the plane of the page in both (a), (b) and (c).

Core (CORC®) cable and the Spiral Copper-plated Striated Coated-conductor cable (SCSC) [76]. While the possibility of using the former in the windings of electrical machines is still under study [3], the latter was specially designed for operation under AC currents and fields. The tapes in the SCSC cable are striated to decrease the AC losses, and filaments are decoupled by spirally winding the tapes around a core. When made of conductive material, this core can work as a current path in case of quenching. Their proven low loss under AC conditions and robustness against local defects and normal state transition make them promising for application in electrical machines armature windings [77]. The main characteristics of HTSs commonly used for electrical machines are listed in Table 2.1.

Table 2.1 Main characteristics of HTS used for electrical machines

| Name | | Type | $T_c$ | $I_c$ / Trapped field | Advantages (A) / Constraints (C) | Ref |
|---|---|---|---|---|---|---|
| $MgB_2$ | | 1G wire | 39 K | 150 – 2600 A (20 K) | (A) Low cost of Mg and B raw materials;<br>(A) Suited for standard wire manufacturing;<br>(A) Low AC loss at high frequency;<br>(C) Low critical temperature | [16], [30], [70], [3] |
| Copper Oxides | $(Bi,Pb)_2Sr_2Ca_2Cu_3O_{10}$ | 1G or 2G wire | 110 K | 120 – 155 A (77 K) | (A) $LN_2$ cooling;<br>(A) Large transportation currents at high magnetic field levels | [28], [36], [73] |
| | REBCO | 2G wire | 119 K | 80-600 A (77 K) | (C) Bending radius and fragility, limits their use in arbitrarily shaped windings | |
| | $YBa_2Cu_3O_7$ | 2G wire | 92 K | 90 A (77 K) | (C) Non-negligible AC loss | |
| | CORC® and SCSC cables | REBCO cable | 50 - 77 K | 840 – 4200 A (76 K) | (A) Improved flexibility and high $J_c$;<br>(A) Higher tolerance to strain and degradation.<br>(C) High price, since it requires large amounts of REBCO tape | [78], [79] |
| | $YBa_2Cu_3O_7$ and $GdBa_2Cu_3O_7$ | Bulk | 93 K | 16 T (YBCO at 24 K), 17.6 T (GDBCO at 32 K) | (A) Can be used as field sources, storing high values of magnetic flux density.<br>(C) Machine must be adapted to bulk placement | [80], [81] |

### 2.3.2 SC Coil manufacturing

HTS coils for practical applications are designed to match the operating conditions required by the superconductors for their specific use. The superconducting coil usually needs to fit the geometric constraints of the considered superconducting magnet and the bending limitations of the superconducting tapes/wires. Nonetheless, specific geometries are commonly used in superconducting coils to allow for the respect of the strain/bending limitations of the material and critical magnetic field.

Regarding the electrical connection in a multiturn coil, the turns can be insulated and non-insulated. Insulated coils are usually wound with a thin layer of insulation between each turn where commonly Kapton tape (thickness 0.05 mm) is used [82, 83]. Non-insulated windings are wounded with turn-to-turn contact between HTS tapes. Each option can offer different advantages depending on the application and coil working conditions. Non-insulated (NI) coils are used for increased stability against quench since their turn-to-turn contact allows the current in each layer to be shared with adjacent layers [83]. This means that when there is a local defect in the coil (a region with lower critical current and/or increased resistivity), the current will flow into a lower resistivity path, preventing quench and localized heating. This also gives the coil increased mechanical and thermal robustness [84]. However, the presence of radial currents in the coil, either during regular operation or quench, introduces unbalanced forces that can cause strain on the conductor [85]. Additionally, NI coils working in AC environments can have coupling between layers, contributing to the increase in coil losses. Hence, choosing between insulated and non-insulated windings requires careful consideration [5]. Two HTS coils with different insulation are shown in Fig 2.6.

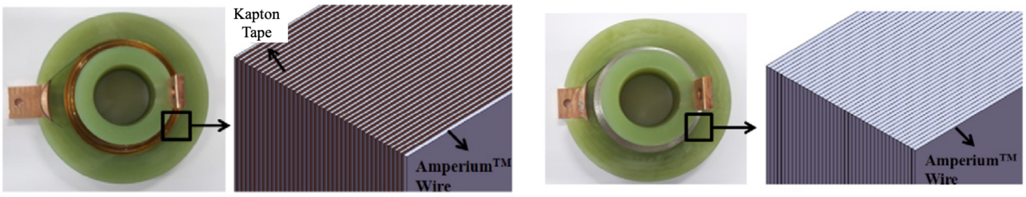

(a) (b)

Fig. 2.6 HTS coils and their insulation technique, (a) turn-to-turn insulated coil and (b) No-insulation coil [5].

The most common structures used for superconducting coils in electrical machines are pancake, double pancake (shown in Fig. 2.7 Electromagnetic models Ex[6]) and racetrack coils, where the superconductors are bent over their widest face [37, 6]. Other geometries are also reported since different shapes are admissible [86]. However, these more common winding typologies are preferred since they usually allow respect for the bending restrictions of the superconductors and fit the design requirements of electrical machines. To wind the coils HTS coated conductors should be bent with low tensile strength and with their substrate facing the outward side of the coil to keep higher critical currents since the current has higher degradation with tensile strain than compressive strain [87]. The material properties must be considered since strain sensitivity and flexibility of SC coils are highly dependent on the superconducting material and tape/wire/cable fabrication method [88]. After winding, the coils are typically fixed with epoxy or paraffin resin, and current leads are attached [89, 90]. To ensure better cooling, attached to the coils, materials such as copper can be added and will act as a heatsink during operations due to their high thermal conductivity [31, 91].

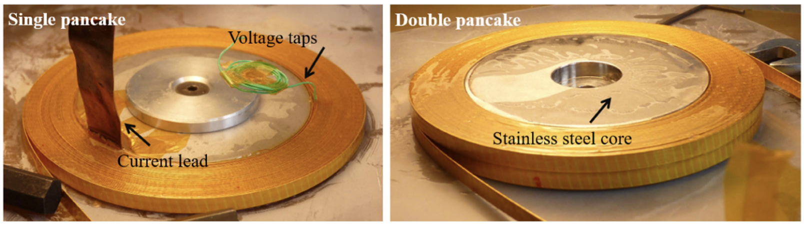

Fig. 2.7 HTS coils, on the left a single pancake coil and on the right a double pancake coil [6].

### 2.3.3 Conducting and Ferromagnetic Materials in Cryogenic Conditions

Considering that SC machines operate in cryogenic conditions, it is likely that other machine components also operate at very low temperatures, depending on the cooling system that was designed for the machine. This means that if cooling systems enclosing parts of the machine other than the SC windings are employed, conducting soft and hard ferromagnetic materials can also be operated at very low temperatures. In this case, when estimating the machine performance, it is essential to consider that this very low-temperature operation affects the material characteristics and losses of the other components in the machine.

### Temperature Dependence of Electric Resistivity in Conductors

The electric resistivity of conducting materials describes the frictional force electrons find while travelling across a medium. It is a measure of opposition to the current flow in conducting materials. This force appears in collisions, which provoke momentum loss in the moving electrons. At ambient temperature, ohmic resistance results from collisions between the electrons and the crystal lattice imperfections, i.e., impurities, lattice defects, and deviated ions due to thermal oscillations. The thermal oscillations are the main reason for the appearance of temperature-dependent resistivity. Logically, when the temperature is decreased, the thermal oscillations become scarcer until only a residual resistivity (from impurities and lattice defects) is left [59]. The material resistivity can then be seen as a sum of the contribution of impurities $\rho_0$ and the intrinsic resistivity caused by vibrations in the lattice $\rho_i(T)$ [92].

$$\rho = \rho_0 + \rho_i(T) \tag{2.3}$$

Even though many materials have been found to exhibit superconductivity when exposed to very low temperatures, some of the best conductors known today, such as copper, silver, or gold, do not exhibit superconductivity unless exposed to very high pressures. Instead, they present a decreasing resistivity with temperature until their residual resistivity $\rho_0$ as described in (2.3). Depending on the purity of the metal, the resistivity dependence on the temperature $\rho(T)$ can also be defined. This characteristic can be determined by the residual resistivity ratio (*RRR*), which is characterised by the ratio between ambient temperature and cryogenic resistivity, $RRR = \rho(273\,\mathrm{K})/\rho(4.2\,\mathrm{K})$. A large RRR means the material has high purity. For example, standard copper conductors have $RRR \approx 100$ [93], while 2G superconducting tapes copper stabilizing layers have a $5 < RRR < 65$ [94]. Since the *RRR* is the ratio between the resistivity of the conductor at ambient and cryogenic temperatures, the losses in the conductor will be reduced for higher *RRR* values (higher material purity) in cryogenic conditions. Most *RRR* values of commonly used materials can be found in NIST public databases [92, 95].

### Soft and Hard Ferromagnetic Materials Operating at Very Low Temperatures

Soft ferromagnetic materials such as iron cores have increased losses when operated at very low temperatures. Under cryogenic conditions, there is an increase in the conductivity of the material, which directly translates into higher eddy current losses when exposed to AC currents or alternate fields. The effect is noticeable even when the iron cores are laminated. The loss increment typically depends on the steel grade, magnetizing frequency, and operating flux density [48]. The magnetization curve of iron samples increases marginally, with a higher BH curve for cryogenic temperatures. This iron characteristic change directly results in iron losses in electric machines increasing considerably at cryogenic temperatures (around 15%) [96]. Hence, a warm core configuration is preferable, with the cooling only for the machine windings.

In hard ferromagnetic materials, different changes will occur depending on the considered material. Generally, the magnetization remanent field increases with the decrease in temperature; the BH curve will shift with more noticeable effects at very low temperatures (close to 10 K). While hard ferrite magnets will have decreased coercivity $H_{ci}$, saturating faster and leading to a flux loss, SmCo and NdFeB magnets will have increased flux output and coercivity under low-temperature conditions [20]. Nonetheless, these effects are usually gradual and continuous and, thus, for all purposes, clearly distinguishable from the transition of the superconducting state.

## 2.4 Superconducting Machine Prototypes

Electrical machines equipped with superconducting materials can be divided into two categories: i) partially or ii) fully superconducting machines. When superconductors are applied to either the stator or the rotor circuits of the machine, they are named hybrid or partially superconducting. Partially superconducting electrical machines are manufactured using SCs, conventional conductors, or permanent magnets. A cryostat is commonly used to maintain the temperature of the superconducting parts well below $T_c$. Fully superconducting machines employ SCs for all their electric circuits. Considering the high current densities and fields enabled by introducing superconductors and the negligible DC resistance, these machines can be more compact and efficient, resulting in higher torque densities. However, there are still barriers to using AC supply due to AC loss in SCs. Some of the prototypes for fully and partially superconducting machines available in the literature for synchronous machines and their challenges and advantages are outlined.

### 2.4.1 Partial Superconducting Synchronous Machines: Superconducting Field Excitation

Partially superconducting machines can employ superconductors in either the rotor or stator circuits. Superconductors typically carry DC currents and exhibit extremely low resistivity when used on the rotor side. When integrated into the stator windings, high-temperature superconducting coils are exposed to alternating magnetic fields and currents, which can result in non-negligible losses. Most superconducting electrical machine prototypes are synchronous machines with a partial configuration, where superconducting circuits are confined to the rotor and used for DC excitation [37, 42]. Figure 2.8 [7] illustrates an example of a partially superconducting axial flux machine featuring a superconducting field winding and a copper armature designed for aircraft applications. By using superconductors in DC conditions, rotor resistive losses can become minimal, enabling them to carry extremely high current densities. As a result, the air gap flux density can be substantially increased, often reaching values up to twice those of conventional machines

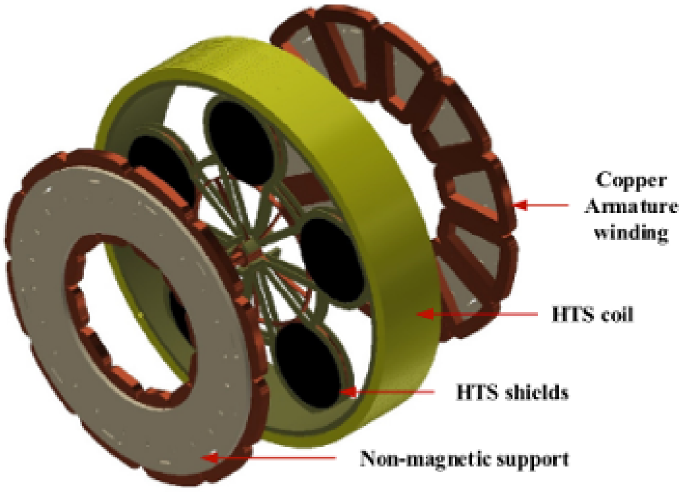

Fig. 2.8 Partially superconducting axial flux synchronous machine for aircraft applications [7].

with copper windings. However, such high magnetic flux densities can cause saturation in iron components. To mitigate associated ferromagnetic losses, designers often reduce core volume or adopt air-core configurations [28]. The design and manufacturing of these partially superconducting machines is usually challenging, particularly due to the need for rotating cryocoolers. Nonetheless, the increased magnetic loading is vital for enhancing torque density. The field windings can be implemented using first- and second-generation (1G and 2G) HTS tapes. This topology has been successfully demonstrated in wind power generation [97, 98] and electric transportation applications [8, 99].

The standard structure of a synchronous HTS wound field propulsion motor is shown in Fig. 2.9 [8]. The rotor has six poles made of DI-BSCCO and is cooled by gaseous helium, operating at 30 K. The rotor core and the stator teeth are made of non-magnetic material to prevent iron saturation [100]. The stator is air-cooled and features conventional copper windings. The motor was tested and showed high-reliability operation for ship propulsion applications, with a maximum output power of 3.02 MW at 160 rpm, reaching 180 kNm torque. Considering the cooling system, the overall efficiency was kept above 95 %, where more than half of the loss contribution came from the armature air-cooled copper windings.

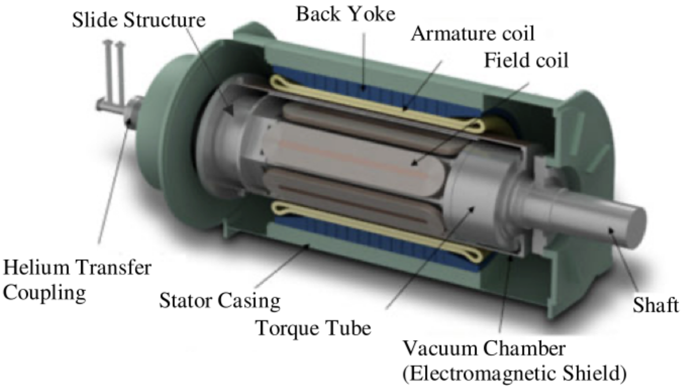

Fig. 2.9 Wound field synchronous machine with a superconducting field winding for ship propulsion applications [8].

Siemens developed two partially superconducting synchronous machines for marine applications: a 400 kW motor and a 4 MVA generator [101]. The rotor windings in both machines were constructed using Bi-2223 tapes, while the stators featured copper Litz wire supported by a fiber-reinforced plastic structure. The

400 kW machine achieved an efficiency of 96.8 %, accounting for cryocooler power consumption. The 4 MVA generator reached an efficiency of 98.7 % at the unit power factor. These efficiencies are approximately 1–2 % higher than those of comparable machines using conventional technologies. Regarding physical characteristics, the 4 MVA generator exhibited an 82 % reduction in volume and was 63 % lighter than traditional synchronous generators [102].

Two partially superconducting motors cooled via forced helium flow were validated in [103, 104]. The first prototype—a 15 kW machine—was developed as a trial for a future megawatt-class fully superconducting marine motor. It incorporated a superconducting stationary field winding and a copper rotating armature, achieving a maximum torque of 398 Nm [103]. The YBCO field winding operated within a temperature range of 20–30 K. A second prototype, a 7.5 kW, 360 rpm motor, featured a conventional copper stator and an air-core rotor with REBCO field windings, operating at 40K [104]. The motor demonstrated stable operation up to 11 kW. The authors noted that rotor motion contributed to maintaining uniform cooling, confirming the feasibility of this technology for higher-power machines.

A design for a partially superconducting generator was proposed as part of the Suprapower EU project [16, 31]. This 10 MW, 8.1 rpm direct-drive generator was developed for offshore wind turbine applications. It featured $MgB_2$ field coils and copper armature windings. The design achieved a 26 % weight reduction compared to conventional permanent magnet synchronous generators. The cooling system utilized a modular cryostat per pole, designed to cool only the superconducting windings, thereby reducing the overall cryostat volume.

Superconducting field excitation can also be realized by including bulk superconductors or stacked HTS tapes in the rotor, replacing permanent magnets. This topology is commonly seen in literature in prototypes of radial [105, 9, 106, 107] and axial flux machines [108, 109]. These machines retain conventional design principles while leveraging the high magnetic flux trapping capability of superconducting materials, which can exceed the flux density achievable with permanent magnets [106]. Prior to operation, the superconducting bulks or stacks must be magnetized. Common magnetization techniques include zero-field cooling, field cooling, and pulse field magnetization [110–112, 4].

Trapped field magnets composed of stacked HTS tapes are increasingly favoured over bulk superconductors due to their greater mechanical robustness, lower cost, and

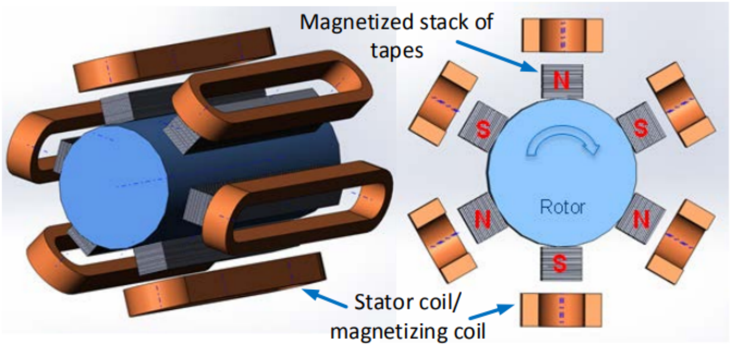

Fig. 2.10 HTS motor with conventional stator windings and HTS stacks embedded in the rotor [9].

compatibility with pulse field magnetization techniques—currently the most widely used method for magnetizing superconducting trapped field magnets [105, 9]. When using SC bulks or tape stacks as substitutes for permanent magnets, their fixed shapes and dimensions necessitate adjustments in machine geometry to accommodate their integration.

### 2.4.2 Partial Superconducting Synchronous Machines: Superconducting Armature Excitation

When superconductors are applied to the electrical machine armature, the cooling can be simplified to a static system; however, superconductors will manifest non-negligible AC loss when supplied with AC currents or subject to AC fields. This means that the cryocooler must deliver the required cooling power to extract the heat incurred by the windings and maintain the superconductors within cryogenic temperatures. Nonetheless, extensive efforts have been carried out towards the development of superconducting machines with AC superconducting windings since they have the potential to surpass conventional machines' limits in achieving compact, lightweight devices of high torque and efficiency [113, 41]. Another impacting factor in constructing superconducting armature windings is the brittleness of the material. Since the SC coils must be wound to respect the material bending limits, specific winding configurations, such as distributed windings, are particularly challenging. However, as will be shown later in this thesis, a distributed winding layout might not be the most suitable choice for superconducting windings, not only due to the material strain limitations but also due to HTS performance susceptibility to the direction of externally applied alternating magnetic fields.

A partially superconducting machine employing superconductors in the stator was presented by the radial prototype in Fig. 2.11 [10]. Even though superconductors manifest non-negligible AC loss, this effect is less noticeable under low-frequency operation. Thus, the intended application is a wind generator. The 2.5 kW low-speed synchronous machine proved the feasibility of the HTS armature winding in a low frequency (10 Hz), low-power application. The experimental tests showed an efficiency of up to 85.5% at 290 rpm. The machine has Bi-2223 stator windings (82 K) and a permanent magnet rotor. Since the purpose of the study was to prove the feasibility of the HTS generator, the design is non-optimized, and its performance is comparable to that of a conventional motor of the same size, however, the authors highlight that the output power can be easily increased if tapes of higher critical currents are used in the armature windings. During motor operation, the stator temperature increased due to the high iron losses; this temperature increase, combined with the effect of the field of the permanent magnets, reduced the temperature-dependent critical current of the superconducting tapes, affecting the tape performance.

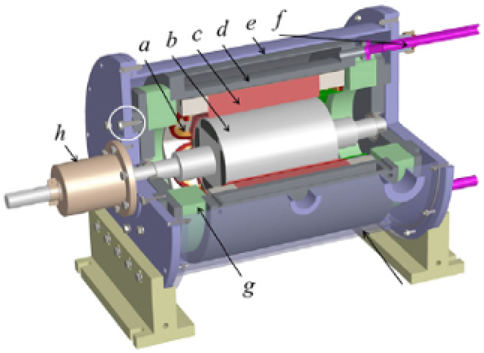

Fig. 2.11 HTS partially superconducting PM radial flux machine. (a) HTS armature coils, (b) permanent magnet rotor, (c) stator iron, (d) stainless steel Dewar, (e) vacuum chamber, (f) liquid nitrogen pipe, (g) fibreglass torque flange, and (h) magnetic fluid sealing device [10].

Axial flux permanent magnet machines with superconductors in the armature windings were tested by different groups, showing the practicability of superconductor stator windings in this topology [114, 11, 115]. BSCCO pancake coils were chosen in [114, 115] while REBCO coils were selected for the prototype in [11]. For the HTS axial flux prototype developed in [115], the authors investigated the influence of self-field from the neighbouring coils and permanent magnets on the

HTS coils' current carrying capacity. A comparison of critical current measurements in the HTS coils at the self-field and inserted in the machine armature showed that the latter has a reduced current carrying capacity. The prototype presented in [114] with iron cores in the stator and rotor was developed for ship propulsion applications. The authors provided several design ideas to reduce the losses in the SCs and the core. This included (i) arranging the magnetic parts in the centre of the armature windings to weaken the alternating field experienced by the HTS and (ii) operating the core at ambient temperature to reduce both the iron and cooling losses. The prototype shown in 2.12 [11] was built fully ironless, with superconducting coils supported by a fibreglass core. The motor achieved an efficiency of 82% at low-frequency operation and a maximum torque of 18.5 Nm.

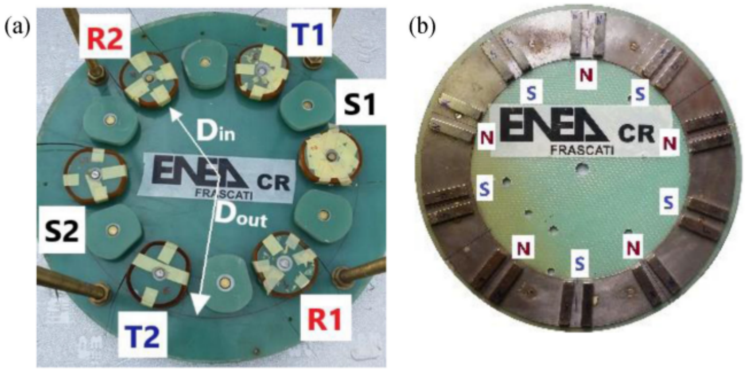

Fig. 2.12 Axial flux permanent magnet ironless prototype (a) stator and (b) rotor [11].

## 2.4.3 Fully Superconducting Prototypes

The first fully superconducting machines to have been developed employed low-temperature superconducting NbTi windings on both the armature and field excitation [116]. The authors were the first to propose a flux pumping system in SC electrical machines to excite field windings built with NbTi wires. The armature windings were constructed from twisted multifilamentary NbTi cables for AC applications to mitigate the effects of alternate excitation in the SC windings.

In the early 2000s, different research groups focused on induction superconducting machines investigation [117–119]. When constructed with superconducting rotor cages, this type of motor had the advantages of both an induction and synchronous machine in a unique device, i.e., starting torque, load-independent speed, etc.

The rotor bars and end rings of squirrel cage conventional squirrel-cage rotors from conventional induction machines are substituted by superconducting tapes to make a superconducting rotor cage. At the start up, the rotor currents have the same frequency of those in the stator windings, the induced currents cause high AC losses making the superconductors quench, i.e., exhibiting high resistivity. Consequently, the machine has a starting torque, and the motor starts as an induction machine. With the increased acceleration of the motor, the slip decreases, and the AC losses in SCs decrease due to the reduced frequency of the rotor currents. When the losses are low enough, the cage's superconducting state is restored, allowing the rotor to trap the linked magnetic flux and rotate at synchronous speed after a short transient stage. The potential for increasing torque density in superconducting machines has been demonstrated through the research on the partially superconducting induction-synchronous motor [120]. This partially superconducting induction motor employing a BSCCO rotor cage was later adapted to a fully superconducting machine rated 50 kW [12]. A ring winding configuration was chosen for the stator to improve the performance of the superconductor see Fig. 2.13. Due to the wide surface of the coil facing the radial direction of the stator, the critical current of the BSCCO tapes in the armature windings was enhanced with the reduction of the perpendicular magnetic field applied on the surface of the tape. The authors later demonstrated the feasibility of a fully superconducting prototype with a smaller stator using REBCO tapes (due to reduced bending radius) [121].

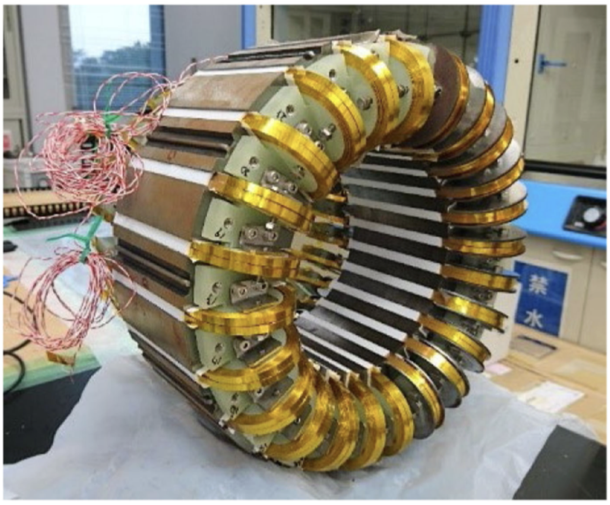

Fig. 2.13 Ring winding configuration of the superconducting stator of the fully superconducting HTS induction/synchronous machine [12].

## 2.5 Summary

The current challenges in the design and development of superconducting electrical machines are primarily focused on a) mechanical limitations, such as the minimum bending radius of SC tapes and transverse tensile stresses on SC tapes; b) the influence of AC losses on the SC performance; c) the complexity of the cooling system; and d) the cost of the superconducting material. The AC losses of superconductors are still the main barrier to applying SC material in electrical machines. While SC operates with minor losses under the DC regime, they experience significant losses under AC operation. This is critical when using SC for armature windings. The impact of superconducting AC losses not only influences the performance of electrical machines but also increases the requirements for the cryocooler [122].

Some researchers have proposed partial superconducting machines to avoid HTS armature windings or to use HTS tapes parallel to the slot leakage magnetic flux density to limit their AC losses. However, this is still a current state-of-the-art challenge for electrical machines.

Another way to explore the full potential of SC materials in electrical machines is by removing the typical iron core. This increases magnetic flux density and reduces machine weight, thus increasing specific power/torque. Air-core radial flux [123] and axial-flux fully and partially SC machines [7] are alternative solutions that may also contribute to developing high-specific power/torque machines. However, with the increased magnetic field, the critical current of SC drops, and the AC losses increase.

Therefore, air-core solutions require further study. Other solutions include researching new SC materials to mitigate AC losses and mechanical limitations and decrease the manufacturing cost of SC tapes. While YBCO and GdBCO tapes are some of the most commercialized SC tapes, MgB2 and iron-based SC are being researched to present low-cost and low AC loss alternatives for SC technologies [124].

The development of SC electrical machines is conditioned to the required cryocooler. While liquid nitrogen cooling is possible using HTSs, several studies indicate the use of liquid hydrogen for the cooling of SC machines due to the increased current capability of SC tapes and lower losses at 30K. In the Polaris project, a turbo-electric aircraft is designed considering an HTS power transmission powered by liquid hydrogen [125]. This project considers using LH2 as a fuel to propel the turbo-electric gas turbine and as a coolant for the SC machines. Using reverse-Brayton cycle cryocoolers, already used in aerospace applications, may allow a sustainable solution with high reliability and efficiency, as it can use the SC machines as a cold heat exchanger [126].

In brief, the question arising today is: what is needed to make HTS electrical machines advantageous?

- Designing HTS machines by including a dynamic variation of operating parameters, such as temperature, field excitation, amount of thermal load conducted to the cryogenic environment, etc.
- HTS machines for rewarding applications: for example, generators for large wind turbines and motors/generators for aircraft;
- Improving the performance of 2G HTS wires is a must. One needs to increase the operation window regarding higher critical temperature, magnetic field, and lower manufacturing cost.
- Reliability and economic efficiency of the cryogenic cooling system: HTS electric machines must achieve economic viability.

# Chapter 3

# Superconducting Modelling and Characterization

## 3.1 Introduction

This chapter reports the numerical models used in this work to describe the electromagnetic behaviour of high-temperature superconducting materials, considering their critical current dependence on the magnetic field and characteristic non-linear resistivity. The model for FEM simulations of coated superconducting tapes using the $T-A$ formulation with the thin sheet approximation, which considers only a single superconducting layer, is described in detail, and the methodology used throughout this work for calibrating superconducting tape FEM models with experimentally obtained DC voltage-current curves and measured AC losses is explained. A multilayer tape model is developed to analyze the influence of the copper layers on superconductor losses. The results for the proposed multilayer model are discussed, showing that for accurate loss estimation in 2G HTS tapes in the high current or high-frequency regime, models must consider the stabilizing copper layers losses since they can become significant. Analytic loss solutions in literature for transport and magnetization losses in superconductors are stated, and an analytical model for loss estimation in superconducting tapes that considers HTS hysteretic and resistive losses is proposed. Analytical and experimental results are compared to those of the developed numerical model, and their accuracy is discussed.

## 3.2 Numerical Models for HTS materials

Several formulations are available in the literature to model superconductors that can be distinguished by the state variables used to characterize them [44]. The majority of the available numerical models used for performance and loss estimation in HTS use the superconducting E-J power law, which will be introduced in this chapter, together with the $H-$formulation [127–129] or $A-$formulation [130, 131]. These models are applied to numerically solve complex electromagnetic superconducting systems with the magnetic field **H** or the magnetic vector potential **A** as state variables. Although these formulations can provide highly accurate results, they are typically time-consuming (especially when dealing with 3D geometries) due to the highly non-linear characteristic of HTS materials and the great detail that is imperative for precise estimation of losses in superconductors [43, 132, 133].

Recent studies show that a combination of two formulations, one for non-linear conductive regions (e.g., HTS) and another for linear conductive and non-conductive regions (e.g., copper and air), provides the same results with lower simulation times [43, 132, 134, 135]. This is the case of the $T-\phi$ formulation, solving for the current vector potential **T** and the scalar vector potential $\phi$ [136, 137], the $T-A$ formulation [134, 138, 139] and the $H-\phi$ formulation [132, 140]. The different variables used to construct the formulations numerically solve the Maxwell equations in the superconducting and surrounding domains defined in (3.1).

$$\nabla \cdot \mathbf{D} = q \qquad \nabla \cdot \mathbf{B} = 0 \qquad \nabla \times \mathbf{E} = -\frac{\partial \mathbf{B}}{\partial t} \qquad \nabla \times \mathbf{H} = \mathbf{J} + \frac{\partial \mathbf{D}}{\partial t} \tag{3.1}$$

In (3.1), **D** is the electric displacement, $q$ is the charge density, **B** is the magnetic flux density, **E** is the electric field, **H** is the magnetic field, and **J** is the current density. The electric displacement **D** and the magnetic field **H** are defined in (3.2).

$$\mathbf{D} = \varepsilon_0 \mathbf{E} + \mathbf{P} \qquad\qquad \mathbf{H} = \frac{\mathbf{B}}{\mu_0} - \mathbf{M} \tag{3.2}$$

Where $\varepsilon_0$ and $\mu_0$ are the vacuum permittivity and permeability and **P** and **M** are the polarization and magnetization. In superconducting formulations, these equations are solved in a quasi-magnetostatic regime, that is, under a slowly changing field, which allows neglecting electromagnetic radiation term, $\partial \mathbf{D}/\partial t$.

### 3.2.1 Superconducting electromagnetic properties

Analyses of superconducting materials and their respective applicability in electrical devices are usually done through numerical models used to describe the macroscopic properties of the material accurately. In purely electromagnetic models, superconductors are defined by their current-voltage/electric field characteristics and critical current density dependence on the external magnetic fields. These two descriptions can be combined and imposed in the superconducting material definitions, regardless of the geometry considered (i.e., coated conductors, cables, bulks). It allows for modelling the behaviour of the conductor under different conditions and estimating its performance and critical limits.

#### The Bean model

To bring forth a qualitative description of the superconducting state voltage-current function, C. P. Bean proposed a model based on the premise that the transport current inside the superconductor is fixed to the critical current (i.e., $I_c$) and independent of the external magnetic field [141, 142]. The model also takes the assumption that any external field penetrates the conductor from its edges, and wherever the conductor is penetrated, current will flow.

The model defines the current density in the superconductor as the critical current when the field penetrates the superconductor. The field penetrating the superconductor causes a local magnetic field variation, which induces an electromotive force, making current flow in the region. In an area of the material without field penetration, the current is null. This model is called the critical state model (CSM). The current in the superconductor is defined as in (3.3).

$$J = \begin{cases} 0, & \text{where } \frac{\partial B}{\partial t} = 0 \\ \pm J_c, & \text{where } \frac{\partial B}{\partial t} \neq 0 \end{cases} \tag{3.3}$$

The CSM description is not applicable when the magnetic field is perpendicular to the current direction in superconducting tapes since it neglects the effects of the magnetic field in the material current carrying capacity [143]. Nonetheless, it provides a qualitative description of the superconductor behaviour, and analytical loss models can be derived from the model assumptions.

### Critical Current Dependence on External Magnetic Field - Kim model

In this work, except for thermal model discussions in chapter 5, the superconducting formulations are mainly applied in electromagnetic environments, with a constant temperature of 77 K, at which the considered material parameters were experimentally determined. In type-II superconductors, the dependence of the critical current density $J_c$ on the applied magnetic field under constant temperature operation is defined by the Kim Model [144–146], stated in (3.4).

$$J_c(\mathbf{B}) = \frac{J_{c0}}{1+|\mathbf{B}|/B_0} \tag{3.4}$$

Where $J_{c0}$ is the critical current density at self-field and $B_0$ is the magnetic flux density that lowers $J_c$ by half, both of which depend on the material and operating temperature. The 2G HTS tape considered in this thesis has a very high aspect ratio between its thickness and width (4 mm width, 1.6 $\mu$m thick) and, thus, exhibits a strong anisotropic critical current dependence on the applied field orientation. This anisotropic behaviour can be included in the analyses with the modified Kim model that considers weighted parameters for each field component effect on the critical current as in (3.5) [147].

$$J_c(B_{\|}, B_{\perp}) = \frac{J_{c0}}{(1+\sqrt{k^2 B_{\|}^2 + B_{\perp}^2}/B_0)^{\beta}} \tag{3.5}$$

In (3.5), $\beta$ is the exponent of the field dependence of the critical current, and $k$<1 is the anisotropy factor. The components $B_{\|}$ and $B_{\perp}$ are the magnetic flux densities parallel and perpendicular to the widest tape surface, corresponding to $B_x$ and $B_y$ respectively, in Fig. 3.3. For simplicity, however, the first Kim model in (3.4) is considered in this thesis, where the magnetic field norm corresponds only to the magnetic field intensity on the normal direction to the superconductor tape since its effect is the most noticeable [67].

### Electric Field Dependence on the Critical Current Density

Although several models can be found in the literature to describe the electric field current density relation in HTS, the $E-J$ power law is the most used to describe the characteristic resistivity of the superconductor [148]. The relation, which is widely accepted as a macroscopic description for the superconductor resistivity, was first proposed to study the thermally activated flux creep regime, i.e. when flux lines are no longer pinned and move freely in the superconductor [149]. The non-linear $E-J$ power law is described in (3.6).

$$\mathbf{E} = E_0\left(\frac{|\mathbf{J}|}{J_c(\mathbf{B})}\right)^{n-1}\frac{\mathbf{J}}{J_c(\mathbf{B})} \tag{3.6}$$

In (3.6) $E_0$ is the critical electric field defined by convention as 100 $\mu$V/m that determines the critical current density, and $n$ is the superconducting n-value that determines the steepness of the transition to the resistive state (and can be used to interpret the tape quality). The effect of different $n$ values is shown in Fig 3.1.

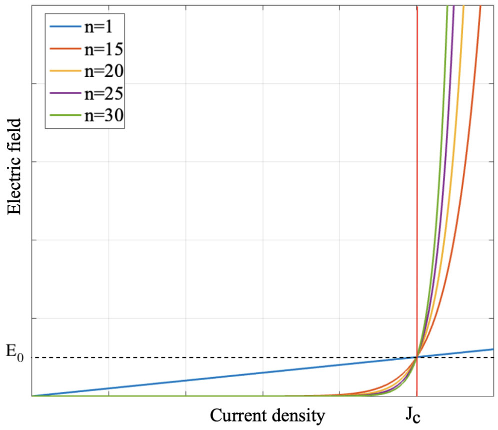

Fig. 3.1 Superconducting E-J power law behaviour for different $n$ values

Note that the limiting case in which $n \to \infty$ the power law approaches a step function corresponds to the Bean model description of superconductors.

## 3.3 The $T-A$ Formulation

The electromagnetic behaviour and AC performance of second-generation (2G) superconducting (SC) tapes are commonly analysed using finite element methods. Among the available formulations, the T-A approach is favoured due to its balance between accuracy and computational efficiency [44, 46]. This method simplifies the FEM model by assuming that all current is confined within the superconducting layer, treating it as a surface of negligible thickness. Consequently, the superconducting domain can be represented by the current vector potential, **T**, which is oriented in the normal direction to the tape's wide surface. The REBCO tapes considered in this study are commercially available high-temperature superconductors (HTS) from Superpower Inc.[73], comprising multiple material layers, as illustrated in Fig.3.2. Given the high aspect ratio of coated conductor tapes—where the width (4 mm) is significantly greater than the thickness (95.6 $\mu$m, see Fig.3.2), other layers, such as copper, silver, and the steel substrate, are omitted, and their associated losses are disregarded. This assumption remains valid for operating conditions where the supply frequency does not exceed 150 Hz and the current remains below the critical threshold when the current will flow mainly in the superconducting layer, making the losses on the remaining conducting elements negligible [150, 13]. Under these conditions, losses arising due to the skin effect in the copper and silver layers are also neglected, and the model complexity is greatly reduced.

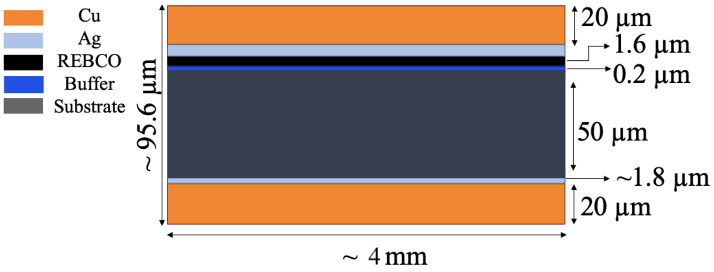

Fig. 3.2 Illustration of a REBCO tape several materials and layers with their respective dimensions

The numerical model is constructed by defining in the tape domain, the potential vector **T**, and in all other domains $\Omega_A$ the magnetic vector potential **A**, as in (3.7).

$$\nabla\times\mathbf{T} = \mathbf{J},\ \text{in}\ \Omega_{SC} \qquad \nabla\times\mathbf{A} = \mathbf{B},\ \text{in}\ \Omega_A \tag{3.7}$$

Considering a 3D environment, the potential vector **T** is defined as stated in (3.8).

$$\begin{bmatrix} J_x \\ J_y \\ J_z \end{bmatrix} = \begin{bmatrix} \frac{\partial(\mathbf{T}\cdot\mathbf{n}_z)}{\partial y} - \frac{\partial(\mathbf{T}\cdot\mathbf{n}_y)}{\partial z} \\ \frac{\partial(\mathbf{T}\cdot\mathbf{n}_x)}{\partial z} - \frac{\partial(\mathbf{T}\cdot\mathbf{n}_z)}{\partial x} \\ \frac{\partial(\mathbf{T}\cdot\mathbf{n}_y)}{\partial x} - \frac{\partial(\mathbf{T}\cdot\mathbf{n}_x)}{\partial y} \end{bmatrix} \tag{3.8}$$

The model complexity is significantly reduced when the $T-$formulation is used to model coated conductor HTS tapes with the thin sheet approximation. The

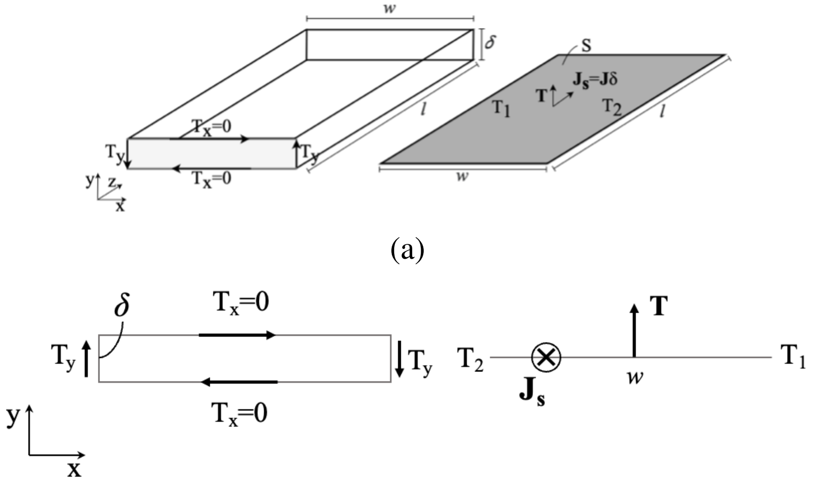

(a)

(b)

Fig. 3.3 Illustration of a REBCO tape and its form with the thin sheet approximation on the surface (right) and important variables in (a) 3D and (b) 2D.

potential vector **T** is defined only in the normal direction to the tape since the current can be assumed to flow in the conducting layer tangentially to the widest plane of the tape [151–154, 137] as is illustrated in Fig. 3.3. This reduces the need for very fine mesh along the thickness of the tape and reduces the number of dimensions to solve by defining the variables according to the tape normal vector **n** and solving (3.8). The $T-$formulation and $A-$formulation allow solving Faraday's law, also implemented in FEM (3.9) [155].

$$\begin{bmatrix} \frac{\partial E_z}{\partial y} - \frac{\partial E_y}{\partial z} \\ \frac{\partial E_x}{\partial z} - \frac{\partial E_z}{\partial x} \\ \frac{\partial E_y}{\partial x} - \frac{\partial E_x}{\partial y} \end{bmatrix} \mathbf{n} + \begin{bmatrix} \frac{\partial B_x}{\partial t} \\ \frac{\partial B_y}{\partial t} \\ \frac{\partial B_z}{\partial t} \end{bmatrix} \mathbf{n} = 0 \tag{3.9}$$

Note that when using the $T-$formulation, the component of **B** that is parallel to the broad face of the conductor is neglected due to using the thin sheet approximation, which simplifies (3.9) [151, 153]. Dirichlet boundary conditions are defined at the tape edges to impose the tape current. To obtain the conditions at each edge of the tape $T_1$ and $T_2$, the Stokes theorem is applied to the definition of the potential vector

**T** as in (3.10).

$$\iint_S \mathbf{J}\cdot\mathbf{n}\,dS = \iint_S (\nabla\times\mathbf{T})\cdot\mathbf{n}\,dS = \oint_L \mathbf{T}\,dl = (T_1 - T_2)\delta \tag{3.10}$$

In (3.10) $L$ denotes the path formed by the boundary edges of the conductor, and $\delta$ is the thickness of the superconductor layer.

### 3.3.1 2D Single Tape Model

In the 2D model, the $T-A$ formulation is applied in FEM to model the simplest case of a single tape of infinite length surrounded by an air domain. The model geometry is shown in Fig. 3.4. In the 2D FEM model, a line of 4 mm width is added to model the HTS tape. Hence, the characteristic equations are defined in the SC domain, and the $T-$formulation is applied. In the air, the $A-$formulation is applied. In commercial finite element software, the defining equations are solved using a General Form Boundary PDE module to define the $T-$formulation and the magnetic fields physics for $A-$formulation (COMSOL Multiphysics®).

The 2D tape model is studied for the case of a tape with an imposed alternate current to analyse the accuracy of the model for AC loss estimation and perform a model calibration. In this model, a sinusoidal current function is imposed on the tape $i(t) = I_m \sin(\omega t)$. For this, the variables $T_1$ and $T_2$ are defined on one edge as 0 and $I_t/\delta$ on the other, where $I_t$ is the imposed current function. For all current values, the superconductor loss $P$ (W/m) is computed in FEM with the instantaneous power $p(t)$ as in (3.11), where $w$ is the width of the tape (4 mm), and $T = 1/f$ is the period of the current waveform.

$$p(t) = \int_w (\mathbf{J}\delta)\cdot\mathbf{E}\,dw, \qquad P = \frac{1}{T}\int_0^T p(t)dt \tag{3.11}$$

In HTS analyses, some detail is necessary to ensure accurate results and model convergence. The defined mesh for the tape model is shown in Fig 3.5. The entire mesh has a total of 3894 elements. The mesh applied in the air domain is triangular, and a linear mesh is defined in the superconducting tape. The mesh is specified with 100 edge elements distributed along the width of the line. A higher number of mesh points are concentrated at the tape edges to improve convergence since the current will penetrate the tape from its edges. Figure 3.6a illustrates how the current

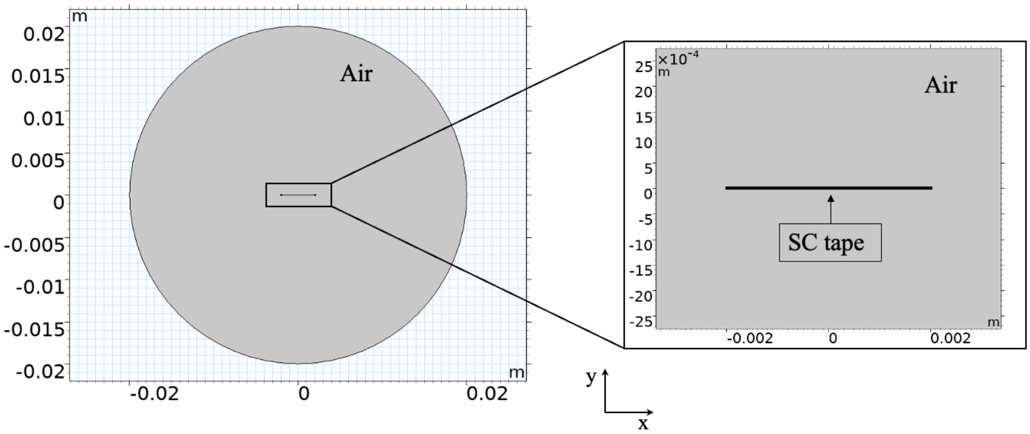

Fig. 3.4 2D model geometry showing single tape surrounded by air domain

is distributed across the width of the tape at various simulation times, showing that with increasing time and current amplitude, the current penetrates deeper into the tape width. The associated current waveform and AC losses of the tape are depicted in Fig. 3.6b.

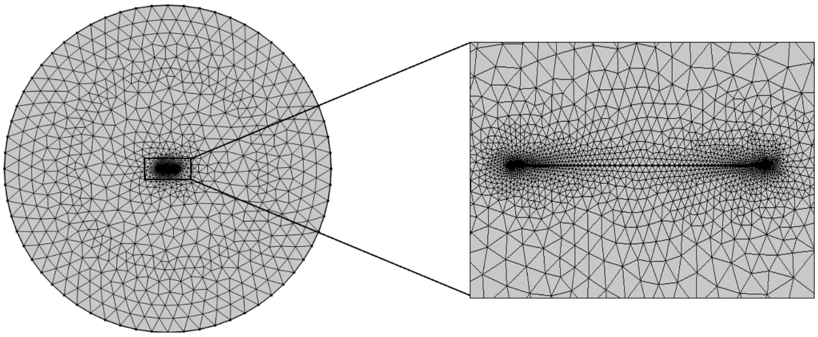

Fig. 3.5 2D model triangular mesh, the mesh of the tape is defined by 100 edge elements with exponential growth at tape edges

### 3.3.2 Experimental Calibration of the Tape Models

The FEM model calibration is achieved with DC and AC measurements, with the voltage-current characteristics of the superconducting tape measured using a direct current (DC) power supply and the hysteresis losses measured using alternate current excitation.

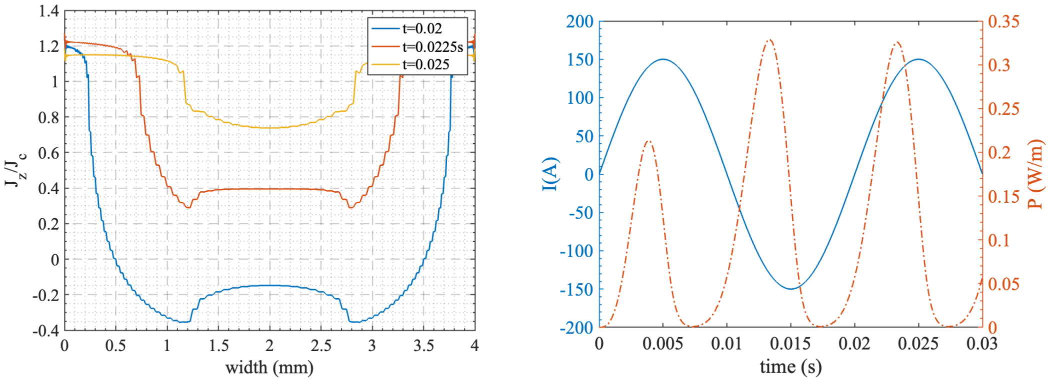

(a) (b)

Fig. 3.6 Simulation results for applied sinusoidal current $I_m$=150 A, $f$=50 Hz (a) current distribution for different times (b) current waveform and AC losses.

## DC Characterization

The primary objective of the DC test was to experimentally ascertain the critical current value ($I_c$) for the given superconducting tape, shown in Fig. 2.5b. Two Delta Eletronika SM-500-CP-90 bidirectional DC power supply impose currents from 0 to 170 A. The sources (each with a maximum current of 90 A) were connected in parallel to achieve the required current for the test. The voltage drop across the superconducting tape was then measured using an HP 34401A multimeter, capable of providing measurements with an accuracy up to $10^{-6}$ V. The results are plotted in Figure 3.7, illustrating the non-linear resistivity characteristic of the REBCO tape and its transition between the superconducting to the resistive state.

The critical DC current value $I_{c0}$ was determined by identifying the intersection point between the black dashed line, representing the critical electric field of $10^{-4}$ V/m, and the measured E-J curve. For the examined REBCO tape, this critical DC current value ($I_c$) at self-field is 162 A with an n-value of 28. The measured critical current matches the data provided by the manufacturer for the considered 30 m length tape (equal to 162 A, with a minimum guaranteed value of 158 A, see Appendix A). In Fig 3.8, the tape is shown inside an Expanded Polystyrene (EPS) foam container and submerged in a liquid nitrogen bath for the measurements. Also shown in the figure are the details of the voltage probe and the current supply at the edges of the REBCO tape.

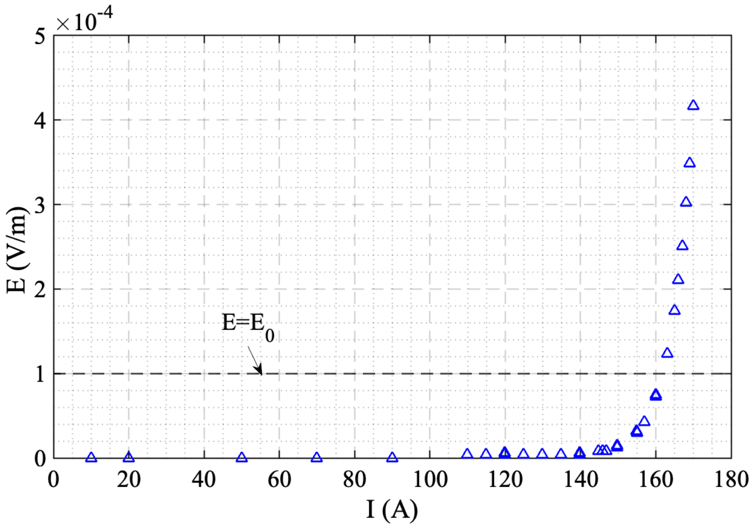

Fig. 3.7 E-J curve measured by the dc test at 77K on the REBCO tape

### AC Characterization

The hysteretic behaviour and the AC loss characteristic of the HTS material was observed under alternate current excitation. The measurement circuit is depicted in Fig. 3.9, and the measurement setup is shown in Fig. 3.10. The HTS tape was connected to the secondary side of a transformer connected to an alternate power supply. A turn ratio equal to 100:1 was necessary to adapt the voltage and current values generated by the sinusoidal power supply for the tape test. Unlike the DC measurements, in AC, the measured voltage in the superconductor has two components: a resistive component and an inductive component [13]. The electrical measurement of AC losses is based on determining the voltage component in phase with the current. While the resistive part of the voltage is related to the hysteresis losses of the tape, the inductive part is caused by the closed loop formed by the tape and the voltmeter. The flux and voltage components in the superconducting tape are stated in (3.12) and (3.13).

$$\Psi(t) = \Psi_{int}(t) + \Psi_{ext}(t) \tag{3.12}$$

$$v_{SC}(t) = Ri(t) + \frac{d\Psi(t)}{dt} \tag{3.13}$$

In 3.12, the 'internal' magnetic flux $\Psi_{int}$(t) is the leakage flux affecting the SC and contributing to the non-linear self and mutual inductance between the coated

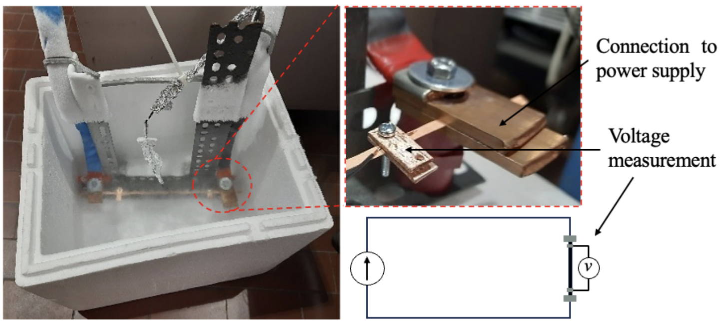

Fig. 3.8 REBCO tape in the LN2 bath with detail of the copper plates used for the voltage drop measurement (1) and for connecting at the power supply (2) and electric circuit schematic for the DC measurement.

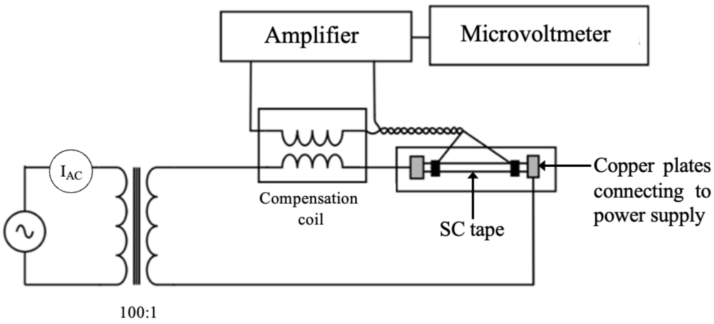

Fig. 3.9 Circuit for AC loss measurements on the superconducting tape.

conductor layers inside the tape [156]. The 'external' $\Psi_{ext}(t)$ is the magnetic flux linked with the voltmeter connection.

$$\Psi_{int}(t) + \Psi_{ext}(t) = \Psi_{int}(t) + L_{ext}i(t) \tag{3.14}$$

It is worth mentioning that $\Psi_{int}(t)$ presents a non-linear behaviour because of the hysteretic phenomenon that affects the current distribution in the superconducting layer [157]. Only the resistive component in (3.13) must be considered to compute the AC losses on the SC tape. Therefore, a compensation coil with adjustable mutual coupling minimizes the inductive voltage component, which can be significantly higher than the in-phase AC loss contribution [158]. Alternatively, the electric measurement can be performed with a lock-in amplifier to determine the losses when the voltage and current phase difference is close to zero. The magnetic flux $\Psi(t)$ in

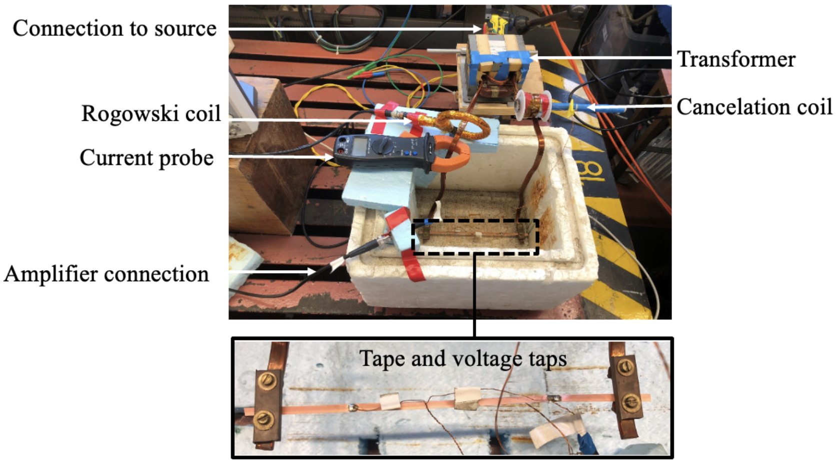

Fig. 3.10 Setup for AC loss measurements on the superconducting tape with detail of the superconducting ReBCO tape.

the HTS tape can be written as in (3.15), where M is the mutual inductance of the compensation coil.

$$\Psi(t) = \Psi_{int}(t) + (L_{ext} - M)i(t) \tag{3.15}$$

The AC losses per unit length are obtained by the average value of the instantaneous power as in (3.16), where $l$ is the distance from the voltage pick-up taps [159].

$$P_{ACmeasured} = \frac{1}{lT}\int_0^T v_{SC}(t)i(t)dt \tag{3.16}$$

The measured AC losses are compared to those obtained by the FEM model of the SC tape for different values of $n$ and $B_0$ as shown in Fig. 3.11. The parameter set of the red curve in Fig. 3.11 allows to achieve with the FEM a good approximation of the measured values. Therefore, the parameters shown in Table 3.1 have been used for the calibrated FEM model. Note that since the tape AC and DC characteristics differ, when the tape is characterized in AC, its behaviour is better described with a lower n-value than that determined in DC conditions. However, Fig. 3.11 presents the losses in a logarithmic scale; hence, for low current values, the FEM computation underestimates the losses, and care must be taken when designing practical superconducting devices and estimating the respective cooling system requirements.

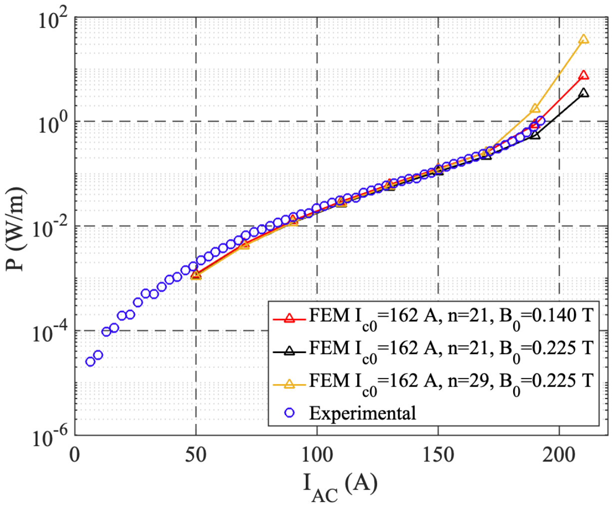

Fig. 3.11 Comparison between FEM and experimental AC losses per unit length at T=77 K and f=50Hz for the measured superconducting REBCO tape.

Table 3.1 ReBCO Tape Main Parameters

| $I_c$ | $B_0$ | $T_c$ | $n$ | width | height | SC layer height |
|---|---|---|---|---|---|---|
| 162 A | 140 mT | 119 K | 21 | 4.01 mm | 95.6 $\mu$m | 1.6 $\mu$m |

Note that for the measured current values, the supply current was limited to 175 A to avoid quenching the HTS tape. Nonetheless, the proximity between experimental and modelled losses allows validating the FEM model and estimate the tape parameters.

## 3.4 Electromagnetic Modelling of the Copper Layers Influence for AC Losses in ReBCO

Usually, coated conductor HTS models consider only the superconducting layer presence, as the path has the lowest resistivity in the tape. However, for sufficiently high frequencies of externally applied fields ($f$>150 Hz), the skin effect in the copper must be considered when computing the loss in the coated conductor tape [150]. Furthermore, at high currents ($I$>$I_c$), the superconducting layer will go into its resistive state with its resistivity increasing by a power law function (if temperature is assumed constant). In this situation, the remaining layers of the tape, which are

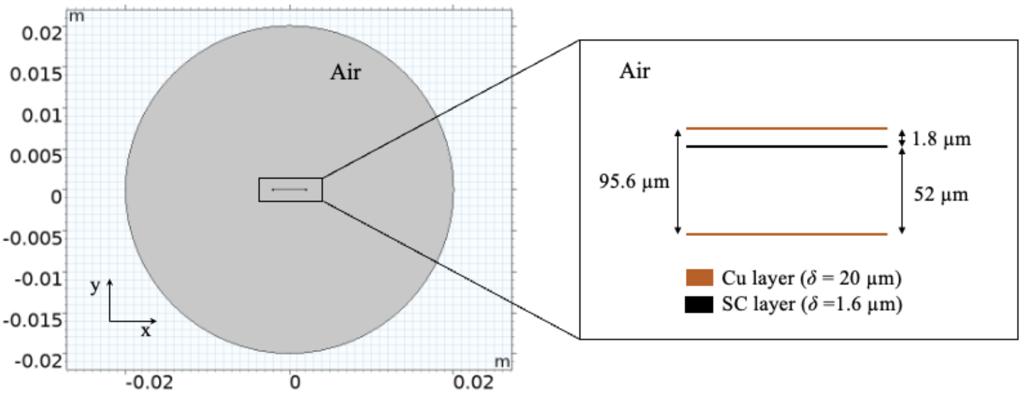

Fig. 3.12 2D geometry of the model of the coated conductor tape considering the influence of copper layers.

connected in parallel, can also carry current. The imposed current will flow into the copper stabilizing layers, providing a similar (or lower) resistivity path at cryogenic temperatures and contributing to the losses. If the conditions of electromagnetic study are such that the thin sheet approximation to model the HTS tape as a single superconducting layer is no longer applicable, the $T-$formulation can be applied in FEM to model the remaining layers of the coated conductor. This allows to better identify optimal operating conditions for 2G tapes in electrical devices. The assumptions of the approximation, which are mainly related to the very small thickness of the conducting tapes [153, 154, 137], can be applied to the other conducting materials of the multilayered conductor (which similarly have a very high aspect ratio between the layer width and thickness). In these conditions, the $T-$ formulation is applied to the coated conductor layers, mainly contributing to the tape losses: the superconducting and copper stabilizing layers [150, 13]. The model assumes that the current flows tangentially to the widest surface of the tape in all layers and that the tape operates in fully cryogenic conditions. In the superconducting domains, the material characteristics for the superconducting HTS material are defined. In the copper domains, the electric field and current relation is determined by the copper resistivity at the cooling fluid temperature $\rho_{77K} = 0.233\times10^{-9}$ Ωm at 77 K ($LN_2$ temperature). The specifications of the REBCO tape are those determined by experimental calibration, for which data is stated in Table 3.1. The 2D multilayer model geometry showing the several layers and dimensions is depicted in Fig. 3.12. Note that in this figure, the several layers are separated by air, and distance between layers is defined according to the specifications of the tapes available for experimenting [73].

New boundary conditions must be added in the $T-$ formulation to consider the several layers of the tape connected in parallel. The law of current conservation is added in FEM as a global constraint, stated in (3.17), ensuring the supplied current can be shared between layers.

$$\int J\delta_{SC}\, d\Omega_{SC} + \int J\delta_{Cu}\, d\Omega_{Cu} = I_T \tag{3.17}$$

In (3.17) $I_t$ is the transport current, $\delta_{SC}$ is the superconducting layer thickness, 1.6 $\mu$m and $\delta_{Cu}$ is each of the copper layers thickness, 20 $\mu$m for the considered tape. The integral in the copper domains must include both copper layers. Thus, it is, in fact, an integration of two different (copper) domains. Only one Dirichlet boundary condition for imposing current is defined at one edge of each layer, superconducting, and copper, as $T_1 = 0$, while the previous Dirichlet condition $T_2$=$I_T/\delta$ is substituted by the global model constraint. This means that there will be an open boundary for the HTS layer. Nonetheless, the global condition for sharing current will ensure that the total current in the three layers is the same as the defined applied current. However, it is also necessary to consider that all layers are in parallel, i.e., with the same voltage or average electric field.

Using the definition of the current vector potential **T**, by Stokes' theorem, the result in (3.10) can be used to define the total electric field in each layer of the tape. The electric field in the tape **E** will be the sum of an induced component and an applied component, such that (3.18).

$$\mathbf{E} = \mathbf{E}_{ap} + \mathbf{E}_{ind} \tag{3.18}$$

However, when integrating **E** in the layer width, the induced component of the electric field is cancelled since its contribution is antisymmetric across the tape width, hence only the applied electric field is considered as in (3.19) and (3.20).

$$\int (E_{apSC} + E_{indSC})\, dw_{SC} = \int E_{apSC}\, dw_{SC} \tag{3.19}$$

$$\int (E_{apCu} + E_{indCu})\, dw_{Cu} = \int E_{apCu} dw_{Cu} \tag{3.20}$$

In (3.19) and (3.20), the subscripts *SC* and *Cu* stand for the HTS and copper layers. When the current density is described by (3.21), the induced components along the width of the tape are also cancelled, giving the relation in (3.22).

$$E_{Cu} = \rho_{Cu} J_{Cu} = \rho_{Cu} \int (J_{apCu} + J_{indCu})\, dw_{Cu} \tag{3.21}$$

$$\int E_{Cu} dw_{Cu} \;=\; \int E_{apCu}\, dw_{Cu} \;=\; \rho_{Cu} \int J_{apCu}\, dw_{Cu} \tag{3.22}$$

Therefore, the same applied electric field can be imposed in the SC and copper layers as shown in (3.23). Using the definition in (3.10) and (3.23), the Dirichlet boundary condition at the edge of the copper layer according to $T-$ formulation, ensuring the same electric field is present in all the tape layers, is defined as in (3.24).

$$\int E_{apSC}\, dw_{SC} \;=\; \int E_{apCu}\, dw_{Cu} \;=\; \int J_{apCu}\, dw_{Cu} \;=\; \rho_{Cu} I_{ap}/\delta_{Cu} \tag{3.23}$$

$$T_{Cu} = I_{ap}/\delta_{Cu} = \frac{1}{\rho_{Cu}} \int E_{apSC}\, dw_{SC} \tag{3.24}$$

Note that to guarantee a good model convergence, the electric field in the copper tapes can be defined as in (3.25) in the FEM model. Nonetheless, this is equivalent to the definition in (3.24), due to the definition of the **T** current vector potential in the $T-$formulation (see Fig. 3.3). The **T** is defined normal to the surface, and thus when the integral in (3.25) is calculated, it corresponds to the value of **T** at the point, that is $T_{Cu}$.

$$\int T\, dw_{Cu} = \frac{1}{\rho_{Cu}} \int E_{apSC}\, dw_{SC} \tag{3.25}$$

The definition in (3.25) is added as a Dirichlet boundary condition in each copper tape end. In Fig 3.13, an illustration of the model definitions and variables is depicted.

It is essential to achieve accurate results to define a mesh with a minimum spacing in the copper tapes smaller than the characteristic skin depth of the copper, $\delta_{SE}$, (for the imposed frequency). Hence, depending on the frequency of the externally applied field or imposed current, the minimum length between two edge elements in copper must be calculated according to (3.26) [160].

$$\delta_{SE} = \sqrt{\frac{2\rho}{\omega\mu}} \tag{3.26}$$

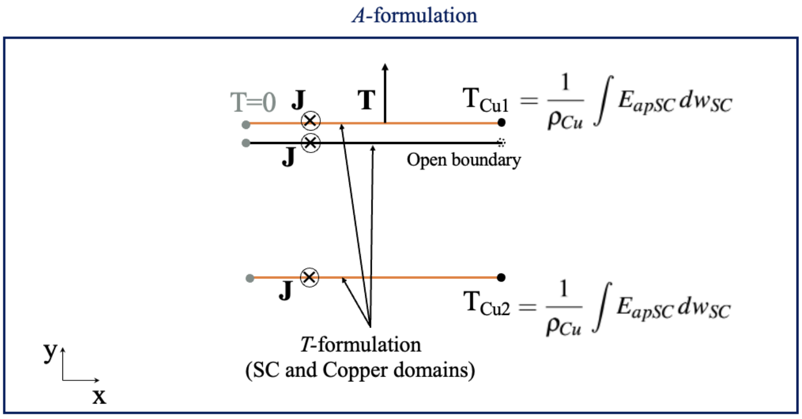

Fig. 3.13 Illustration of the 2D multilayered tape model defined conditions in the superconducting and the copper layers.

In (3.26), $\rho$ is the resistivity of the conductor, $\omega$ is the angular frequency of the current $2\pi f$, $\mu$ is the permeability of the conductor, and $\varepsilon$ is the permittivity of the conductor. For copper, a skin depth is considered to simulate frequencies up to $10^5$ Hz, for comparison with results in [150]. The corresponding $\delta_{SE}$ is $7.6\times 10^{-6}$ m. For this effect, the defined mesh in copper is the same as in the HTS layer. A mesh of 100 edge elements with the exponential growth of factor 25 from the edges to the centre is defined in all layers, which admits a distance between mesh points up to $1\times10^{-6}$m.

## 3.5 Analytical Models

For coated conductor tapes under the effect of applied alternate field or alternate current, there are analytical solutions for both transport current losses proposed by Norris [161] and Fernandes [13] and magnetization losses, proposed by Brandt [143]. In this work, superconducting tapes are investigated for application in electrical machine armature windings. Hence, these analytical calculations are used in applicable cases for validation of the FEM models for loss estimation.

### 3.5.1 Norris Model

The result proposed by Norris provides an analytical solution for transport losses in hard superconductors under self-field conditions. The model neglects the effect of the external magnetic field on the critical current density by applying the assumptions of the critical state model. The tape loss solution is obtained by determining the current inside the superconducting slab, considering that whatever current arises in the superconductor appears first at the outer regions of the tape and then gradually penetrates the inner area of the tape. The power dissipation is proportional to the supply frequency and is considered a hysteretic phenomenon. The expression for a 1G tape, with elliptical cross-section, is given in (3.27) and for a thin slab in (3.28) [161].

$$P_{EN} = \frac{\mu_0 f I_{c0}^2}{\pi}[(1-i)\ln(1-i)+(2-i)\frac{i}{2}] \tag{3.27}$$

$$P_{TN} = \frac{\mu_0 f I_{c0}^2}{\pi}[(1-i)\ln(1-i)+(1+i)\ln(1+i)-i^2] \tag{3.28}$$

In (3.27) and (3.28) $i<1$ is the ratio between the transport current and the critical current at self-field, $I_t/I_{c0}$ and $f$ is the supply current frequency. The subscripts $EN$ and $TN$ represent elliptical and thin strip solutions, respectively.

### 3.5.2 Extended Norris and Sigmoid model

The solution given by Norris is only valid until the saturation point of the SC tape for the amplitude of the applied current $I<I_c$. For $I \geq I_c$, the critical state model is no longer applicable; therefore, neither is the Norris solution. According to the critical state model, the maximum permissible current inside a superconducting specimen would be $J_c \cdot A_S$, where $A_S$ is the cross-section of the superconductor, and this case corresponds to that when the material is carrying a current equal to its critical current $I_c$.

However, superconductors can carry currents superior to their critical current, albeit with a non-negligible resistivity. A solution is proposed to estimate losses in the superconducting tapes in an overcritical regime ($I \geq I_c$) when the total losses in the conductor are the sum of the hysteresis losses (accounted for in the Norris model) and the resistive losses due to the resistive behaviour of the HTS tape at sufficiently high currents[13]. This extended model also considers the influence of the self AC and external DC fields on the critical current of the tape, which is not considered in the Norris model.

The $E-J$ power law is used to estimate the resistive losses that add to the hysteresis losses already present in the tape, accounting for the resistance increase. This result is derived initially from the Norris losses in the hysteretic region where $I<I_c$. When the tape carries a current $I=I_c$, then $i \rightarrow 1$ and the losses are written as in (3.29) and (3.30).

$$P_{EN} = \frac{1}{2}\frac{\mu_0 f I_{c0}^2}{\pi} \tag{3.29}$$

$$P_{TN} = \frac{\mu_0 f I_{c0}^2}{\pi}\left(\ln(4)-1\right) \tag{3.30}$$

When the superconducting tape enters the resistive regime, at currents $I \geq I_c$, the HTS resistive losses are obtained from the $E-J$ power law as stated in (3.31) [13].

$$P_{resistive} = \frac{1}{T}\int_0^T \frac{E_c}{I_c^n} \cdot I(t)^{n+1}\, dt = \frac{1}{2\pi}\frac{E_c}{I_c^n} I_m^{n+1} \int_0^{2\pi} \cos^{n+1}(\theta)\, d\theta \tag{3.31}$$

In (3.31), $I(t)$ is the imposed current in the tape, $I_m\cos(\omega t)$ and $\theta = \omega\, t$. The solution to the integral in (3.31) is stated in (3.32).

$$\int_0^{2\pi} \cos^{n+1}(\theta)\, d\theta = \frac{\pi}{2^n}\frac{(n+1)}{(\frac{n+1}{2}!)^2} \tag{3.32}$$

The expression for the resistive losses becomes (3.33), and therefore, the total losses at $I \geq I_c$ for 1G tapes are defined as in (3.34) and for 2G coated conductors as in (3.35).

$$P_{resistive} = \frac{i^{n+1}\, I_c\, E_c}{2^{\,n+1}}\frac{(n+1)!}{(\frac{n+1}{2}!)^2} \tag{3.33}$$

$$P_{EF} = \frac{1}{2}\frac{f\mu_0 I_c^2}{\pi} + \frac{i^{n+1} I_c E_c}{2^{n+1}}\frac{(n+1)!}{\left(\frac{n+1}{2}!\right)^2}, \qquad \Gamma = min(i,1) \tag{3.34}$$

$$P_{TF} = \frac{f\mu_0 I_c^2}{\pi}(\ln(4)-1) + \frac{i^{n+1} I_c E_c}{2^{n+1}}\frac{(n+1)!}{\left(\frac{n+1}{2}!\right)^2}, \qquad \Gamma = min(i,1) \tag{3.35}$$

In (3.34) and (3.35), the subscripts $EF$ and $TF$ stand for elliptical and thin strip solutions, respectively. Since the $n$ number is typically high in HTS, the expression for $P_{resistive}$ can also be used to compute the tape transport losses when $I < I_c$. Hence, the general analytical result for the tape losses can be formulated as stated in (3.36) and (3.37) for 1G and 2G tapes, respectively.

$$\begin{aligned} &P_{EF} = \frac{f\mu_0 I_c^2}{\pi}\left[(1-\Gamma)\ln(1-\Gamma)+(2-\Gamma)\frac{\Gamma}{2}\right] + \frac{i^{n+1} I_c E_c}{2^{n+1}} \frac{(n+1)!}{\left(\frac{n+1}{2}!\right)^2}, \\ &\Gamma = min(i,1) \end{aligned} \tag{3.36}$$

$$\begin{aligned} &P_{TF} = \frac{f\mu_0 I_c^2}{\pi}\left[(1-\Gamma)\ln(1-\Gamma)+(1+\Gamma)\ln(1+\Gamma)-\Gamma^2\right] + \frac{i^{n+1} I_c E_c}{2^{n+1}} \frac{(n+1)!}{\left(\frac{n+1}{2}!\right)^2}, \\ &\Gamma = min(i,1) \end{aligned} \tag{3.37}$$

The hysteresis losses from the Norris model are used to compute losses relative to $I < I_c$, and the resistive losses are used for $I \geq I_c$. Thus, the analytical result is defined by branches. This discontinuous loss function creates the illusion of a "knee" point on the losses evolution, as a function of the current, in the transition between the hysteretic and resistive zones as shown in Fig. 3.14 [13]. For a solution without discontinuity effects, the losses in the superconducting tape can be characterized by a Sigmoid function (3.38) for both 1G and 2G superconductors, making a smoother transition between the hysteretic and resistive modes. This sigmoid analytical model presents a unique and continuous function for all ranges of current amplitudes. It is to be noted that while the extended Norris model analytical solution is applicable for tapes with known critical current, the sigmoid model parameters must be calibrated with experimental measurements on AC losses to provide a well-fitted continuous solution.

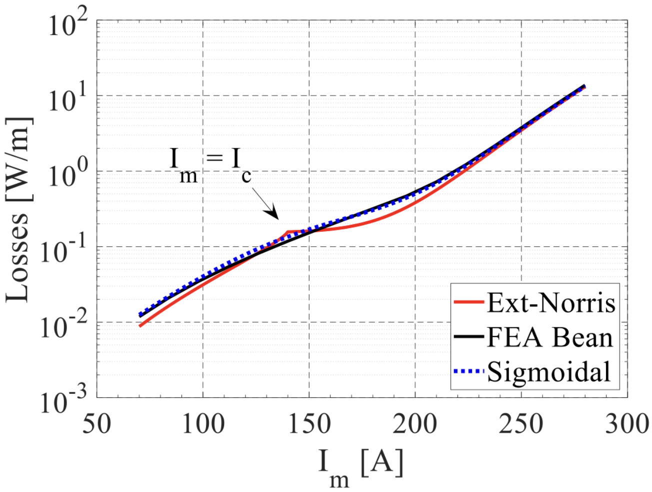

Fig. 3.14 HTS losses (W/m) for different amplitudes of magnetizing current $I_m$ for a tape with $I_c$ = 140 A and $n$ = 11, considering extended-Norris, sigmoid (a=0.8, b=5 and c=1.25) and FEA Bean models [13].

$$P_S = \frac{f\mu_0 I_c^2}{\pi}\left(\frac{a}{(1+\exp(-b(i-1)))^c}\right) + \frac{i^{n+1} I_c E_c}{2^{n+1}} \frac{(n+1)!}{\left(\frac{n+1}{2}!\right)^2} \tag{3.38}$$

In (3.38), the parameters $a$, $b$, and $c$ are found for elliptical and thin strips with experimental measurements of AC transport loss. The solution for the HTS losses can be used to determine the HTS resistance in 1G and 2G tapes for a given transport current. However, when the current density is such that the resistivity of the superconductor is increased beyond that of the stabilizing materials (e.g., copper or silver) at the cooling fluid temperature, the solution for the tape loss computation can be found using an equivalent circuit to accurately determine each material loss contribution [156]. The representation of the equivalent circuit for a 2G HTS tape is shown in Fig. 3.15 [13].

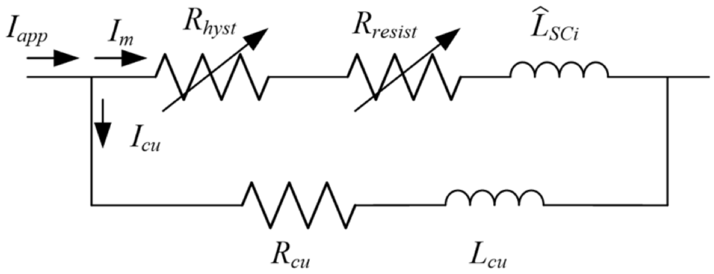

Fig. 3.15 2G HTS tape equivalent circuit considering the superconducting and copper layers [13].

The resistance of the HTS layer can be found from the loss contribution as $P_{HTS} = I_m^2(R_{hyst} + R_{resis})$, and its inductance is computed from the average inner flux in half of the HTS layer, $\lambda' = \frac{w}{2}B_{av}$ for the considered current. The contribution of the copper layer can be found in the resistivity of copper at cryogenic temperatures; in this case, $\rho_{Cu}=0.233\times10^{-8}$ Ωm and its inductance is calculated using rectangular conductor theory. The parameter determination is described in detail in [13].

### 3.5.3 Brandt Model

When superconductors are exposed to externally applied alternate magnetic fields, they manifest magnetization losses. Brandt derived this loss contribution for superconductors when the magnetic field is applied in the transverse direction to the tape, in (3.39) [143]. Notice that transverse refers to the direction transverse to the wide face of the tape (in REBCO, the 4 mm wide face) and the current flowing direction, not to be confused with the direction transverse to the tape height. The magnetization loss in superconductors has a hysteretic nature. Since the superconductor tends to retain its magnetized state due to flux pinning, as soon as the applied field varies, the magnetization state changes and energy is spent to override the previous magnetization state.

$$P_B = \mu_0 w^2 f J_c \delta H_0 \, g\left(\frac{H_0}{H_c}\right) \tag{3.39}$$

In (3.39) $w$ is the width of the conductor, $f$ is the frequency of the applied magnetic field and $H_0$ its amplitude, $H_c$ is the characteristic field, $I_c/w\pi$, and $g(x)$ is given by (3.40).

$$g(x) = (2/x)\ln\cosh(x) - \tanh(x) \tag{3.40}$$

## 3.6 Numerical and Experimental Results

### 3.6.1 DC Current

Using the experimentally determined parameters for the REBCO tape 3.1, the single tape and multilayer models were compared for different case studies. The single-layer and multilayer models were simulated with varying amplitudes of imposed DC current. The current is defined in FEM by a step function between 50 and 260 A of imposed current $I_{DC}$ for both the single-layer and the multilayer coated conductor model. The electric field results for different current amplitudes are plotted in Fig. 3.16.

The results show that the thin sheet approximation and the multilayer model have the same results for low current amplitudes. This similarity indicates that the superconducting layer carries current until values are higher than the critical limit (162 A). However, the curves have different evolutions in the high current region. In this high current regime, there is current sharing between the copper and the superconducting. This is due to the SC resistivity increase, making it comparable to or even higher than that of copper at 77 K, while the thin-sheet approximation follows the $E-J$ law.

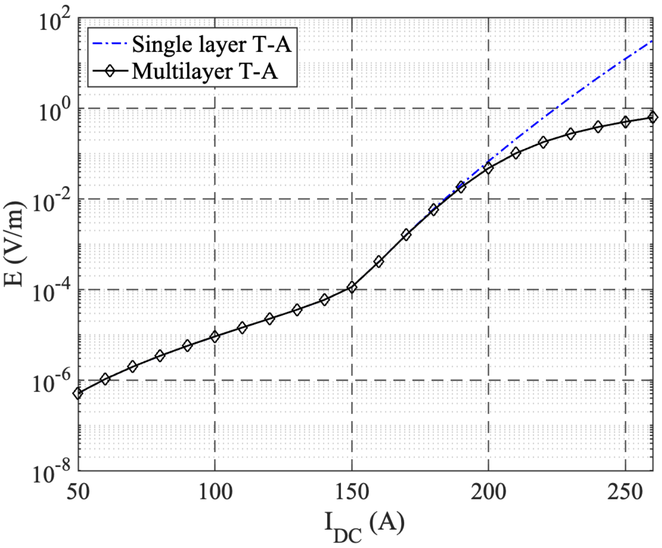

Fig. 3.16 Electric field in the SC layer vs current for the multilayer and single layer models supplied in DC.

### 3.6.2 Transport Current AC Losses

In Fig. 3.17, the numerical AC loss results are plotted for different current amplitudes supplied to a single tape under an alternate current supply at a 50 Hz frequency. The single layer and multilayer models are compared with the homogenized model in [162]. Experimental results and analytical results of the Norris and extended Norris model solution with an equivalent circuit are also compared. Note that as mentioned in 3.3.2, the supply current was limited to avoid quenching the tape, hence it is difficult to analyze the proximity between results in the overcritical regime when the different contributions from the tape layers should be noticeable. Nonetheless, all FEM models show good agreement with experimental data below the overcritical regime. The main difference between the single-layer, homogenized and multilayer models is shown above 175 A, when the superconducting layer starts to have a considerable resistance, comparable to that of copper at cryogenic temperatures. For high current values the multilayer model results have a close agreement with analytical results obtained by the equivalent circuit model in [13], which separates the current flowing between the copper and HTS. It is also noteworthy that at high current regime the single-layer tape has a loss that becomes considerably larger than the multilayered and homogenized models.

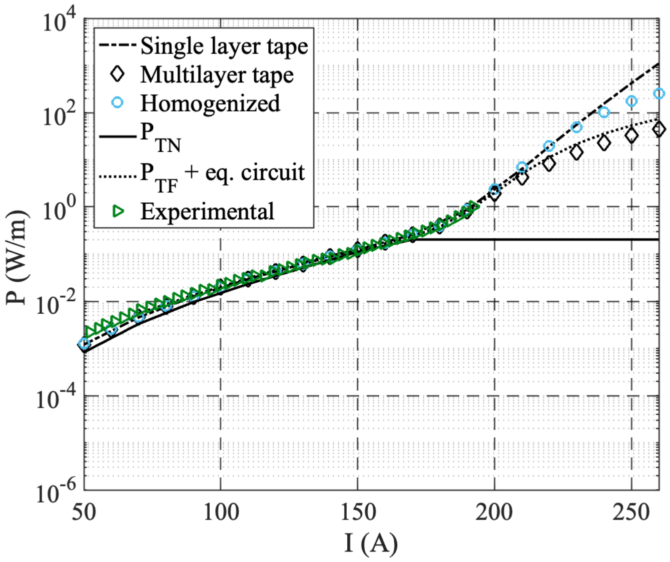

Fig. 3.17 Transport Current losses for a sinusoidal current with *f*=50 Hz.

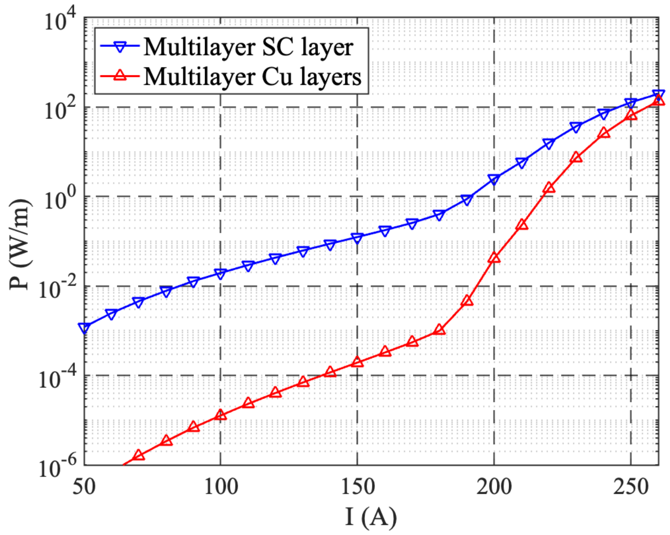

Fig. 3.18 Detail of copper and HTS layer transport current losses for a sinusoidal current with *f*=50 Hz.

Figure 3.18 illustrates the individual contributions of the HTS and copper layers. At a frequency of 50 Hz, copper layer losses are minimal. However, when the critical current of the tape is exceeded, the gap between losses in the copper and superconducting layers narrows. This is due to the increased resistivity of the superconducting layer, resulting from significant transport current and higher self-field, which restricts the critical current. The rise in current and self-field contribute to higher resistivity in the HTS layer, prompting current to also pass through the copper layers. This is demonstrated by the close match between the FEM multilayer model and the analytical model incorporating an electrical circuit ($P_{TF}$ + eq. circuit). Additionally, the graph indicates that under high currents, the single-layer tape has greater losses compared to the multilayer models. This occurs because, for the single-layer tape, FEM loss calculations only consider the superconducting component detailed in (3.35), which follows a power law resistivity function and increases greatly after the critical current is reached. When a copper layer is incorporated in parallel, current preferentially follows the path of least resistivity across different layers. As a result, the analytical circuit result $P_{TF}$ (from (3.37)) closely aligns with the results of the multilayer model, supporting the assumption that at high currents, the copper resistivity must be considered.

### 3.6.3 Magnetization Losses

The multi-layered and single-layer models were subject to an alternating sinusoidal magnetic field (50 Hz) at different selected magnetic flux density amplitude $B_m$ values. In this model, the transport current and the integral of the current in all layers are set to zero. A transverse external magnetic field is applied at the boundaries of the model on the $y$-axis direction (see Fig. 3.12). The numerical results for a single tape subject to a sinusoidal magnetic field perpendicular to the wide surface of the tape (4 mm) are plotted in Fig. 3.19 with homogenized and analytical results. The graph shows good agreement between numerical models and analytical solutions. In this case, the difference between the single-layer and the multilayered superconducting tape models is less noticeable; however, as the magnetic field increases, it is clear that the contribution of the copper layers to the total loss can become equivalent to that of the superconducting layer and therefore must be taken into account when estimating HTS tape losses.

The magnetization loss results for the external alternate field of fixed amplitude and varying frequency are plotted in Fig 3.20 with the multilayer H-formulation results in [150]. For verification purposes, the tape defining constants, $n$, $B_0$, and $I_{c0}$, were set to be the same as the ones found in the reference. The results agree for all applied field frequencies. Hence, the model is validated for applied current, externally applied magnetic field and high-frequency regime.

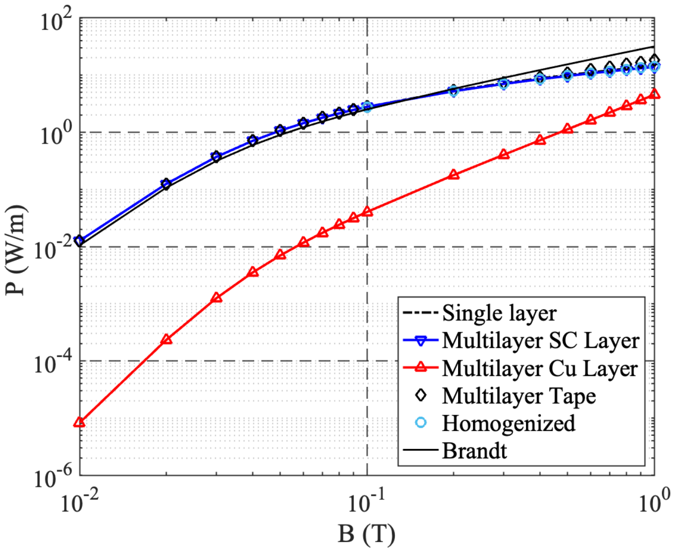

Fig. 3.19 Magnetization losses for a sinusoidal external applied field at 50 Hz.

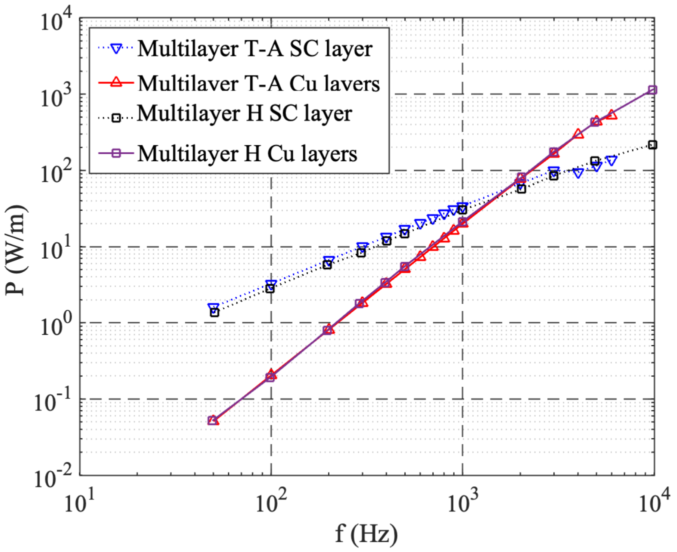

Fig. 3.20 Magnetization losses with a sinusoidal external applied field of 100 mT amplitude with varying frequency 50-10000 Hz.

## 3.7 Summary

This chapter provided an in-depth explanation of the superconducting FEM models used in this thesis; the laws that define the superconductor macroscopic behaviour were stated, and the main equations of the HTS tape model were described.

The geometric and material characteristics of the HTS tape were also given according to measured data. The setup for properly characterizing superconducting tapes in AC and DC conditions is explained in detail, and experimental results are compared to numerical and analytic results.

To better analyze the performance of HTS tapes, a $T-A$ formulation model is proposed to consider the loss influence of the stabilizing layers in 2G HTS tapes, considering their multilayer structure. The model is constructed according to the parallel connection between the HTS and copper layers in the 2G tape. The relevant model boundary conditions and global constraints were defined to describe the electrical connection between the different materials.

Analytical results in the literature to estimate losses in superconducting tapes are outlined. An analytic model to consider the hysteresis and resistive losses in HTS 1G and 2G tapes in an overcritical regime and the influence of stabilizing materials in tape losses is explained, and relevant equations are stated.

Numerical and analytic results for the HTS material in hysteretic and resistive regimes are shown, considering the influence of the copper stabilizing layers as modelled by the proposed multilayer $T-A$ methodology. Experimental and numerical results are compared to those calculated with the analytic model for validation. It is demonstrated through the multilayer model that copper losses can become significant at high currents (DC and AC), high external alternate fields, and high frequencies. This shows the necessity of the multilayer model to accurately estimate tape losses in energy conversion devices, where alternate fields and currents surround materials and consequently affect their performance.

# Chapter 4

# Superconducting Windings for Rotating Electrical Machines

## 4.1 Introduction

This chapter investigates the methodologies and practicability of modelling and potentially applying SCs in rotating electrical machines. The study was performed on an HTS winding inserted into the electrical machine stator. In these conditions, the HTS coils carry AC currents and are subject to AC fields, which can strongly impact the superconductor performance. The superconductors are modelled in the armature windings of a conventional case-study AFPM machine, which, due to its axial geometry, should be simulated in 3D. The developed HTS electromagnetic models use the experimentally described and calibrated superconducting tape models in the previous chapter, and ferromagnetic cores are experimentally calibrated at liquid nitrogen temperatures. The material calibration is inserted in the FEM models, where they are used to describe the windings and rotor and stator core material characteristics. To reduce simulation time and complexity in the models that might be unpractical due to the SC formulations in 3D FEM, a 2D single-slot model is proposed for time-efficient analyses of SCs during the machine operation. This methodology allows efficient analyses of superconductor armature windings to estimate SC performance, reduce losses, and quench risk.

## 4.2 Case-study Axial Flux Permanent Magnet Machine

A conventional copper wounded electric machine design can be achieved through general analytical sizing equations for electrical machines. However, when machine realization is considered, numerical models that can provide further insight into the specifications and performance of the machine can be valuable tools to estimate airgap flux density, efficiency, and losses in the different machine components. These FEM models can also allow machine designers to achieve more reliable and efficient machine topologies, especially when combined with optimization methods based on machine specifications [19].

When electrical machines that utilize superconductors in their circuits are designed, FEM models become an indispensable tool for assessing the feasibility of the machine. The models that require specific numerical formulations to describe the non-linear electromagnetic properties of the materials are essential to investigate the superconductors performance, which is highly sensitive to material critical parameters such as transport current and external magnetic fields magnitude and orientation [163]. This is further exacerbated when superconductors are applied in armature windings, supplied by AC currents and surrounded by alternate external fields since AC working conditions inevitably lead to non-negligible losses in superconductors [66].

These AC losses significantly impact the superconductor performance and must be estimated so that the power required to dissipate the heat generated at a cryogenic level is accurately predicted [63]. The superconducting coils will have lower critical currents and critical magnetic fields. In extreme cases, the losses can overheat the SC with reduced current carrying capacity and cause a quench – i.e. the sudden loss of superconductivity, causing a high increase in the HTS resistivity. Consequentially, the temperature of the conductor can become higher than its critical temperature ($T_c$), and the coils will overheat, with a high risk of irreversible damage to the conductors, which also naturally can cause malfunctioning of the machine [164]. This means that precise estimation of AC losses in SCs is essential for achieving a feasible design that optimizes the superconductors and the overall machine performance.

The HTS coils can be strategically positioned inside slots to help reduce the impact of the external magnetic fields on their performance and minimise effect of the AC fields on superconducting tapes inserted in the windings of electrical machines. Alternatively, ferromagnetic materials can be placed in the vicinity of the superconductors to divert the magnetic field away from the superconducting tapes and conducting elements can be inserted to shield the materials from the surrounding AC fields [165]. Nonetheless, all these methods can contribute to the losses inside the armature slots and reduce linked flux in the armature windings, and thus, their application requires careful consideration [166].

The chosen machine typology to apply the superconducting armature windings in this study is an axial flux machine. This particular machine configuration was chosen because it can be designed with a toroidal stator, which aligns well with the limited bending constraints of superconductors (see Fig. 2.13 [121]). The toroidal stator allows the superconductors to flex over their flat surface while maintaining a large bending diameter, thus preventing any degradation of material properties [87]. Additionally, in radial and axial configurations, this winding arrangement ensures that the armature leakage flux remains mainly parallel to the broad surface of the tape, which is critical to enhancing the performance of the cables [121]. Unlike radial topologies, however, axial flux machines can easily accommodate multistage configurations while preserving compact machine dimensions. This means that the setup can be particularly advantageous for power-dense superconducting machines. For this specific machine, a single-stator with a double-rotor arrangement would allow the efficient exploitation of the magnetic flux from both sides of the armature conductors, as SC coils can produce high magnetic fields due to their ability to carry very large currents. It should also be noted that the presence of an even number of air gaps allows proper balance between the stator and the rotor axial forces, which is one of the drawbacks of single-stage axial flux topologies.

This type of machine is specifically chosen because its geometrical configuration seems to be a more promising solution for easily respecting the strict bending limits of the superconductors and applying multistage configurations [167]. Yet, computational demands of modelling superconductors in 3D geometries are usually required for axial flux machine analyses. Due to the three-dimensional nature of the magnetic field problem [168], the models can take hours, if not days, to simulate and are therefore incompatible with machine design methodologies. Since the design of electrical machines is often an iterative process, the FEM tools to analyse the superconductors inserted in machine windings must be both precise and time-efficient.

The literature reports various formulations to simulate the non-linear behaviour of the superconductor and its dependence on the surrounding magnetic fields [44, 127, 130]. Introducing superconductors with tiny dimensions, non-linear resistivity, and the moving mesh in the rotor make these models highly complex and computationally demanding [45]. Thus, efficient methodologies to reduce this computational cost should be developed.

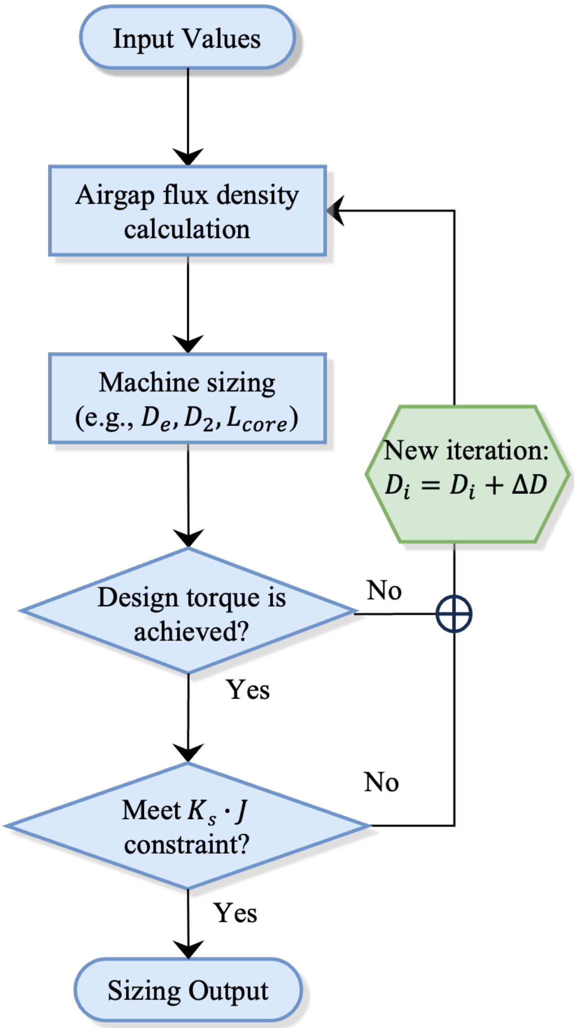

Fig. 4.1 Axial flux permanent magnet single-stage iterative design process.

### 4.2.1 Design Methodology

This chapter examines a case study involving an axial flux machine used to model superconductors within the armature windings, which was designed utilizing traditional sizing equations for AFPM machines [169]. The electrical machine sizing is based on an iterative procedure for designing single-stage surface-mounted AFPM machines [169]. The machine airgap flux density and torque for the minimum permissible machine inner diameter ($D_i$) are calculated using the initial design specifications. Iteratively, the machine diameter is increased, and the geometrical parameters (e.g. outer diameter $D_2$ (lamination diameter), external diameter $D_e$ (including end-windings), core length $L_{core}$) are obtained from the electromagnetic machine sizing equations until the required machine specifications are met, ensuring minimum dimensions for the designed machine. The exit condition of the iterative procedure is the limit product between the linear current density in the stator windings $K_s$ and the current density $J$, imposed by the designer according to the expected cooling method (air-cooled, water-cooled, etc.). The flowchart of the machine design procedure is depicted in Fig. 4.1 [170, 169]. Table 4.1 lists the main data of the machine, while Fig. 2 shows its geometry.

Table 4.1 Main design data of the four pole AFPM

| Parameter | Value |
|---|---|
| Rated torque (Nm) | 95 |
| pole number | 4 |
| Rated speed (rpm) | 1500 |
| Magnet thickness (mm) | 8 |
| Magnet Br (T) | 1.1 |
| Magnet polar pitch (%) | 0.778 |
| Airgap thickness (mm) | 1 |
| Outer diameter (mm) | 340 |
| Inner diameter (mm) | 135 |
| Total axial length (mm) | 390 |
| Total volume (dm$^3$) | 20.34 |

Note that neither the design approach nor the geometry optimization is the focus of this research activity. Hence, the machine must be considered a generic and not optimized design solution sized with the primary purpose of applying the modelling of SC windings integrated with a magnetic circuit. Besides, for the considered speed

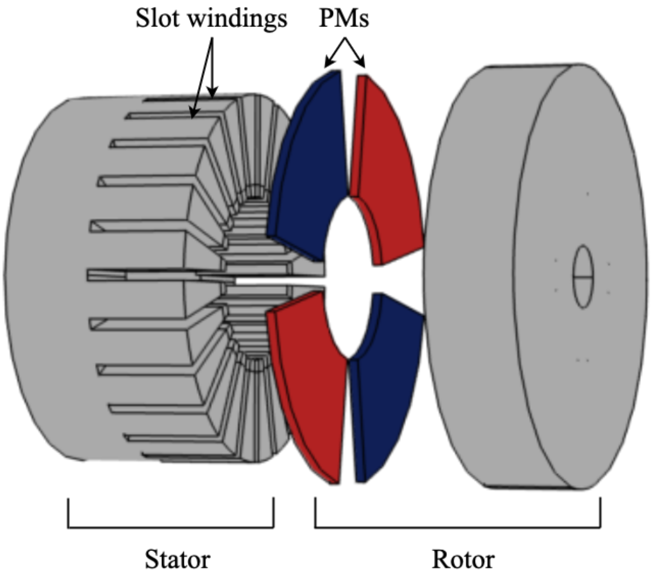

Fig. 4.2 Axial Flux PM machine geometry considered as a case study.

range of 1000-2000 rpm, four poles were chosen to keep a low supply frequency since the thin sheet approximation can be successfully applied for loss estimation for external magnetic field frequencies up to 150 Hz [150].

### 4.2.2 Machine 3D FEM model

The generic non-optimized 4-pole 24-slot AFPM was considered to test the superconducting formulations on a complex FEM model. The machine was first modelled in FEM with the conventional copper armature to have a baseline model for comparison and verification of the working conditions of the machine. The imposed peak slot current is 810 A, given by the machine design tool for the maximum torque condition.

Since the case study AFPM is considered in a single-stage configuration, the chosen winding configuration that allows respecting the conductor bending limitations, as shown in Fig. 4.3, and utilizes a smaller amount of HTS conductor is an integral slot concentrated winding [171]. The selected configuration corresponds to a permissible bending diameter for the ReBCO tapes (11 mm minimum). To guarantee a balanced three-phase system, the winding configuration corresponds to the repetition of the phases AcBaCb. The currents are imposed in the FEM model through their $i_q$ and $i_d$ contributions, using the $d-q$ synchronous referential with the $d-axis$ aligned with the flux of the permanent magnet. To verify the machine model and winding topology, two tests were performed in FEM: 1. The winding phase configuration of the machine was verified by analysing in FEM the back-MMF of the machine, obtained by simulating the machine with no current supplied to the armature windings; 2. With $i_q \neq 0$ and $i_d = 0$, the specified torque and airgap flux density were verified.

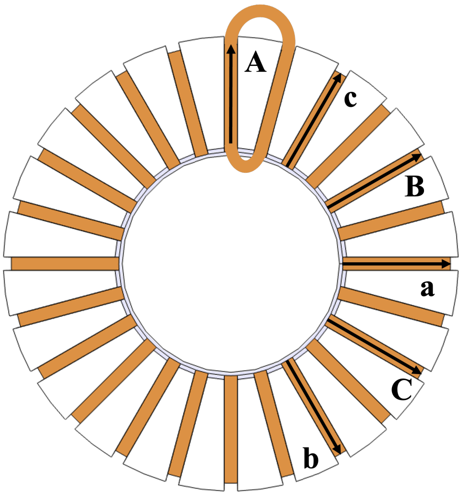

Fig. 4.3 Winding configuration for the considered axial flux PM machine.

### 4.2.3 Ferromagnetic Material Characterization

Except for HTS machines with the cryostat limited to the superconducting elements, superconducting electrical machines might have rotor or stator cores operating entirely at cryogenic temperatures. In this initial analysis stage, the stator of the AFPM machine is considered to operate fully in cryogenic conditions, i.e., immersed in $LN_2$ bath. In this situation, to accurately describe and model the ferromagnetic materials used for the machine cores, it is required to introduce in FEM their non-linear BH curve and specific losses for machine performance estimation. Since the datasheets of ferromagnetic materials usually report the BH curves only at ambient temperature, experiments are performed to characterise cores at cryogenic temperatures. A toroidal sample of 0.35 mm Vacoflux 50 cobalt-iron (CoFe) laminations and a toroidal sample of 0.5 mm M470-50A silicon-iron (SiFe) laminations were tested and characterized at ambient and cryogenic temperatures through the procedure described in [48]. The toroidal samples were wound with a primary magnetizing winding supplied by a sinusoidal power source. The iron characteristics of the samples were measured under sinusoidal flux excitation through the secondary (sensing) winding. Using a high-accuracy digital power meter, the primary current and the secondary induced voltage were measured with the core at ambient (298 K) and cryogenic temperatures (77 K). In detail, for the cryogenic test, the cores were positioned in an Expanded Polystyrene (EPS) foam container and submerged in a liquid nitrogen bath. In Fig. 4.4, the circuit characterizing the ferromagnetic samples is depicted. Note that although a radial flux machine sample core was tested, the experiment was performed to verify the material characteristics. Hence, its geometry and application are not important in this context.

The primary winding was excited by a perfectly sinusoidal supply at different frequencies, and the primary current and induced voltage in the secondary winding were measured to analyze the BH curves in the flux density range of 0-1.6 T, with

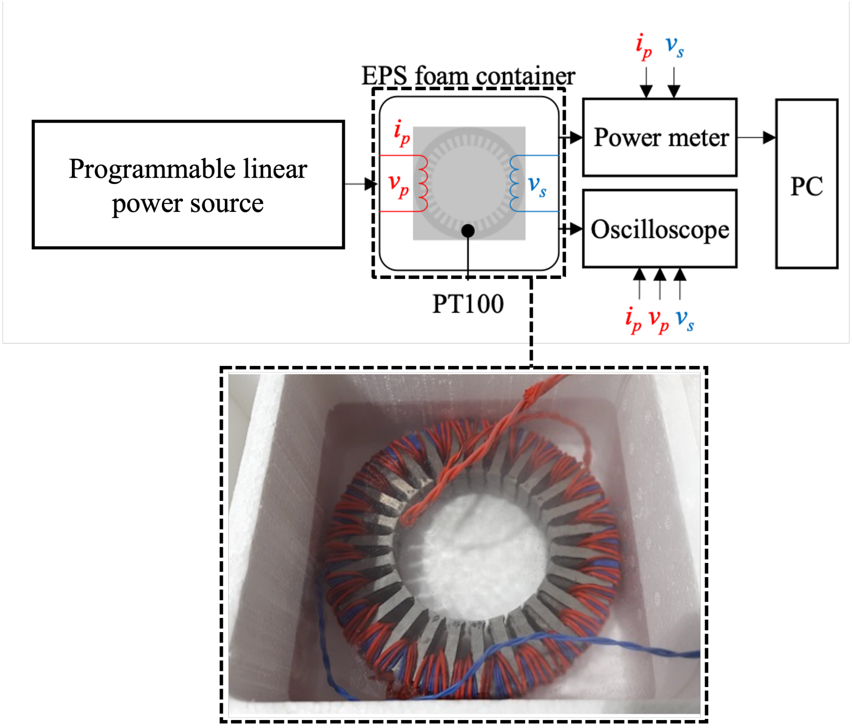

Fig. 4.4 Circuit for magnetic characterization of cores at cryogenic temperatures with detail of iron sample immersed in LN2 at 77 K.

frequencies ranging from 20 - 100 Hz. During the tests, the secondary voltage form factor was verified to be 1.11±1, per the standards [172].

The peak magnetic flux density $B_m$ and the peak magnetic field $H_m$ in the iron sample were determined to obtain the BH curve. Under sinusoidal excitation and in the absence of minor hysteresis loops, the values for $B_m$ are calculated by (4.1) [173].

$$B_m = \frac{|\overline{V_s}|}{4 f N_s A} \tag{4.1}$$

In 4.1, $|\overline{V_s}|$ is the mean rectified value of the secondary induced emf; $f$ is the excitation frequency; $N_s$ is the number of turns of the secondary winding; $A$ is the cross-sectional area of the core sample. The peak magnetic field $H_m$ is stated in (4.2).

$$H_m = \frac{N_p I_m}{l_{av}} \tag{4.2}$$

In 4.2, $I_m$ is the peak value of the primary current, $N_p$ is the number of turns of the primary winding, and $l_{av}$ is the mean length of the magnetic path in the core given by (4.3).

$$l_{av} = \frac{\pi(D_o - D_i)}{ln(D_o/D_i)} \tag{4.3}$$

In (4.3), $D_o$ and $D_i$ are the outer and inner diameters of the yoke of the toroidal core sample [174]. The measured BH curves are plotted in Fig. 4.5. The cryogenic temperature marginally impacts the BH magnetizing curve for the two investigated materials. The core losses are also measured for both samples to ensure the completeness of the information. The primary current $i_p$ and the secondary induced emf $v_s$ are measured to calculate the active power $P$ (W), the specific core losses $p_{Fe}$ (W/kg) are computed according to (4.4) [173].

$$p_{Fe} = \frac{N_p}{N_s m_a} \cdot P = \frac{1}{m_a} \frac{N_p}{N_s} \frac{1}{T} \int_0^T v_s(t) i_p(t) dt \tag{4.4}$$

In (4.4) $T$ is the electrical period of the supply voltage and current. The factor $N_p/N_s$ is the turn ratio of the primary and secondary windings, and $m_a$ (kg) is the mass of the sample. Fig. 4.6 shows the specific core losses measured at 50Hz on the two core samples.

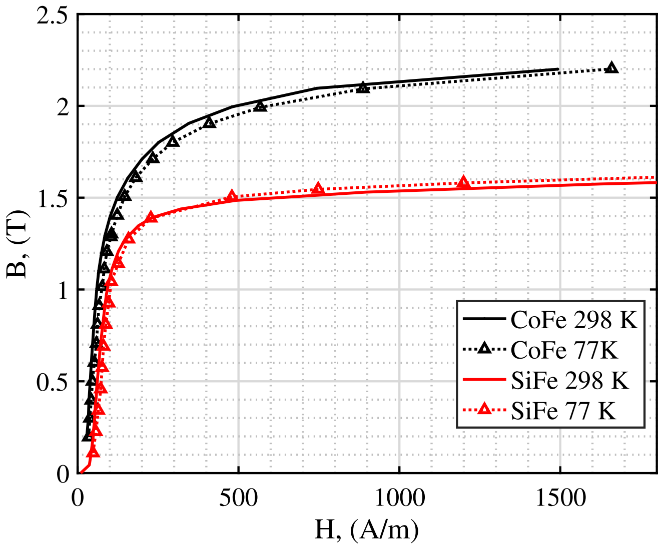

Fig. 4.5 BH curve at 50 Hz for the M470-50A and Vacoflux 50 toroidal samples at ambient and cryogenic temperatures.

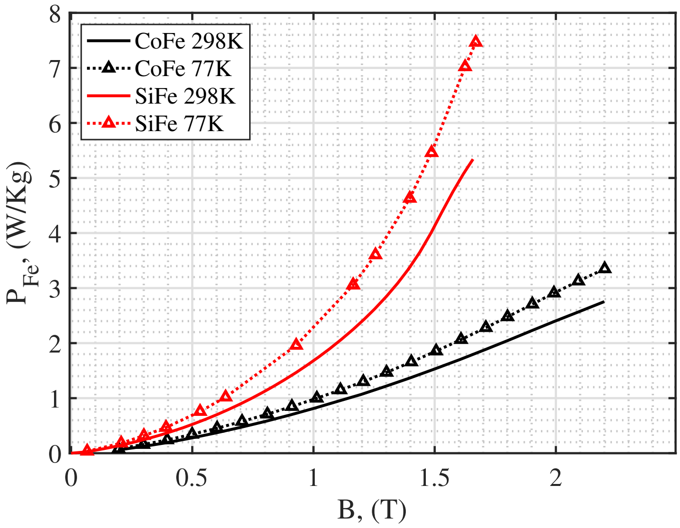

Fig. 4.6 specific losses at 50 Hz for the M470-50A and Vacoflux 50 toroidal samples at ambient and cryogenic temperatures.

As shown in Fig. 4.5, the impact of cryogenic temperatures in the iron BH curve is minimal. However, the losses significantly increase due to the low-temperature operation, which increases the conductivity in the iron components. The most significant difference is in SiFe samples, which have a maximum increase of 37%, while the CoFe sample has a 20% maximum loss increase. The measured BH curve is applied in FEM models in the material characteristics to describe the ferromagnetic core components of the motor. Generally, losses can either be inserted as a function of the magnetic field $P_{Fe}(B)$ or they can be fitted to a program-integrated loss function. This includes typically adding the Steinmetz or Bertotti coefficients in the material loss calculation module [175]. The loss function given by the Steinmetz equation is stated in (4.5) [174].

$$P_S = k_S f^{\beta} B_m^{\gamma} \tag{4.5}$$

In (4.5) $K_S$, $\beta$ and $\gamma$ are the standard Steinmetz model coefficients obtained by fitting the loss model to measured data. The Bertotti loss function is stated in (4.6) [176, 177].

$$P_B = k_h f B^{\alpha} + k_{cl} f^2 B_m^2 + k_{exc} f^{3/2} B_m^{3/2} \tag{4.6}$$

In (4.6) $k_h$ and $\alpha$ are the coefficients of the hysteresis losses, $k_{cl}$ is the coefficient of the classical losses, and $k_{exc}$ is the coefficient of the excess losses. For the case-study machine model, the coefficient-based loss functions were not used. Instead, the measured data of the material loss density at 50 Hz is directly inserted in the model as a lookup table and used as a loss function $P_{Fe}(B, f)\mathrm{W/m^3}$.

### 4.2.4 Results for the 3D FEM Models

To accurately represent and analyze the magnetic field surrounding the superconducting tapes and limit the simulation time, copper surfaces replaced the armature windings in all slots except for one where the superconducting surfaces were applied to estimate SC losses. This method is supposed to emulate the working conditions of the machine when the slots are filled with superconducting tapes (with thickness in the order of $\mu$m) and allows applying the thin sheet approximation to simulate superconductors inside the machine slot. The machine stator is depicted in Fig. 4.7.

Note that it is expected, due to the geometric symmetry of the machine, that all slots will be subject to the same magnetic field evolution after one complete rotation of the rotor magnets. The direct consequence is that all slots must have approximately the same losses. This way, the superconductor losses can be estimated in only one slot, making the model significantly more straightforward to implement and less time-consuming. To further reduce the model complexity in these simulations, the end-windings of the armature coils are not modelled, and the current is imposed in

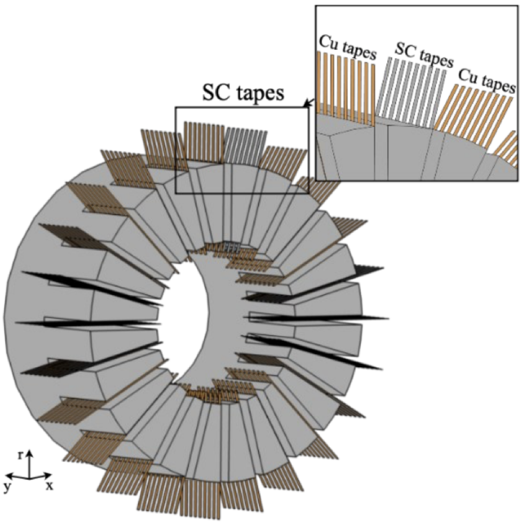

Fig. 4.7 Machine stator with superconducting tapes in one slot (grey) and copper tapes in the remaining slots (copper).

each conducting element through boundary conditions. The developed 3D AFPM model with superconducting tapes in one slot only is solved in tens of hours using a standard desktop computer with 32GB of RAM. It is important to notice that a model with only copper conductors would be considerably less time-consuming, and could be performed in a few hours.

The rated slot current of 810 A was imposed in nine tapes per slot for the armature coils of the AFPM machine. In this way, the transport current in each SC results well below the critical current of the considered REBCO tape (i.e., 90 A per conductor, which is approximately 55% of the critical current). The same number of tapes per slot has also been considered for the copper conductors for modelling simplification. This would be impracticable for a prototype because the copper windings have much lower current density capability than SCs.

Figure 4.8 shows the air gap magnetic induction and the electromagnetic torque for the 3D FEM model of the copper wounded AFPM (Cu-AFPM) and for the same model with SCs in one slot (SC-AFPM) as illustrated in Fig. 4.7. To accurately describe the material characteristics in FEM and compute the material losses, the models take into account the measured SiFe magnetizing curve for the stator and rotor core materials and the experimentally calibrated SC single-layer tape model validated in Chapter 3.

As shown in Fig. 4.8, the models have similar airgap induction and torque results since the same slot current is imposed in both machines. The slight difference between both results is due only to the finer mesh that must be used when superconducting formulations are added to the FEM models. The torque result is shown for both machines starting at t = 0.02s since the transient regime is not used for the machine analyses. When the superconducting formulations are applied in the complete machine model, a step function is added to the remanent field in the permanent magnets and to the imposed stator current. This function, which starts at 0 and has a maximum value of 1, guarantees that the field surrounding the superconductors

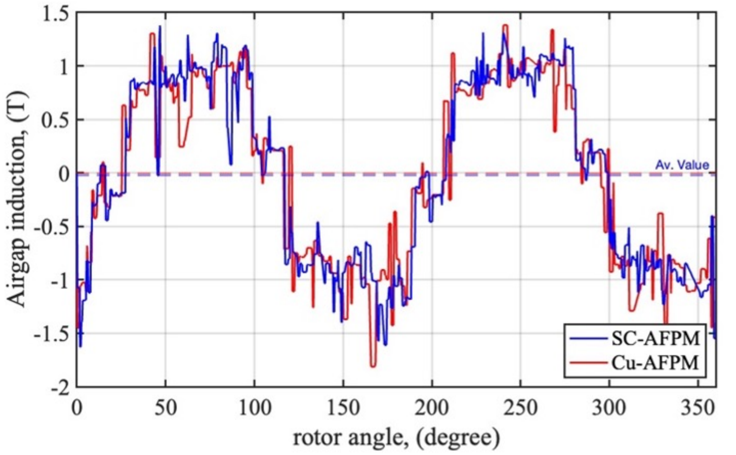

(a)

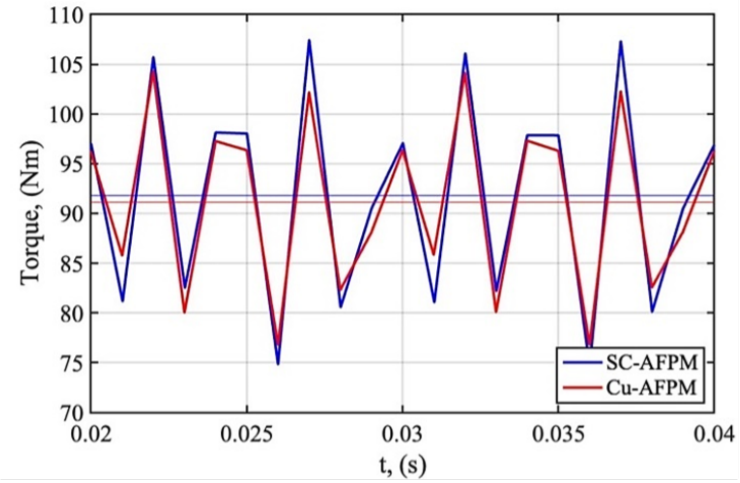

(b)

Fig. 4.8 Air gap magnetic induction (a) and electromagnetic torque (b) for the Cu-AFPM and the SC-AFPM models.

begins at zero and increases through a smooth function, thus significantly improving the $T-A$ formulation convergence.

Simulations demonstrate that the copper wounded AFPM model and the SC-AFPM model provide the same results regarding the air gap magnetic induction and electromagnetic torque. However, the power losses at the copper or superconducting windings differ significantly, as shown in this chapter. Nonetheless, the obtained results prove the appropriateness of the proposed modelling approach to analyse the behaviour of electrical machines equipped with SCs.

## 4.3 2D Slot Model for AC Loss Estimation

Since each 3D simulation of the motor study has a computation time of about 54 h, it would be inefficient to model the superconductors inside the electrical machine to optimize the machine topology and devise methods to mitigate the effects of the applied magnetic field on the SC tapes, such as shields, flux diverters, and different tape positioning inside the armature slot. The magnetic field within the slot of a permanent magnet electrical machine arises from two primary sources: the self-field in the conductors and the magnetic field produced by the permanent magnets. In the context of the specific axial flux permanent magnet (AFPM) machine under consideration, the contribution of the permanent magnets to the magnetic field is particularly significant due to the narrow slot design intended to accommodate very small superconductors.

A 2D slot model for expedited analysis of the superconductors inserted in the armature slots is proposed in this thesis to address these concerns [49]. Since the purpose of the model is to separate the machine 3D simulation from the superconducting formulation so that the computation time can be reduced, the AFPM is first simulated, considering it is a conventional copper wounded machine. The machine slots are substituted by standard copper conducting surfaces to analyze the field distribution inside the slot and in the vicinity of the HTS tapes as if superconducting tapes are inserted in the slots. The magnetic field density norm $|\mathbf{B}|$ surrounding the armature coils analyzed in FEM is shown in Fig. 4.9.

Analyses on the magnitude of the magnetic field within the slot $B(x,y,z)$ revealed limited variations in $B_z$ at any $z-$axis coordinate within the region enclosed by the

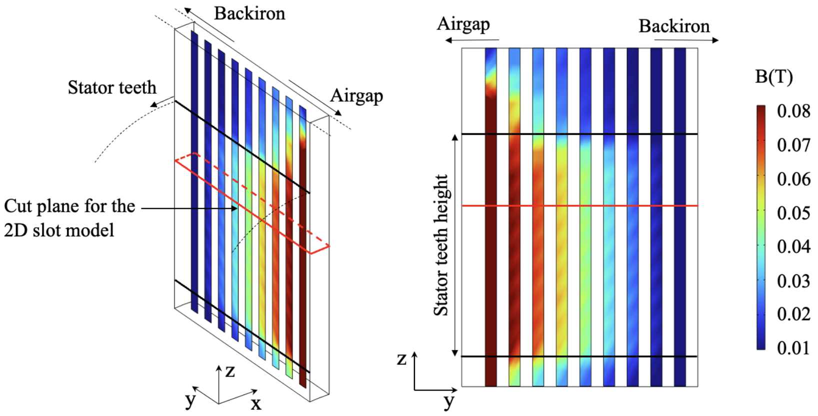

Fig. 4.9 Magnetic flux density on the surface of the armature conductors with a cut plane for the 2D slot model.

stator teeth. Consequently, a cut plane at the midpoint of the slot height was selected to analyse the boundary magnetic field strength. This cut plane is delineated by a rectangular shape with red borders in Fig. 4.9.

### 4.3.1 Boundary Conditions

The equivalent 2D slot model is constructed from the analysed cut plane in the 3D geometry. In the 2D FEM model of the armature slot, the rotating magnetic field from the permanent magnets is enforced through boundary conditions derived from a 3D model. The initial simulation of the 3D machine model, conducted with no stator current, aimed to analyze only the rotating field generated by the permanent magnets; hence, for the construction of the 2D model, no current is imposed in the armature conductors.

At a specific time instant when the considered slot is exposed to the maximum flux produced by the permanent magnets, Fig 4.10a demonstrates that the $B_x$ component varies linearly along the slot depth ($y-$axis) on the red border of the identified cut plane (in Fig. 4.9). The maximum magnitude of $B_x$ is observed at the air gap border, while the lowest is at the back iron border. Consequently, $B_x$ is incorporated in the 2D model using a linear interpolated relation between the values at each border. The $B_y$ component exhibited minimal variation along the $y-$axis, and as a result, it was treated as a constant value along the slot depth. The $B_x$ and $B_y$ components were implemented as boundary conditions through a function of the magnetic field over time, $B(t) = B_{x,y} sin(\omega t + \theta)$, where $\theta$ represents the phase difference between the slot current and the rotating field, to account for the time-dependent nature of the rotating field of the machine in the 2D model.

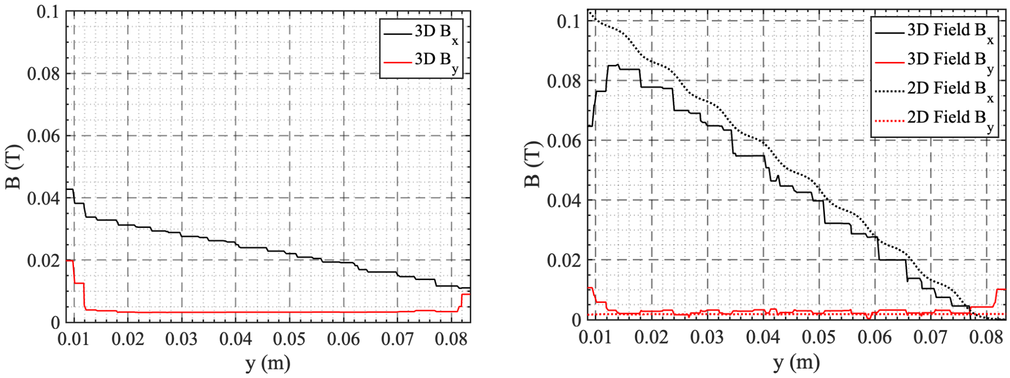

(a) (b)

Fig. 4.10 The flux density components along the $x$ and $y$ directions, determined using 3D FEM without current in the armature conductors (a) and with current by both 3D and 2D FEM (b). The field is assessed in the $y-$axis direction along the border of the cut plane.

Considering how the problem is specified, starting from inputting the rotating field of the machine on the boundaries and adding currents to the SC tapes, the model is not solvable with only magnetic field boundary conditions, as this would not allow the field from the tape current to change the field at the armature slot boundaries. A magnetic vector potential boundary condition defines a source for the magnetic field instead of fixing the magnetic field to a limited value. In this way, two types of boundary conditions are used on the 2D model, as depicted in Fig. 4.11, one that imposes the magnetic field and a second to define the magnetic vector potential. These are stated in 4.7.

$$\mathbf{n} \times \mathbf{H} = \mathbf{n} \times \mathbf{H_0} \qquad \mathbf{n} \times \mathbf{A} = \mathbf{n} \times \mathbf{A_0} \tag{4.7}$$

In (4.7), the parameter $H_0$ specifies the tangential value for the magnetic field, and $A_0$ defines the magnetic vector potential normal to the boundary, $\mathbf{A}$=A $e_z$. Note also that defining $A_z$ has the same effect as defining the component of $\mathbf{B}$ normal to the slot border, $B_y$. When the superconductors experience the maximum current and the slot is simultaneously impacted by the maximum permanent magnetic flux (the most challenging operational condition for the superconductors), Fig. 4.10b illustrates the

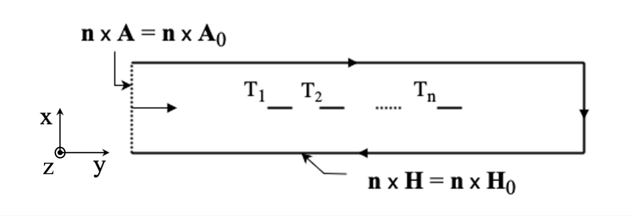

Fig. 4.11 Electromagnetic model boundary condition definitions on the 2D slot model

$B_x$ and $B_y$ for the 2D simulation. It should be noted that the proposed single-slot 2D modelling approach reduces the simulation computational time significantly (from tens of hours to a few minutes). Consequently, in the 2D model, a much finer mesh can be imposed compared to the 3D model. For this reason, the results in Fig. 4.10b vary more smoothly for the 2D model than those for the 3D. In Fig. 4.12, the time evolution for the magnetic flux density components at a slot depth of y=0.02 m is shown. A good match between the 3D and 2D waveforms is obtained, albeit with a slight phase shift.

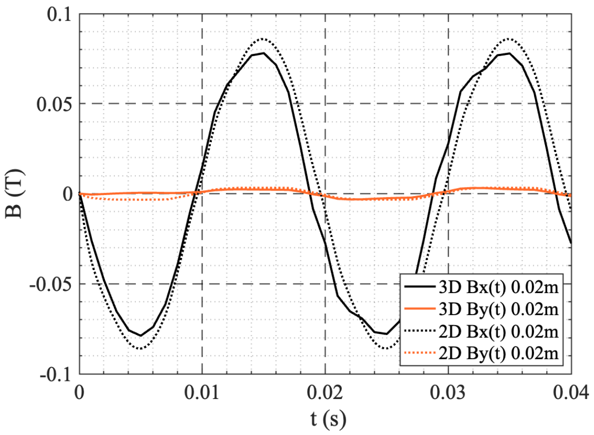

Fig. 4.12 Magnetic flux density time evolution at y= 0.02 m during two 3D and 2D simulation cycles

### 4.3.2 Slot Model Numerical Results

The magnetic field strength perpendicular to the tape is reported to have the most significant impact on increasing losses, while a magnetic field parallel to the tape has the most negligible influence [178]. Although this is generally true for SC tapes, the

FEM model with the thin sheet approximation only takes into account the magnitude of $B_x$ (normal to the tape) instead of different weights for perpendicular and parallel components to the tape's widest surface. The induced currents will be maximum when the magnetic field is perpendicular to the flat surface of the tape. As depicted in Fig. 4.13, the field contribution inside the slot is mainly in the $x-$axis direction. Therefore, a 90° rotation for the tapes is suggested here to decrease the field impact on the superconducting tape losses, as shown in Fig. 4.13b. This will allow a closer examination of the effect of tape orientation on their losses. The analyses of the magnetic field in the 3D motor simulation with 90° rotated tapes allowed to verify that the field at the slot boundaries is the same as for the previous tapes' orientation.

The losses estimated in the SCs by the 3D FEM model with SCs in one slot and by the single-slot 2D FEM model with the SC tape oriented as in Fig. 4.13a and oriented as in Fig. 4.13b (i.e., with 90° rotated tapes) are reported in Figure 4.14. It should be noted that the numerical results for the 3D FEM model are shown only for the machine-rated operation point due to the substantial computational time required by the 3D simulation to compute the SC losses (54 h per simulation). The results

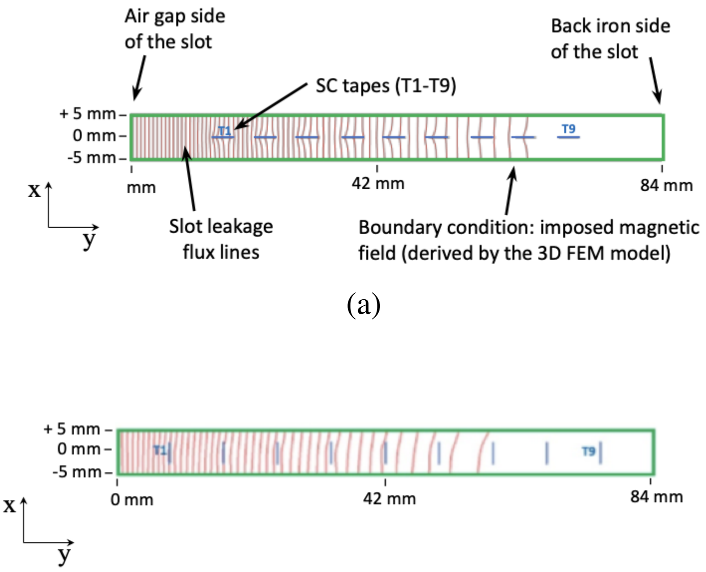

(a)

(b)

Fig. 4.13 Magnetic flux density on the surfaces of the SC tapes T1-T9 obtained with the 2D single-slot model for HTS tapes oriented perpendicular (a) and parallel (b) to the slot leakage flux.

show that the single-slot 2D FEM model aligns well with the 3D results, validating the proposed modelling approach. It should be observed that Fig. 4.14a shows a limit condition where the SC tapes are oriented parallelly to the slot $y-$axis and perpendicular to the magnetic flux leakage. In these conditions, the tapes are subject to high alternate magnetic field amplitudes and carry high transport currents, and consequently, they quench, i.e., have increased resistivity and losses. Comparatively, if copper conductors have the same imposed current, the loss on each conductor can be estimated by (4.8), and the total losses amount to about 15 W.

$$P = I_{slot}^2 \rho_{Cu} \frac{k_f * A_{slot}}{l_{Cu}} \tag{4.8}$$

In (4.8), $k_f$ and $A_{slot}$ are the slot filling factor and cross-sectional area, respectively, and $l_{Cu}$ is the copper conductor length which includes its end-winding length. This proximity between the losses of superconducting and copper armature conductors demonstrates that using the SC tapes (which can cause high cooling requirements) and neglecting the effects of the direct perpendicular magnetic does not provide a real benefit to a conventional copper winding machine at cryogenic temperatures. Nevertheless, the FEM simulations showed that the perpendicular positioning of the superconducting tapes, as shown in Fig. 4.14b, reduces the risk of quenching since it allows maintaining the wide surface of the conductor parallel to the leakage magnetic field, providing minimal losses per unit length. This finding agrees with the conclusion provided in [178]. Incidentally, the orientation of the conductors in the slot enables the realization of toroidal winding solutions, allowing better compliance with the minimum bending radii of commercial superconducting tapes and can be applied to multistage AFPM machines.

### 4.3.3 Summary

A 2D slot model was proposed to easily separate the superconducting formulations from rotating electrical machine FEM models. The model is applied to a case study AFPM motor model, providing agreeable results for a significantly reduced simulation complexity and duration (running in a few minutes). The model results reasonably agree with those found by the study of the machine with superconducting formulations in the 3D electrical machine study, showing the feasibility of HTS loss estimation with the proposed approach.

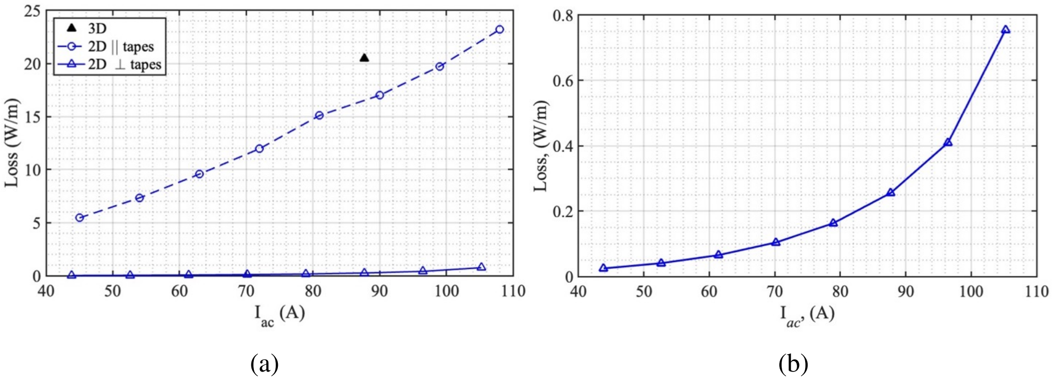

(a) (b)

Fig. 4.14 Losses on the SCs by the 3D FEM and by the 2D single-slot model for two different tape orientations (a), and zoom for the 2D ⊥ tapes (b).

The proposed slot model requires careful examination of the magnetic field surrounding the slot conductors. To develop this model, the applied magnetic flux density at the slot borders is defined by a sinusoidal time function, which means that only the first time harmonic of the magnetic field was considered, contributing to keep the FEM model as simple as possible. Since the conductors inside the machine armature slots will be subject to different harmonic contributions, specific machine topologies might require better representation with the remaining time harmonics for accurate loss estimation. Furthermore, although magnetic field and magnetic vector potential boundary conditions were chosen to represent the rotating magnetic field from the permanent magnets, the slot model methodology and the separation between the AFPM motor and the superconducting armature coils could also be applied through magnetic field boundary conditions, as long as both the initial machine simulation to determine the model magnetic field and the slot model simulation were performed with current in the armature conductors.

The presented methodology can be a tool for machine designers to estimate better the best placement for superconducting materials inside machine armature slots and find ways to mitigate these losses or reduce the impact of alternate magnetic fields and currents on the performance of the HTS conductors.

# Chapter 5

# Extended Slot Model

## 5.1 Introduction

This Chapter proposes an extended 2D single slot model that, similarly to the model presented in the previous Chapter, is constructed by obtaining the magnetic field amplitudes from 3D electrical machine simulations inside the armature slot [49]. The proposed extended single-slot model, however, is constructed to represent all harmonics of the slot field. In the 3D motor simulation, the magnetic field complete temporal and spatial evolution is acquired and introduced in the 2D model to define the magnetic field boundary conditions. The model proposed in Chapter 4 considers a linear spatial variation of the magnetic field amplitude along the slot depth, and only the first time-harmonic of the magnetic field is accounted for. The extended slot model, instead, is constructed to include all time and space harmonics of the electrical machine rotating field.

The modelling methodology in this Chapter is based on determining the magnetic field spatial and temporal distribution at each mesh point of the slot boundaries in the 3D electrical machine simulation and implementing it in the 2D model boundaries. This approach guarantees the replication of the magnetic field surrounding the machine armature windings at each simulated step and slot coordinates.

Similarly to the equivalent 2D model developed in Chapter 4 and published in [49], the tangential magnetic field component is imposed in the 2D model boundaries. The superconductor winding performance is estimated through the finite element model using the thin-sheet approximation with the $T-A$ formulation in the HTS domains.

## 5.2 Toroidal AFPM

The results of the analysis performed on the SC tapes in Chapter 4 indicate that to prevent HTS performance degradation, the (4 mm) surface of the tape should not be facing the perpendicular magnetic field, which is also in line with literature reports [67]. In this study, to evaluate the applicability and accuracy of the developed 2D and 3d slot models, the chosen case study, AFPM machine topology, features a toroidal winding. The reason for implementing this winding configuration is twofold: it easily allows for respecting the material's minimum bending radius and keeping the HTS tapes parallel to the magnetic flux leakage inside the armature slots. Both conditions are critical to keeping high critical current and low AC losses in the HTS conductors.

The toroidal configuration allows keeping a high transport current in the armature windings as the effects of perpendicular AC fields on the HTS conductors are reduced. Hence, a multistage axial flux machine is chosen to take advantage of the axial configuration and better exploit the stator flux. The considered machine is a 10-pole, 12-slot axial flux permanent magnet motor with toroidal core wound coils, designed using conventional sizing equations for copper-wound AFPMs [169, 51]. The total slot current of 910 A is imposed in the $q$-axis to reach maximum torque, and the chosen winding configuration corresponds to the repetition of phases AaCcBb.

Since this study aims to verify the application of the slot model for SC AC loss estimation, this machine is not optimized. Table 5.1 lists the primary data of the machine, and Fig. 5.1a depicts its geometry. Fig. 5.1b shows a detailed representation of the stator windings.

Note that for this design, it will be necessary to introduce the superconductors into the slot. Hence, a width of 8 mm was considered for the slot opening to accommodate the REBCO tapes, whose widths do not surpass 4 mm. When placed in the stator, the superconducting tape bending diameter is 60 mm, well below the limit of 11 mm for the selected tapes [73].

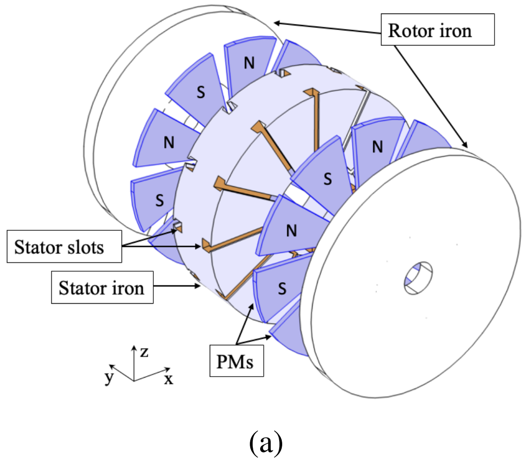

(a)

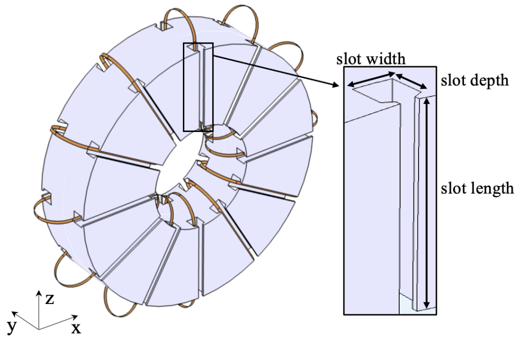

(b)

Fig. 5.1 10-pole 12-slot toroidal AFPM machine geometry, (a) exploded view: stator iron (grey), PMs (blue) and rotor iron (white), (b) representation of the AFPM stator with toroidal core wound coils.

Table 5.1 Machine main design parameters

| Parameters | Values |
|---|---|
| Rated power (kW) | 20 |
| Rated speed (rpm) | 1200 |
| Magnet thickness (mm) | 8 |
| Magnet polar pitch (%) | 0.778 |
| Airgap thickness (mm) | 1 |
| Outer diameter (mm) | 375 |
| Inner diameter (mm) | 150 |
| Total axial length (mm) | 164 |
| Total volume, ($dm^3$) | 14.45 |

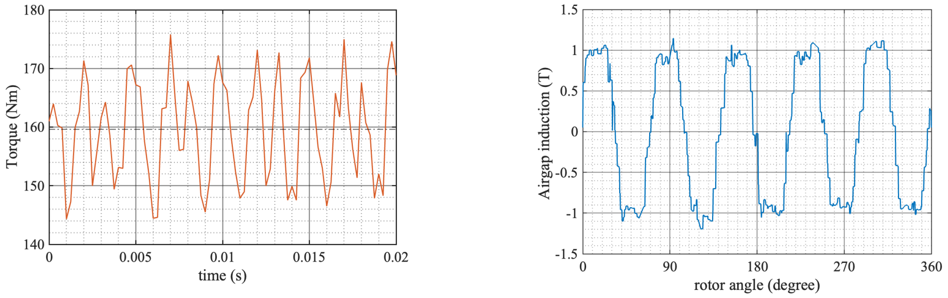

(a) (b)

Fig. 5.2 10-pole 12-slot multistage toroidal AFPM torque (a) and airgap induction in load condition (b).

To avoid the excessive computational complexity of introducing superconductors in the machine 3D finite element simulation, the armature conductors are just standard conducting tape-like surfaces with imposed slot current, where losses are initially neglected. The armature conductors of the AFPM machine are shown in Fig. 5.3. The conductors collectively carry the total slot current of 910 A. In this way, it is expected that the magnetic field is represented as if superconducting tapes are inserted in the armature windings. Note that nine conducting elements were chosen so that when superconducting tapes are considered, the total slot current can be imposed in the HTS conductors without reaching the critical current of the material (160 A). Figs 5.2a and 5.2b show the torque and airgap flux density results for the 3D AFPM model with surface conductors in the armature. The results obtained for the machine torque and airgap induction prove the appropriateness of the proposed

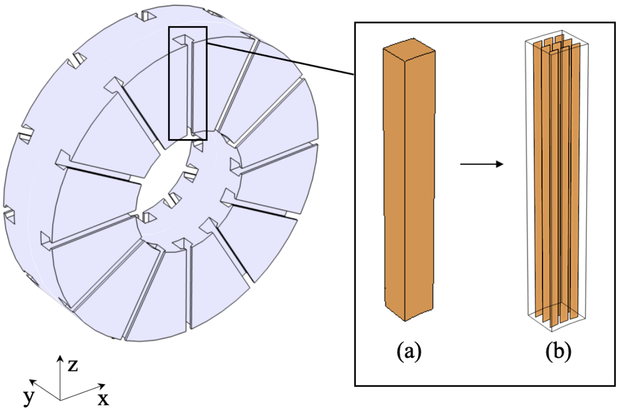

Fig. 5.3 FEM model of stator iron with detail of armature slot with (a) standard copper windings and (b) conducting surface elements with applied rated slot current, 910 A.

modelling approach to evaluate the electrical machine behaviour. Note that in this FEM model, the slot current is applied in the conductors. Thus, the main difference between the superconducting and the simulated ideal conductor machine will be the conductor losses and the resulting phase voltage; therefore, it does not affect the results in Fig. 5.2.

## 5.3 Extended 2D Slot Model

The magnetic field of the 2D slot model is derived from the 3D simulation results of the AFPM motor. These results were published in [51]. While the initial AFPM motor study does not incorporate the superconducting characteristics directly in the 3D model, the surface representation of the armature conductors ensures the magnetic field distribution inside the slot matches that of superconducting tapes carrying the slot current.

The SC performance is evaluated in only one armature slot since the geometric symmetry of the machine allows for the assumption that each slot will be subject to similar magnetic field evolution after one rotation of the rotor magnets. Additionally, the magnetic flux distribution is not significantly altered along the slot length. Therefore, the 3D slot can be modelled by only a 2D cross-section (see Fig. 5.1), which further simplifies the problem and reduces simulation time consumption [49]. The slot cross-section where the field is determined is illustrated in Fig. 5.4.

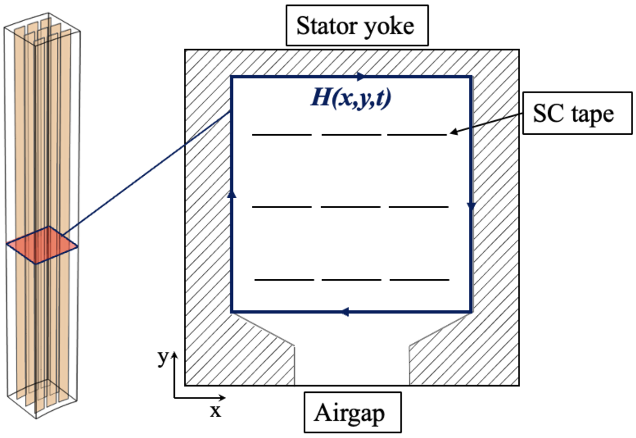

Fig. 5.4 Stator slot cross-section in 3D, analyzed plane highlighted in red, boundaries to acquire the magnetic field delimited in blue.

From the 3D FEM machine simulation, where a standard machine with armature surface conductors is modelled for one electrical period, the component of the field $H_t(x,y)$ tangential to the slot cross section boundaries is evaluated at each mesh node in the slot's cross-section limits (represented in blue in Fig. 5.4). The result of this evaluation for the motor study is a matrix giving the field at each position for every time step of the simulation $H_t(x,y,t)$. This field is acquired for each line delimiting the cross section (represented in red in Fig. 5.4). These results are exported from the 3D model introduced in the 2D model.

The acquired field is then introduced in the 2D slot model at each edge element of the cross section through tangential magnetic field boundary conditions, taking the information of the files containing $H_t(x,y,t)$ derived in the 3D model. The $T-A$ formulation is applied in the armature conductors defined in the 2D model with the same imposed slot current of 910 a and with the superconductor material characteristics in Table 3.1. Note that limiting the tangential component of the field along the slot borders limits the total current inside the slot. This is feasible because the magnetic field on the complete 3D machine and 2D slot model is the same, and the imposed current in each tape is equal, ensuring Ampère's law is respected. The full methodology of the extended slot model is shown in Fig. 5.5.

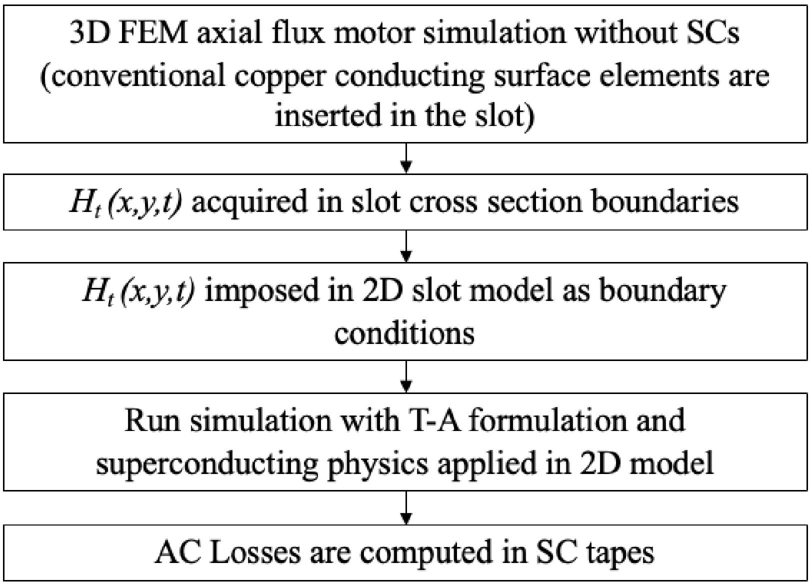

Fig. 5.5 Flowchart of methodology to apply the 3D slot model.

In Fig. 5.6a, the cross-section of the analyzed stator slot in the 3D simulation (with conducting surface elements) is shown. The 2D slot model results (with superconducting tapes) are reported in Fig. 5.6b. The flux density norm, $|\mathbf{B}|$, colour map and the flux density arrow surface, $B_x$ and $B_y$, are plotted for the same simulation times. The arrow surface plot shows that most of the magnetic flux density is parallel to the HTS elements due to using toroidal core wound coils, which will have a significant effect in reducing the magnetic field impact on the superconductor losses [178]. By comparing the cross section from the 3D motor simulation (Fig. 5.6a) with the 2D model results (Fig 5.6b), it is verified that this method provides an accurate description of the flux density in the slot plane that surrounds the superconductors and shows the appropriateness of considering toroidal wound coils for the designed machine.

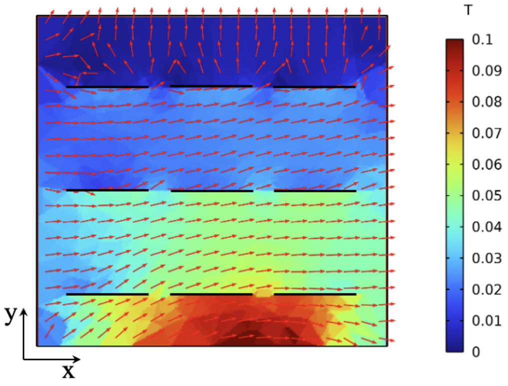

(a)

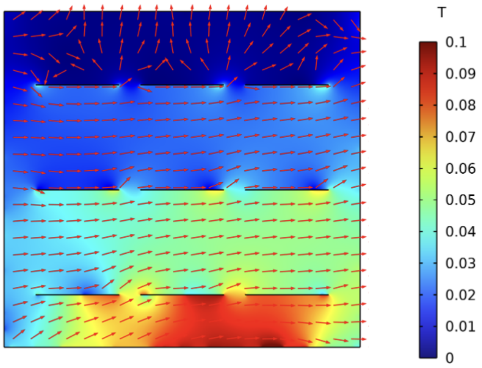

(b)

Fig. 5.6 Magnetic flux density Surface plot $|B|$ (T) and $B_x$, and $B_y$ arrow surface plot, (a) in a cross-section of the 3D machine slot, (b) in the 2D slot model.

### 5.3.1 Validation with Analytical Methods

Two specific cases were analyzed to verify the model's applicability for loss estimation by comparing simulation and analytical AC loss results for the superconducting tapes.

In the first case analyzed, the 3D AFPM model is run with null current in the armature conducting elements and remanent flux density of $B_r$ = 1.1 T is set in the permanent magnets. In this situation, when no current is imposed and the HTS tapes are exposed only to external varying fields, they exhibit magnetization losses. To determine this loss contribution analytically, the magnetic field amplitude, oriented perpendicularly to the flat surface of each conducting tape (in the $y$ direction, as shown in Fig. 5.6), is evaluated in the 3D model. Since the magnetic flux density amplitude on the surface of the tapes is almost sinusoidal in time, this allows for the calculation of the analytical losses $P_B$ (W/m) using Brandt's equation for magnetization losses [143]. The maximum amplitude of the magnetic field hitting the tape over one rotation of the machine rotor $H_0$ is applied in (3.39) to determine $P_B$. This result is then compared with the numerical loss results obtained from the 2D FEM slot model employing the $T-A$ formulation.

The 2D slot model was also analyzed when the HTS conductors carry the rated slot current $I_t$, and no magnetic field from permanent magnets is present, allowing the estimation of the HTS transport losses in self-field. In the 3D motor model, the remanent field of the magnets $B_r$ is set to zero, and in all slots, the rated slot current, 910 A, is imposed in the superconducting tapes. The analytical result for the transport loss solution for the nine tapes $P_{TN}$ (W/m) is determined for the imposed $I_t$ given by Norris' equation for a tape carrying an alternate current in self-field in (3.28) [161].

In the FEM model, the tape losses per unit length $P$ (W/m) are determined by the time integration of the instantaneous AC loss over the second cycle of the simulation (3.11). In Table 5.2, the analytical solutions are reported with the slot model results, showing coherent values and validating the model. Note that in each tested case (magnetization and transport loss estimation), the field determined in the 3D simulation is always imposed in the 2D model.

Table 5.2 FEM and Analytical AC Losses

| Model | 2D Slot model (W/m) | $P_{TN}$ (W/m) | $P_B$ (W/m) |
|---|---|---|---|
| Applied current | 0.273 | 0.234 | - |
| Applied field | 0.134 | - | 0.118 |

## 5.4 3D Slot Model

The proposed methodology developed for the 2D slot model can similarly be applied to construct a 3D model. In the AFPM motor simulations, the magnetic field distribution is acquired at each point of the analyzed armature slot. The resulting matrix $H_t(x,y,z,t)$ is stored and applied to the 3D slot model through magnetic field boundary conditions as in the 2D methodology, illustrated in the flowchart in Fig. 5.5 [51]. The $T-A$ formulation with the thin sheet approximation is used in the 3D slot to model the superconducting tapes.

The AC losses for the nine tapes in the 2D and the 3D slot models for the nine tapes inserted in the electrical machine armature at normal operating conditions, i.e., with applied current and field, are listed in Table 5.3. The 2D model provides the advantage of lower computation time, while the 3D model presents a more rigorous magnetic field representation, at the cost of increased simulation time. The difference between the performance of the superconducting tapes estimated with 2D and the 3D models can be attributed to the different mesh in each model due to the higher complexity and simulation time of the 3D model. Nonetheless, the loss estimation for both models is in agreement.

Table 5.3 AC Losses and computation time in 2D and 3D slot models

| Slot Model | P (W/m) | Simulation time [hh:mm:ss] |
|---|---|---|
| 2D | 1.24 | 00:20:40 |
| 3D | 1.52 | 14:28:51 |

Note that the end-windings are not included since this model only evaluates the losses inside the slot region. When the end windings are included in the model, the magnetic field surrounding the tapes outside the slot region will no longer stay parallel to the conductor surfaces, likely increasing superconductor losses. The end winding regions can be included in the 3D model by increasing the studied volume to include the entire coil.

## 5.5 Copper Layers Influence in HTS Armature AC Losses

With the multilayered HTS tape model proposed in Chapter 3, the impact of the copper layers on tape loss estimation is verified. The stabilizing copper layers and corresponding boundary conditions are introduced in the 2D slot model to each of the nine SC tapes as described in 3.4. The motor simulation defines the field at the slot boundaries as in 5.3. The mesh in the HTS layers of the single layer and multilayer tape models was defined with an equal number of elements to accurately compare results and simulation times, since a thinner mesh is usually required for good convergence in the multilayer model. The computed dissipated power in the tapes for the different models is stated in Table 5.4 with the respective simulation times.

Table 5.4 AC Losses and computation time in 2D single layer and multilayer slot models

| Slot Model | P (W/m) | Simulation time [mm:ss] |
|---|---|---|
| 2D single layer | 1.33 | 20:40 |
| 2D multilayer | 1.41 | 22:00 |

Considering the proximity between the results and similar simulation running times (due to a very similar mesh used for both models), it is shown that although the losses vary slightly, the results are still in close agreement. This means that for low operating frequencies (below 150 Hz) in the HTS coils, the simplification of using a single layer to model the coated conductor provides comparable results.

For the considered AFPM, the main differences between the partially superconducting and the conventional AFPM machine will be the winding losses, weight and cryostat power. The relevant performance metrics are listed in Table 5.5. Note that considering the armature losses and required cooling power in the HTS machine, the increase in the machine efficiency, excluding other losses (e.g. core losses and me-

Table 5.5 Comparison of Performance Metrics for Machines with Different Armature Windings

| Machine | Winding weight | $P_{Winding}$ | $P_{Cryocooler}$ |
|---|---|---|---|
| 1 - HTS AFPM | <1 (kg) | 6.1 (W) | 91-121.5 (W) [a] |
| 2 - $C_u$ AFPM | 5 (kg) | 578.9 (W) | - |

[a] to extract 1 W out of the cryostat at 77 K, 15-20 W are consumed by the cryocooler [63, 179].

chanical losses), is only 2.2%. This small increase in efficiency shows that designing a partially superconducting HTS machine might not be advantageous if the machine is designed in the same way as a conventional copper-wound electrical machine, since there is not a significant increase in efficiency when HTS coils replace the copper windings. Due to the high cost of the REBCO tapes and cryostat requirements, a partially or even fully superconducting machine might become competitive when the machine iron content is decreased, by taking advantage of the high current-carrying capacity and lightweight of HTS conductors, and manufacturing, for example, ironless prototypes. This means a higher specific torque can be achieved by increasing the magnetic loading of the machine and decreasing its weight. In such conditions, however, due to the different path of the magnetic field surrounding the windings, the superconductor winding working conditions should be thoroughly investigated to guarantee good performance of the HTS conductors with reduced AC losses.

## 5.6 SCSC Cables in Electrical Machine Armature Windings

Several strategies have been proposed to address the challenge of minimizing AC losses and magnetic field effects on HTS material performance, which play a critical role in the efficiency of superconducting windings. Literature reports various techniques for reducing AC losses in superconductors, including the striation of SC tapes, which is particularly effective in decreasing SC hysteresis losses as these are proportional to the square of the width of the superconductor [180, 181, 67]. Yet, while a significant reduction in the losses can be achieved with striation, the superconducting tape filaments have reduced critical currents. Improved conductor stability and reliability can be achieved by adding copper plating (as depicted in

Fig. 5.7) to the filamented tapes to allow current sharing between filaments in case one filament quenches [182]. The copper plating, however, also makes the multifilament structure ineffective for loss reduction under applied magnetic fields since it creates a conductive path between filaments for the shielding current [183].

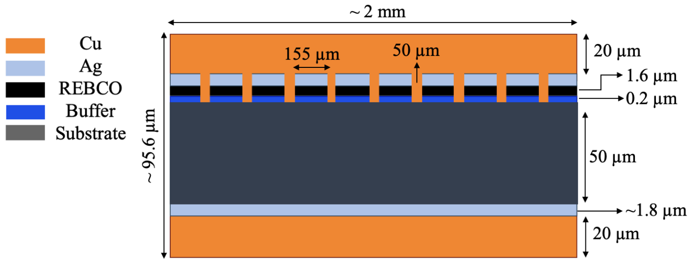

Fig. 5.7 Striated copper plated coated superconductor, not to scale.

Additionally, suppose the cable core around which the tapes are wound is made of conducting material. In that case, it can also provide an alternative current path in case of quench of one or more superconducting strands. This contributes to increasing the cable operation stability and ensures higher mechanical flexibility of the conductors [75]. Nonetheless, copper cores manifest eddy current losses. Hence, depending on the operation conditions, HTS cables can be fabricated with tapes wound around non-conductive materials such as Glass Fibre Reinforced Plastic to limit core losses [75].

The mechanical limitations of SC tapes, such as brittleness and fragility, restrict them to being bent only over their flat face, with specific bending restrictions that make it challenging to implement certain winding topologies in electrical machines, such as distributed windings. In contrast, superconducting Spiral Copper-plated Striated Coated-conductor(SCSC) cables can be bent in all directions due to their spiral structure, regardless of their minimum bending radius. Due to the twisted geometry of the tapes, the losses in superconducting cables also remain unaffected by the direction of the surrounding magnetic field. This means that changes in magnetic field direction in end-winding regions will have minimal impact on superconducting losses. The copper plating on the HTS tapes and the conducting core of the cable provide stability against quench. The spiral geometry grants low loss at operating frequencies up to a few kHz [184] and low impact with the field direction change on end winding regions, making the cables appropriate for application in electrical machine armature windings, where they are exposed to alternate fields and currents. To verify the cables applicability in electrical machine windings and compare their performance with that of HTS tapes in the same operating conditions, the slot model is used to analyse the cables performance.

### 5.6.1 SCSC 3D and 2D Cable Model

For this study, SCSC cables with two tapes per layer, four layers, and a cable core diameter of 3 mm developed by Amemiya lab at Kyoto University [75] are considered. The cables coupling time constant is experimentally measured to be below 0.05 ms, making the coupling frequency $f_c$=1/2$\pi\tau_c$ of the considered cables above 3 kHz [77]. This means the filaments are uncoupled for the considered operating conditions in the AFPM armature windings (100 Hz), and during stable operation, no current will be shared between the HTS filaments, making cable losses mostly hysteretic [185]. In this situation, the copper plating does not need to be considered when modelling the SCSC cables, since coupling trough the copper plating does not occur.

Since the cable losses are mostly hysteretic, this means that loss estimation in 2D models, i.e. that do not represent the twisted geometry of the tapes provides results that are close to those obtained by 3D models. Since the spiral geometry is meant to uncouple the filaments, it is possible to approximate the AC losses by a 2D model. The 2D single-slot model is applied to estimate losses in the superconductors. The details of the modelled multifilament coated conductor can be found in Table 5.6 [77].

Table 5.6 Striated Coated Conductor Parameters at 77 K

| Parameter | Value |
|---|---|
| $I_c$ (A) | 35 |
| $B_0$ (mT) | 150 |
| $n$ (A) | 21 |
| Tape width (mm) | 2 |
| Number of SC filaments | 10 |
| Width of SC filaments (mm) | 0.155 |
| Copper width ($\mu$m) | 50 |

Notice that here the main focus is on estimating the loss in SCSC cable armature windings. Therefore, only cables suitable for a test setup were considered. For the practical implementation of superconducting armature windings, it would be preferable to use SCSC cables wound with tapes of higher critical currents and a greater number of filaments. Figure 5.8a illustrates the geometry of one pitch of the cable. The model includes only the superconducting filaments, as the current primarily flows in the SC layers for the study operating conditions. The 2D cable geometry shown in Fig. 5.8b represents the cross-section of the 3D model, taken through a plane perpendicular to the axial direction of the cable ($z-$axis in Fig. 5.8a).

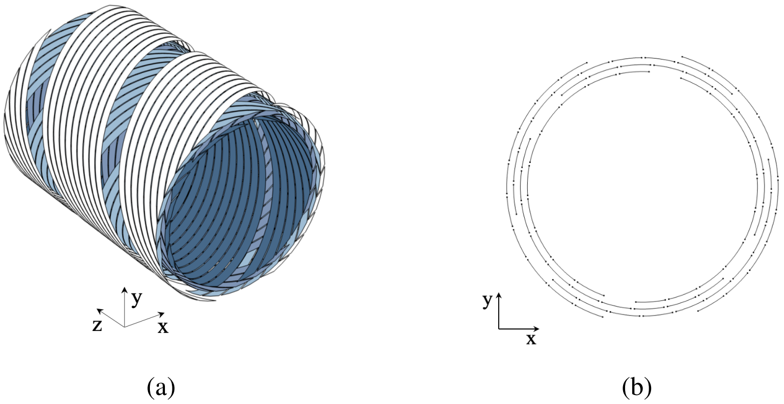

(a) (b)

Fig. 5.8 Illustration of one pitch of the SCSC cable, modelled by the thin sheet approximation in 3D (a) and 2D models (b).

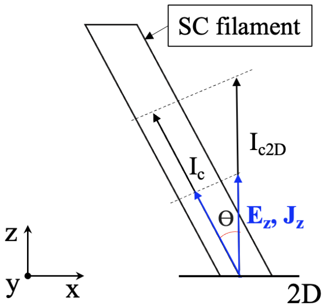

Fig. 5.9 Illustration of one filament of the SCSC cable with representation of the considered variables.

Figure 5.9 shows a superconducting filament with the 2D model variables. It is important to note that the current defined in the 2D model, $J_z$, is perpendicular to the model plane. Additionally, the width of the tapes is increased by a factor of 1/cos($\theta$), where $\theta$ represents the angle between the coated conductor and the cable axis ($\theta$ = 64° for the considered SCSC cable). Therefore, the critical current in the 2D model, $I_{c2D}$, must also be increased by the same factor, becoming $I_c$/cos($\theta$).

Similarly, the calculated variables in the 2D model, **E** and **J**, used to evaluate the tape losses must be corrected by a factor of cos($\theta$). The $T-A$ formulation is applied in FEM to both 2D and 3D models to estimate the cable's AC loss for an externally applied alternate magnetic field $H_m(t) = H_0 \sin(\omega t+\phi)$, in the $y-$axis direction. The applied magnetic field amplitude is varied between 10 mT and 100 mT, and its frequency $f$ is set as 112 Hz in agreement with results in [77]. The current distribution is plotted for both models in Fig. 5.10a for a magnetic flux density amplitude $B_m$ of 100 mT. Since the 2D and the 3D models' current density profiles agree and $E-J$ parameters are the same, the losses must also agree. The magnetization losses (per cable meter) for different values of magnetic field amplitude are shown in Fig. 5.10b with the experimental results reported in [77]. Analytical results for magnetization losses for SC tapes under applied transverse magnetic field, $Q_{BI}$ (3.39) are also compared. Regarding the analytical results shown in Fig. 5.10b, $n_f Q_{BI}$ corresponds to the magnetization loss contribution for all filaments. The result given by $2/\pi n_f Q_{BI}$ has an added factor of $2/\pi$ to account for the portion of the tape that is impacted by the external magnetic field due to the cable spiral structure [184]. In electrical machines, it is realistic for the armature windings to experience magnetic slot leakage flux densities ranging from 10 to 100 mT during standard operation, that is, if the machines have an iron core (aircore machine stator slots would have much higher leakage flux densities). In these conditions, experimental and analytical results support the 2D model.

It is noticeable that results from the 2D model are considerably higher than those obtained from the 3D model. This is first due to the different meshes in both models. The 2D model has more elements per width than the 3D cable model since the latter can take weeks to solve if the mesh is finer, while the 2D model is solved in a few minutes. The difference in experimental results and analytical estimation might be due to the fact that analytical equations do not consider different current penetration in the different layers of the conductor. The analytical estimation is based on the assumption that all layers have the same penetration length (dependent on the applied magnetic field amplitude), when in fact, the outer layers partially shield the inner layers from the external magnetic field. This results in different field penetration for

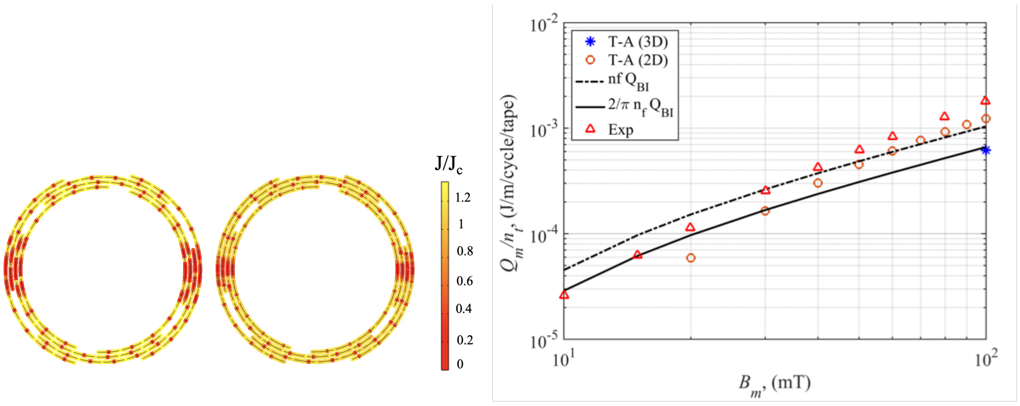

(a) (b)

Fig. 5.10 Simulation results for the SCSC cables with externally applied magnetic field, current density profile (a) and (b) Magnetization loss results for the SCSC cable with varying external applied magnetic field amplitude.

the different layers. It should also be noticed that the effect of the self-field from each filament on the surrounding tapes is not taken into account, which might contribute to a slight inconsistency between analytical and experimental results

Figure 5.11a depicts the slot model methodology for the SCSC cables where conducting cylinders were added in the 3D FEM model to obtain the magnetic field distribution inside the armature slot. Fig. 5.11b shows the magnetic flux density colour shade map $|\mathbf{B}|$ and flux density arrow surface resulting from the 2D FEM slot model where the superconducting material definitions and the $T-A$ formulation were added. Table 5.7 lists the estimated losses computed by the slot model for the SCSC cables and SC tapes positioned parallel and perpendicular to the machine's leakage magnetic field.

The resulting losses for the SCSC cables are higher than those calculated for the REBCO tapes when the external field is parallel to the tape's surface and lower than those for tapes perpendicular to the external magnetic field, i.e., rotated 90° relative to the position shown in Fig. 5.6. This result is expected since the superconductor performance is significantly impacted by external fields perpendicular to the surfaces of the tapes and filaments. However, it also demonstrates the advantage of the reduced influence of magnetic field direction on AC losses in SCSC cables. The low impact of the field direction in SCSC cable losses and their mechanical flexibility provides greater freedom in the winding design for superconducting electrical machines.

The lower AC losses in the cables and improved stability against quench show the applicability of SCSC cables in armature windings.

Table 5.7 Losses computed in the 2D slot model for SCSC cables and REBCO tapes oriented parallel and perpendicular to the armature leakage flux

| Model | P (W/m) |
|---|---|
| SCSC cables | 4.91 |
| REBCO tapes $\parallel$ | 1.24 |
| REBCO tapes $\perp$ | 18.1 |

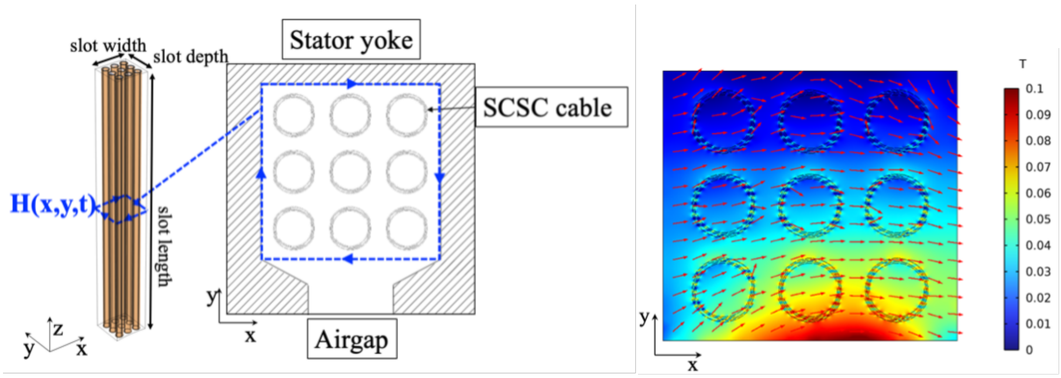

(a) (b)

Fig. 5.11 Slot model with SCSC cables (a) methodology and (b) magnetic flux density colour shade map and $B_x$, $B_y$ surface plot arrows.

## 5.7 Summary

This Chapter presents an extension of an electromagnetic slot model designed for expedited analyses of loss estimation in superconducting armature windings. The proposed methodology allows for estimating losses in electrical machine armature slots that, due to their complex geometry, require 3D motor models. The 2D methodology significantly reduces the simulation time and complexity, while considering all time and spatial harmonics of the stator slot magnetic field contributes to an accurate description of the working conditions of the superconducting coils. A 3D slot model was developed using the 2D model methodology. The proposed

2D and 3D modelling approaches allow restricting the FEM simulation only to the slot and the SC elements, avoiding dealing with moving mesh for the rotor and other non-linear materials such as the laminated iron core and significantly reducing the computational requirements for the loss estimation of superconducting AC windings. The 2D and 3D models were validated with analytical formulations reported in the literature for calculating losses in superconducting tapes with applied AC currents or subject to alternate magnetic fields.

The computation time of the 2D model proposed in this Chapter is increased, relative to the model proposed in Chapter 4 [49], and its losses are reduced. Nonetheless, the AC losses evaluated for the nine SC tapes using the 2D extended slot model have reduced relative error (18%) compared to the 3D model, when compared to the 2D model presented in [49], for which errors go up to 38%. Overall, the extended model shows consistency in the magnetic field representation compared to the result obtained in the 3D model and the motor simulation, which is essential for evaluating superconducting tape performance and accurately estimating its losses.

The slot model is implemented to estimate losses for different conductor typologies and investigate methods that can mitigate superconducting losses in armature windings. For this study, low AC loss and quench resilient multifilament conductor cables (SCSC) are chosen to study their implementation in the armature slots of the case study toroidal AFPM. The results of this investigation show the applicability of the SCSC cables in armature windings and the applicability of the slot model in investigating the performance of different HTS materials for machine design.

# Chapter 6

# Slot Thermal Model

## 6.1 Introduction

This Chapter presents a methodology for estimating the cooling requirements of superconducting windings by proposing a complementary slot thermal model. Based on the loss estimation obtained through the extended slot model methodology in the previous Chapter, a complementary thermal model is introduced. The thermal study is intended to estimate the cooling efficiency of the superconducting coils inside the electrical machine armature slots. The model can help machine designers find suitable cryostat specifications, such as flow rate and cooling temperature, for the safe operation of the HTS windings. The analysis considers that each coil is cooled individually using liquid nitrogen. Material characteristics and fluid and thermal laws for the developed thermal model are stated, and numerical results are experimentally verified.

## 6.2 Slot Thermal Model

The main purpose of the thermal model is to help estimate the conditions that maintain the temperature of the superconducting coils stable at the cooling fluid temperature ($LN_2$). Under thermal equilibrium, the HTS material parameters (temperature-dependent) are constant. This means thermal and electromagnetic analyses can be kept separate, making the models less complex and reducing simulation time and computer memory requirements. Since the HTS tape position in the previous study for the AFPM machine slot model would make the winding challenging to build and support, a more practical geometry was chosen for the thermal analyses. The HTS tapes are considered to be wound with a thin layer of Kapton tape for electrical insulation. The electromagnetic model is used to evaluate different positions for the tapes and winding layouts, i.e., double-layer and single-layer coils. The tapes were modelled with electrical insulation as shown in Fig. 6.1a, and the insulating layer (Kapton tape) thickness was varied, and the AC losses were determined for different intertape distancing by the slot model as shown in Fig. 6.1b. For each distance, the losses were evaluated, and the placement for the tapes, which reduces the HTS tape losses and keeps a feasible coil for the considered cryostat thickness, was determined, as shown in Fig. 6.1b, where the cryostat walls form a squared duct surrounding the tapes. The losses for the different distances between the tapes are shown in Fig. 6.2.

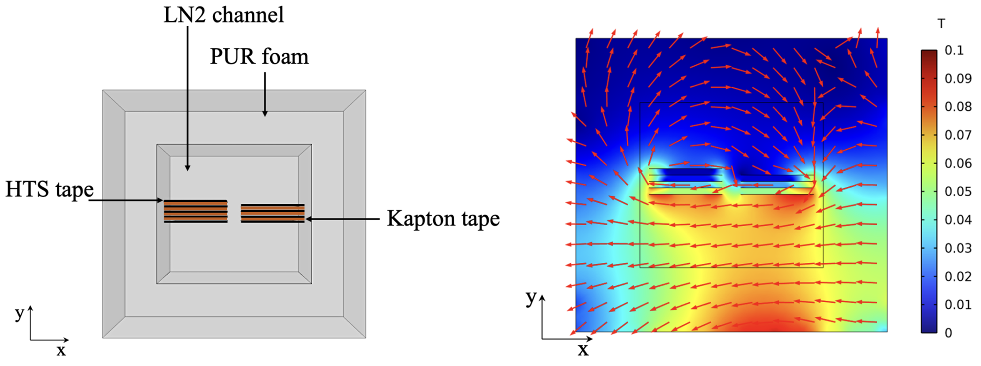

(a) (b)

Fig. 6.1 Slot cross section detail showing the superconducting tapes and Kapton layer insulation (a) and **B** colour shade map and magnetic flux density arrow surface $B_x$ and $B_y$ for minimum tape distance and (b) .

The coil in the chosen configuration has the lowest spacing between tapes, equivalent to 1 standard Kapton tape layer (127$\mu$m). The nine tapes have an average dissipation of 2.7 W/m. Although this configuration has higher losses, it guarantees enough space in the armature slot for a layer of insulation material. Additionally, it ensures sufficient distance between the tapes and cryostat walls, facilitating the cooling, winding, and support of the coils.

In the thermal model, the armature conductors are defined as surface resistive heaters with a dissipation of 2.7 W/m, defined as a constant heat rate of 0.38 W

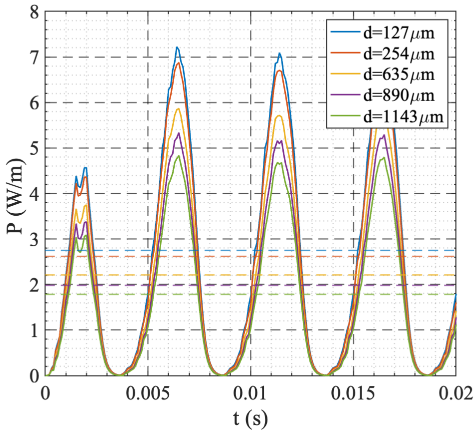

Fig. 6.2 AC loss results obtained by the slot model for different spacing between tapes.

according to the length of the tapes. The superconducting formulations and their non-linear characteristics are not described for the thermal model. Nonetheless, the thermal conductivity, thermal capacity, and density of the tapes are defined according to REBCO material characteristics.

### 6.2.1 Heat Transfer Phenomena in a Liquid-Cooled Slot

In FEM models, the heat transfer simulations are defined by the heat conservation laws in fluids for the fluid domains as stated in (6.1) and by the Fourier law defining the heat flux for solid domains (6.2).

$$\rho_i \, C_{pi} \, \frac{\partial T}{\partial t} + \rho_i \, C_{p_i} \, \mathbf{u} \cdot \nabla \mathbf{T} - k_i \nabla^2 T = Q \tag{6.1}$$

$$\mathbf{q} = -k_i \, \nabla \mathbf{T} \tag{6.2}$$

In the heat equation for convective and diffusive heat transfer (6.1), $\rho_i$ is the $i$-th material density (kg/m$^3$), $C_{pi}$ is the cooling material heat capacity at constant pressure (J/kg·K), and $k$ is the thermal conductivity (W/m·K). The first equation describes heat transfer by convection and diffusion and models the superconducting tape heat transfer to the surrounding liquid nitrogen. The Fourier law can determine the heat flux between the several layers of the tape and between the cryostat/insulation walls and the ambient. The hysteresis and resistive losses generated by the REBCO tape are imposed in the thermal model by defining the superconducting surfaces as boundary heat sources with constant heat rate $P_0$ (W/m), obtained from the electromagnetic study performed in the AFPM slot model. To define the model materials, the thermal characteristics of the different materials according to operation temperature are stated in Table 6.1 [162, 186, 187].

### 6.2.2 Material Thermal Characteristics

The thermal study is performed considering a non-metallic cryostat, where the coils are enclosed in a channel where liquid nitrogen circulates. Since alternate magnetic fields impact the windings, non-metallic insulation is assumed to guarantee that the coil enclosure does not act as an electromagnetic shield or affect the linked flux by the armature windings. Non-conducting materials also eliminate eddy current losses on cryostat walls, which inevitably generate an extra heat source inside the machine and increase the cooling requirements of the cryostat. In addition, literature reports that non-metallic cryostats can help reduce the system volume and weight, which can be particularly important in achieving higher torque densities [188]. Several solutions are available in the literature to insulate the coils. Usually, a vacuum layer is preferred to prevent heat conduction between the ambient and cryogenic systems [189]. However, for simplicity, high-density polyurethane (PUR) is chosen due to having a low thermal conductivity in the range of 0.025 W/m· K and low weight, as well as being widely available and affordable. The thermal characteristics of the REBCO tapes are defined for RRR = 40 in the copper layers, corresponding to the available tapes for experimental tests [73]. The material thermal characteristics for modelling the REBCO tape at 77 K are listed in Table 6.1 [162].

Table 6.1 Thermal properties of REBCO coated conductor materials at 77 K

| Material | k (W/m K) | $\rho$ (kg/m$^3$) | $C_p$(J/kg K) |
|---|---|---|---|
| YBCO | 5.914 | 6390 | 88.69 |
| $A_g$ | 530.4 | 10630 | 161.4 |
| $C_u$ | 431.2 | 8960 | 218.1 |
| Hastelloy | 7.801 | 8890 | 163.5 |
| Homogenized | 204.1 | 8936 | 185.2 |

Using Fourier's law of conduction in (6.2), it is possible to define for the HTS tape a homogenised heat conductivity considering its thermal resistance model.

The thermal conductivity of the tape is anisotropic and can be considered in two directions: transverse or parallel to the several layers of the tape. According to Fourier's law of conduction, the rate of heat conduction through a layer of material $i$ with area $A_i$ and thickness $L_i$ can be defined by a thermal resistance $R_{\theta i}$ as in (6.3).

$$Q = \frac{T_1 - T_2}{R_{\theta i}}, \qquad R_{\theta i} = \frac{L_i}{k_i\, A_i} \tag{6.3}$$

Using (6.3), the thermal resistances for the $n_L$ layers of the REBCO tape with defined in the normal direction of the tape wide face can be determined by the equivalent series resistance. The thermal resistance transverse to the thin side of the tape (normal to the 95.6$\mu$m face) is determined by the parallel resistance contribution [162]. The equivalent thermal conductivities transverse, $k_\perp$, and parallel, $k_\parallel$, to the tape surface can be obtained by (6.4).

$$\frac{1}{k_\perp} = \frac{\sum_{i=1}^{n_l} \frac{A_i}{k_i}}{\sum_{i=1}^{n_l} A_i}, \qquad k_\parallel = \frac{\sum_{i=1}^{n_l} A_i k_i}{\sum_{i=1}^{n_l} A_i} \tag{6.4}$$

To homogenize the material heat capacity, the contribution of each layer is accounted for by considering its contribution using the heat capacity per unit volume and density of each layer $C_{vi}$ and $\rho_i$ to obtain (6.5) [190].

$$C_v = \frac{\sum_{i=1}^{n_l} C_{vi} A_i}{\sum_{i=1}^{n_l} A_i} \tag{6.5}$$

The homogenised specific heat capacity of the tape at constant pressure $C_p$ is then obtained by the ratio between the homogenized heat capacity per unit volume and tape density, $C_v$ and $\rho$ (6.6) determined by (6.7).

$$\rho = \frac{\sum_{i=1}^{n_l} \rho_i A_i}{\sum_{i=1}^{n_l} A_i} \tag{6.6}$$

$$C_p = \frac{C_v}{\rho} \tag{6.7}$$

The heat rate contribution from the ambient (external to the slot walls) is determined by the expression for natural convection, as the slot is surrounded by air at standard ambient temperature and pressure (298.15 K and 1 atm). For vertical walls and laminar external flow, the heat flux through convection is given by (6.8).

$$q = h(T_{ext} - T) \tag{6.8}$$

In (6.8), $h$ (W/m$^2$·K) is the heat transfer coefficient. For the vertical cryostat walls, the natural heat transfer coefficient is given by $h_v$ (6.9). For horizontal surfaces, the heat transfer coefficient for free convection on the upper surface of a cold plate is given by $h_{hu}$ and by $h_{hl}$ for the lower surface, with expressions (6.10) and (6.11) respectively [191].

$$h_v = \frac{k_i}{L}\left(0.68 + \frac{0.67Ra_L^{1/4}}{(1+(\frac{0.492k_i}{\mu C_{pi}})^{9/16})^{8/27}}\right) \quad \text{if} \quad Ra_L \leq 10^9 \tag{6.9}$$

$$h_{hu} = \frac{k_i}{L}0.27Ra_L^{1/4} \quad \text{if} \quad 10^5 \leq Ra_L \leq 10^{10} \tag{6.10}$$

$$h_{hl} = \begin{cases} \frac{k_i}{L}0.54Ra_L^{1/4} & \text{if} \quad 10^4 \leq Ra_L \leq 7^{10} \\ \frac{k_i}{L}0.15Ra_L^{1/4} & \text{if} \quad 10^7 \leq Ra_L \leq 10^{11} \end{cases} \tag{6.11}$$

In (6.11) and (6.10) $Ra_L$ is the Rayleigh number determined by the characteristic length of the geometry $L$ and given by the expression in (6.12).

$$Ra_L = Gr_L Pr \tag{6.12}$$

$Gr_L$ is Grashof's number (6.13) defined for $g$ (m/s$^2$), the gravity acceleration, $\beta$ the thermal expansion coefficient, $L$ the height of the cryostat wall and $\nu$ the kinematic viscosity of the fluid.

$$Gr_L = \frac{g\beta(T_s - T_\infty)L^3}{\nu^2} \tag{6.13}$$

In (6.13), $T_s$ is the surface temperature, $T_\infty$ is the ambient temperature, and $Pr$ is Prandtl's number given by the ratio between the kinematic viscosity and the material thermal diffusivity $\alpha_i$=$k_i/\rho_i C_{pi}$.

### 6.2.3 Liquid Flow Model

To model the liquid cooling of the superconducting tape windings, laminar flow conditions are assumed in the FEM model according to experimental conditions

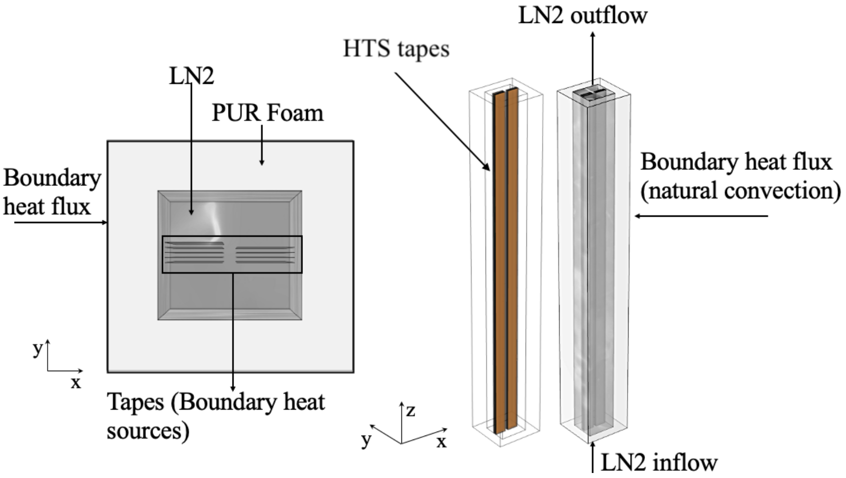

Fig. 6.3 Illustration of the thermal slot model with heat transfer and fluid flow boundary conditions.

available for testing the thermal model which will be discussed in 6.2.4. However, it is essential to note that laminar flow is also ideal for cooling the windings since turbulent flow can introduce evaporation and air bubbles inside the channel, reducing the cooling efficiency and creating hotspots in the superconducting tapes. The fluid flow model is defined by the Navier-Stokes equation in (6.14), and the mass conservation is given by the continuity equation for incompressible fluids in (6.15) [192].

$$\rho\frac{\partial \mathbf{u}}{\partial t}+\rho\mathbf{u}\cdot\nabla\mathbf{u}-\mu\nabla^2\mathbf{u}=-\nabla p+\rho g \tag{6.14}$$

$$\frac{\partial \rho}{\partial t}+\rho\mathbf{u}\cdot\nabla\mathbf{u}=0 \tag{6.15}$$

In (6.14) and (6.15), **u** is the fluid velocity vector (m/s), and $p$ is the fluid pressure (Pa). A condition of no slip on the walls is considered (**u** = 0). The material properties for $N_2$ in both liquid and gaseous states are temperature dependent and can be found in material databases [193].

For the PUR, the parameters were defined as $k$ = 0.025 W/m·K, $C_p$ =1400 J/kg/K, $\rho$ = 40 kg/m$^3$ [187]. The geometry of the thermal slot model is shown in Fig. 6.3. The inlet velocity, i.e., normal to the slot cross-section, is varied according to the cooling requirement of the HTS tapes. A first estimation for the fluid velocity can be obtained, neglecting the natural convection from the air and estimating the heat transferred by conduction through the PUR walls. Using the shape factor $S_f$ for a squared duct, such as the cryostat assumed for the slot model, the conduction heat rate can be calculated as stated in (6.16) [191].

$$q = S_f k \Delta T_{1,2} = \frac{2\pi\, L_{slot}}{0.930\, \ln(\frac{w_o}{w_i}) - 0.05} \tag{6.16}$$

In (6.16) $L_{slot}$ is the slot length (0.14 m), $w_o$ is the outer width of the slot, 0.017 m, and $w_i$ is the $LN_2$ channel width, 0.010 m. The assumed temperatures of each wall are 293.15 K and 75 K. The analytical conduction heat rate is 10.82 W. The same result is obtained through the FEM model (10.76 W) for fixed temperatures on the slot walls, defined as constant 75 K at the channel inner walls and 293.15 K at the channel outer walls of the PUR insulation. However, if the study is performed with these inner and outer channel temperature values defined as initial conditions instead of fixed throughout the simulation, the stationary result for the equilibrium temperatures at the walls changes, and the resulting heat rate becomes 5.72 W. This happens because the analytical formulation considers a constant temperature at each surface, assuming thermal equilibrium conditions at each surface.

Nonetheless, the heat rate results can be used to estimate the fluid velocity that can maintain the temperature in the tapes constant with (6.17).

$$q = \dot{m} C_p (T_2 - T_1) \tag{6.17}$$

In (6.17) $\dot{q}$ is the conduction heat rate (W), $\dot{m}$ (kg/s) is the flow rate of the fluid inside the channel. For the estimated conduction heat rates and the dissipated power in the HTS tapes, the minimum flow velocities for a maximum increase of 1 K inside the slot correspond to 0.075 m/s or 0.4 L/min and 0.041 m/s or 0.22 L/min for the 11.2 W and 6.1 W, respectively, guaranteeing dissipation of tape losses and the ambient temperature losses. Since the conditions closest to the experiment are those without fixed wall temperatures, the results for a FEM stationary simulation where the wall temperatures are defined only as initial values are shown in Fig. 6.4. The results show that the flow velocity can be accurately estimated using the stationary simulation and analytical results in (6.17).

### 6.2.4 Experimental Results

A setup was constructed to measure the temperature of a superconducting coil cooled in a liquid nitrogen channel of similar dimensions to the AFPM armature

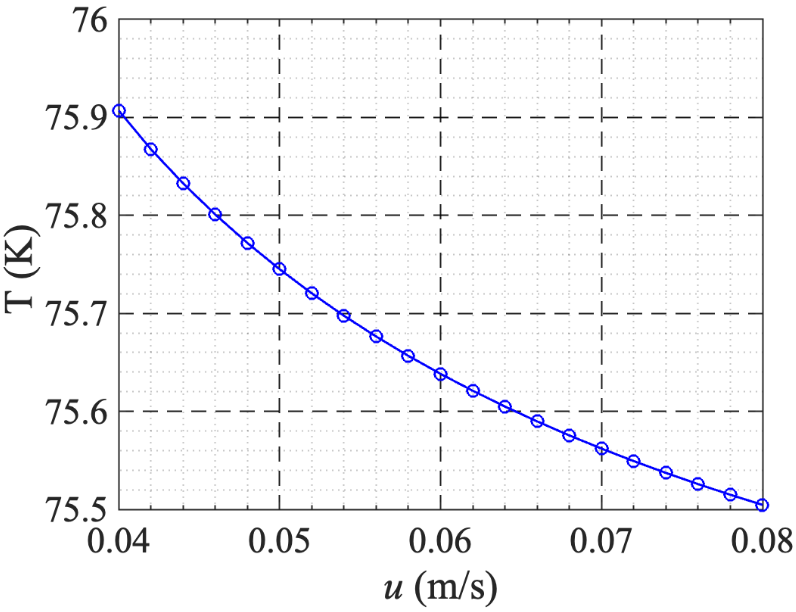

Fig. 6.4 Average temperature inside the slot in equilibrium conditions (stationary study) for different flow velocities of liquid nitrogen.

coil to verify the thermal model. The cooling channel was filled with $LN_2$ using the cryogenic pump. The flow in the cooling channel was observed to be laminar, having smooth, parallel streamlines and the absence of turbulence. A short-circuited superconducting coil was inserted in a PUR cryostat and excited by a magnetic circuit. The primary coil is connected to a sinusoidal power supply for excitation and kept at ambient temperature. This type of setup was considered so that losses caused by the current leads can be neglected in the FEM model. Figure 6.5 depicts the circuit components.

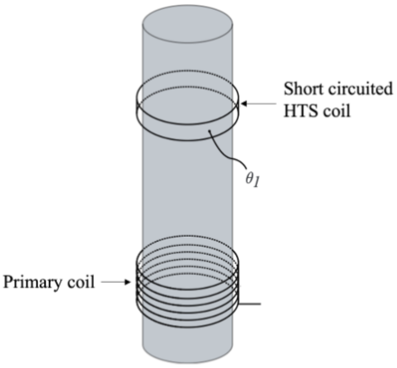

Fig. 6.5 Circuit diagram for measurement of magnetisation losses in short-circuited HTS coil

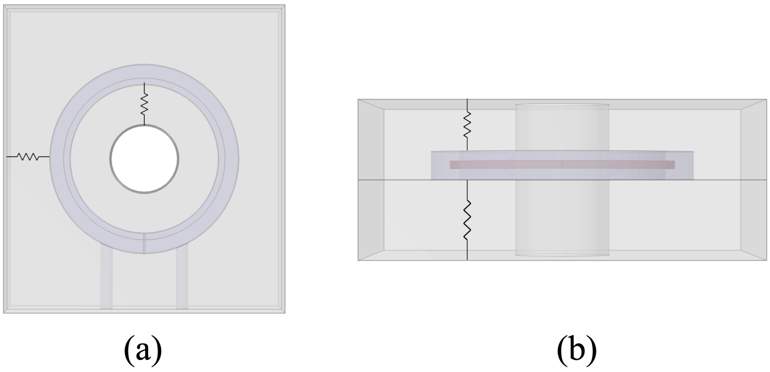

Fig. 6.6 Thermal resistances in the cryostat setup, shown in lateral view (a), and from above (b)

### Material Calibration

The thermal conductivity of the insulation material is verified experimentally by filling the cryostat with liquid nitrogen and measuring its evaporation rate. The weight of the cryostat with $LN_2$ is measured over time until all liquid inside the cryostat evaporates at ambient temperature. The ambient and cryostat surface temperatures are measured by a PT100 sensor. The insulating PUR material thermal conductivity is estimated using the equivalence in (6.18).

$$Q_{evap} = L\frac{dm_{LN_2}}{dt} = \frac{(T_{out} - T_{LN_2})}{R_{PUR}} \tag{6.18}$$

In (6.18) $T_{LN_2}$ is the phase change temperature of liquid nitrogen, 77 K and $L$ is its latent heat 199 J/g and $R_{PUR}$ is the thermal resistance of the PUR cryostat. Note that according to the setup geometry, the thermal resistances for the heat flow between the cooling channel and ambient temperature are as shown in Fig. 6.6. The cryostat thermal resistances are calculated for each surface of the cooling channel and added in parallel as in (6.4) with the resistances computed according to the geometry of the setup. In this way, the thermal conductivity is isolated as in (6.19).

$$R_i^{PUR} = \frac{1}{k_{PUR}}\frac{L_i}{A_i} \tag{6.19}$$

In (6.19), $R_i^{PUR}$ is the thermal resistance of each cryostat wall, $L_i$ and $A_i$ are its thickness and area, and $k_{PUR}$ is the material thermal conductivity to determine. This means the parallel thermal resistance of all walls is given by

$$\frac{1}{R_{||}} = k_{PUR} \sum_{i}^{4} \frac{1}{L_i/A_i} \tag{6.20}$$

Considering that the liquid volume inside the channel evaporates during the experiment, the contact area between the liquid and the channel walls will change depending on the evaporated $LN_2$ mass. Since the thermal resistance is a function depending on the contact area between the fluid and the cryostat walls, as shown by (6.3), the percentage of $LN_2$ mass inside the cryostat is taken into account to obtain the thermal conductivity as in (6.21).

$$k_{PUR} = \frac{R_{||} k_{PUR}}{m/m_0} \frac{Q_{evap}}{dT} \tag{6.21}$$

In (6.21), $m$ is the measured mass at each instant, and $m_0$ is the initial mass of the cooling fluid. The results for the measured mass of the cryostat over time and the estimated thermal conductivity are shown in Fig. 6.7.

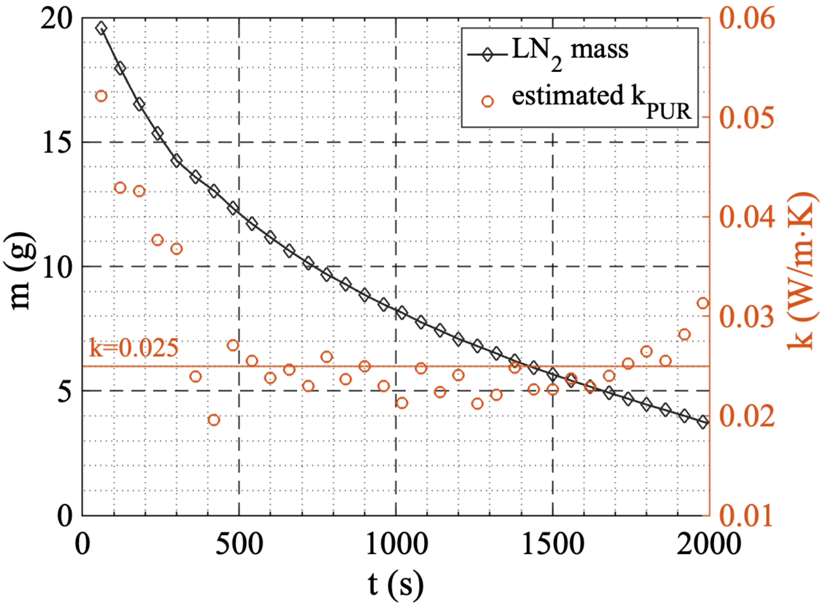

Fig. 6.7 Thermal experiment $LN_2$ mass evolution and estimated thermal conductivity for the PUR material.

Note that although the results in Fig. 6.7 vary slightly from the conductivity specified by the manufacturer (0.025 W/m·K), the natural convection for both the $LN_2$ inside the channel and the air outside the cryostat was not accounted for in the thermal conductivity estimation. Hence, a deviation from the estimated and manufacturer conductivity is expected.

The measured mass of $LN_2$ is plotted alongside the thermal conductivity result to better identify the regions where higher inaccuracies are found for the $k_{PUR}$ estimation. In the beginning of the experiment, the channel temperature is the ambient temperature (not the 77 K considered in (6.18)), this means that until the inner channel temperature stabilizes to the $LN_2$ temperature, the analytical estimation deviates from the manufacturer given specification of 0.025 W/m·K. At the end of the measurement, due to the low sensibility of the weight measurement system, the analytical results lead to oscillation in the conductivity estimation. However, the remaining results are in agreement with the characteristics provided by the manufacturer, and therefore, the thermal conductivity of the PUR material is verified.

### Thermal Model Preliminary Validation

To validate the thermal model, the short-circuited REBCO single-turn coil was inserted in the $LN_2$ channel and supplied with an alternate current at 50 Hz frequency through the primary circuit in Fig. 6.5. The PUR cryostat was tightly sealed to prevent leakage, and a PT100 temperature sensor was attached to the HTS coil

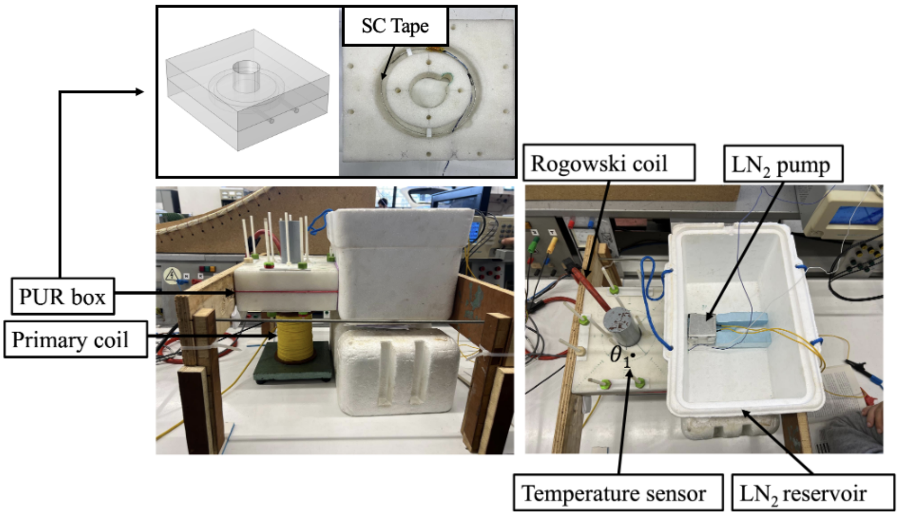

Fig. 6.8 Experimental setup to measure temperature in an HTS coil cooled by $LN_2$, $\theta_1$ marks the approximate location of the temperature sensor.

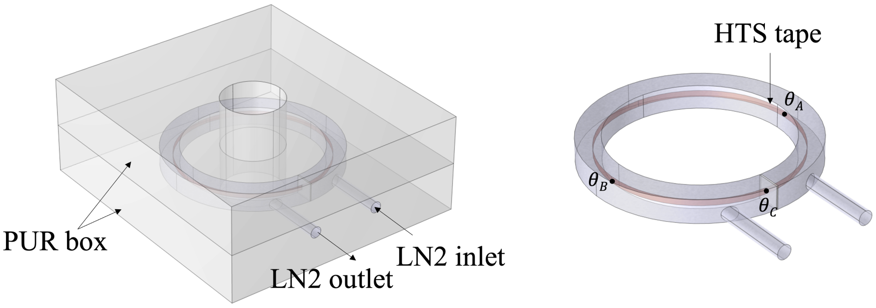

(a) (b)

Fig. 6.9 Simulated model of the cryostat (a) and detail of $LN_2$ channel with superconducting tape (b)

inside the cryostat channel to measure the coil temperature. Inlets and outlets were connected to an $LN_2$ reservoir, where a cryogenic pump was added to circulate the liquid nitrogen into the cooling channel with a flow capacity of 2-4 L/min. A Rogowski coil was added to the electrical circuit to measure the current flowing in the HTS coil. The complete experimental setup is shown in Fig. 6.8. Note that although the current in the tape is measured, its voltage was not measured since it would be difficult to keep both the temperature sensor cables and voltage taps through the outlet of the cooling channel. However, for a single-turn pancake coil and an HTS short sample supplied with an alternate current under self-field conditions, the losses are equal [194]. Therefore, the HTS coil losses are estimated with transport AC loss data in Chapter 3 and are imposed in the FEM model. The setup was modelled in 3D in FEM with the HTS tape defined as a surface resistive heater with the thermal characteristics of the homogenised tape in Table 6.1. The geometry of the model is shown in Fig. 6.9. For each test, the adjacent reservoir was filled with $LN_2$, and the pump was connected to a power supply; its flow rate was controlled by the imposed voltage. The primary circuit was supplied with an alternate power source to excite the HTS short-circuited coil on the secondary circuit. For each imposed flow rate, several current amplitudes were supplied to the HTS coil. Since the temperature sensor measured only the liquid nitrogen temperature and no temperature increase in the tape was detected, the experiment was performed to determine the minimum flow rate for each imposed current that ensures the tape carries current without quenching. When the tape losses are too high to be dissipated by the imposed flow rate, the quench is detected by a sudden drop in the measured current, determining the limit losses for the imposed flow rate. The flow rate is then increased to ensure the dissipation of the tape losses, and the current is increased once again until the limiting flow is determined. Table 6.2 shows the measured limit current and corresponding flow rates.

Table 6.2 Measured RMS currents and properties of REBCO coated conductor materials at 77 K.

| $I_{RMS}$ (A) | HTS losses (W/m) | Flow rate (L/min) | inflow velocity (m/s) |
|---|---|---|---|
| 155 | 1.2 | 1.3 | 0.3 |
| 175 | 3.2 | 1.9 | 0.5 |
| 235 | 26 | 2.6 | 0.7 |

The FEM thermal model was initially simulated with a stationary study without phase change in the liquid nitrogen to obtain an equilibrium temperature distribution between the inner channel at initial temperature $T_0$=75 K and the ambient temperature (external to the cryostat) $T_\infty = 293.15$ K. This stationary study solution is imposed as the initial condition in the subsequent time-dependent study. This initial stationary step was added to accelerate the time-dependent study, which is significantly more complex and time-consuming, as it includes both transient effects and the phase change phenomena of liquid nitrogen.

The phase change module was added in the time-dependent study, and the solution was computed for a simulation time of 60 s, after which the system was found to be in equilibrium conditions, and three temperatures $\theta_A$, $\theta_B$ and $\theta_C$ were obtained in different coil positions as shown in Fig. 6.9b. The corresponding temperatures are listed in Table 6.3. Note that the table results are highlighted in grey for the experimentally measured limit flow rates (see Table 6.2).

Table 6.3 shows that the tape has a local hotspot where $\theta_C$ is measured. This means the tape is overheating in the region where the PUR separator was placed, even if most of the channel is kept at lower temperatures. The consequence of this localized quench (and hot spot) is that the cooling fluid will start evaporating if the flow rate is not high enough to prevent heating above 77 K. Note also that this quench decreases the admissible critical temperature and generates higher losses, eventually quenching the whole tape, as seen experimentally.

These results validate the thermal model since the model determined limit velocity, which can dissipate the HTS losses for the imposed current without causing the evaporation of the liquid nitrogen in the channel, corresponding to the same limit value determined experimentally. This shows that the model can effectively be used to determine the working conditions that maintain the temperature of the superconducting tape constant, depending on the losses of the tape, even for complex geometries where hotspots can arise.

Table 6.3: Thermal model temperature results for the HTS coil in the PUR cryostat.

| $I_{RMS}$ (A) | inflow velocity (m/s) | $\theta_A$ (K) | $\theta_B$ (K) | $\theta_C$ (K) |
|---|---|---|---|---|
| 155 | 0,10 | 75,282 | 75,755 | 78,633 |
| | 0,15 | 75,191 | 75,508 | 78,656 |
| | 0,25 | 75,116 | 75,307 | 76,876 |
| | 0,30 | 75,097 | 75,257 | 76,455 |
| | 0,35 | 75,083 | 75,22 | 76,189 |
| 175 | 0,10 | 75,318 | 75,836 | 79,86 |
| | 0,20 | 75,164 | 75,425 | 79,313 |
| | 0,30 | 75,111 | 75,285 | 77,402 |
| | 0,40 | 75,084 | 75,214 | 76,522 |
| | 0,50 | 75,067 | 75,172 | 76,052 |
| 235 | 0,30 | 75,279 | 75,626 | 87,647 |
| | 0,40 | 75,212 | 75,474 | 82,22 |
| | 0,50 | 75,171 | 75,38 | 79,703 |
| | 0,60 | 75,143 | 75,318 | 78,355 |
| | 0,70 | 75,123 | 75,273 | 77,557 |

## 6.3 Summary

This Chapter presented a thermal model to complement the electromagnetic HTS performance estimation tools developed throughout the thesis. The thermal formulation was stated, and the slot thermal model was developed, providing a full methodology to estimate the cooling requirements of armature superconducting coils in electrical rotating machines. The thermal model results were compared to experimental measurements, showing good agreement and thus validating the methodology.

# Chapter 7

# Conclusions and Future work

## 7.1 Conclusions

This thesis investigated methods for characterising and simulating superconductors in complex electromagnetic devices such as electrical machines. The work was mainly focused on developing accurate, fast models for loss estimation on superconducting windings applied in axial flux machines, which, due to their complex geometry and magnetic flux distribution, require 3D models. The studies aimed to provide machine designers with efficient tools to estimate superconducting coil losses and evaluate their applicability in the armature windings of AFPM machines, where they are subject to alternate currents and AC magnetic stray flux, conditions which inevitably lead to non-negligible losses in superconductors.

The research was initially directed at experimentally describing HTS tapes and ferromagnetic materials at cryogenic temperatures to develop accurate calibration methods for the developed FEM models. Ferromagnetic samples were tested at ambient and cryogenic temperatures, and their loss densities were measured and compared with their ambient temperature behaviour. The materials manifest higher losses, due to increased conductivity in low temperature operation, and therefore their measured loss densities and BH curves were applied to model the iron cores of AFPM machines in COMSOL Multiphysics. Experiments in DC and AC operation conditions were performed in superconducting REBCO tapes to observe their resistive and hysteretic behaviour and estimate their losses with the $T-A$ formulation. Analytical and FEM models were developed and experimentally verified to calculate transport current losses in HTS in the high current or high frequency regime where the impact and loss of the remaining materials in the HTS tapes must be taken into account, either due to the current saturation in the superconducting material or due to the skin effect occurring in the remaining layers of the superconducting tape. Two distinct case study AFPM machines were designed to estimate working conditions and losses in HTS coils inserted in its armature windings. Due to the high computational demand of the HTS models when applied to a 3D model of the case study rotating machine, two equivalent slot models were developed for more expedited analyses. These models were successfully implemented in a 2D environment, significantly reducing the computational time for loss estimation of the superconducting coils operating in the AFPM armature windings. The models were validated with analytical solutions for superconductors subject to alternate applied fields and currents, showing coherent results between FEM and analytical models. A 3D model was also developed through a similar methodology as that of the 2D slot model which is also considerably more efficient than full electrical rotating machine simulations.

The slot model was applied to estimate losses for different types of HTS conductors, such as SCSC cables and compare them with REBCO windings and to verify the applicability and losses of different conductors in the machine armature windings. The advantages of the different HTS conductors were highlighted, and their applicability in machine AC windings was demonstrated. To better estimate the cooling requirement of HTS armature coils, a thermal model was proposed and preliminarily validated on a simplified experimental setup, to estimate the conditions that ensure sufficient cooling on the superconductors such that they operate in non-critical conditions.

## 7.2 Future work

This thesis proposes a methodology for accurate estimation of superconducting losses, which can work as a tool for developing electrical machines with superconductors. It goes without saying that to reach the prototyping stage of any type of superconducting electrical machine, optimization methods must be implemented together with the developed methodology, and different machine topologies, such as air-core machines and radial flux machines, should be investigated. Furthermore, operating temperature, fluid, and cryostat design will be essential in reaching a feasible and reliable prototype, for which the thermal model can be used for initial estimations.

Different approaches should be analysed during the machine design phase to mitigate losses of HTS inserted in alternate regimes without compromising the efficiency of the machine. The cooling requirements and performance investigation should be carried out for different materials and HTS conductor types such as striated coated conductors, CORC cables, $MgB_2$, 1G BSCCO tapes, among others. Specific solutions can also be investigated, such as different placement of HTS conductors inside the armature slots. The impact of the addition of ferromagnetic and conducting materials to act as flux diverters and shields in the vicinity of the superconducting materials should be investigated to evaluate their applicability to mitigate the effects of magnetic fields surrounding the superconductors.

Experimental tests of superconducting coils subject to alternate magnetic fields and supplied with AC currents simultaneously should be performed to further validate slot model results and more comprehensively describe the superconducting behaviour operating in rotating electrical machines. To further validate the multilayered FEM and analytical loss models proposed in this work, experiments ought to be performed in superconducting tapes operating in an overcritical regime to measure both their DC and AC characteristics. Alternatively, a setup for measuring magnetization losses at different frequencies can also be constructed to verify the influence of the remaining conducting layers in HTS tapes at different supply frequencies.

Since the HTS materials are highly sensitive to strain, the support for the HTS windings should be carefully considered due to the high current densities and magnetic fields in electrical machines, which can cause large forces and might lead to damaging the superconducting coils. Monitoring systems for superconducting machines and power electronics should be investigated for cryogenic operation to guarantee a reliable design.

# References

[1] Yasha Nikulshin, Shuki Wolfus, Vladimir Ginodman, Alex Friedman, Matteo Tropeano, Gianni Grasso, and Yosef Yeshurun. Ac losses in mgb2 wires and tapes in frequencies up to 18 khz. *IEEE Transactions on Applied Superconductivity*, 28(4):1–4, 2018.

[2] D.C. Larbalestier. The road to conductors of high temperature superconductors: 10 years do make a difference! *IEEE Transactions on Applied Superconductivity*, 7(2):90–97, 1997.

[3] Swarn Kalsi, Rod Badcock, J. Storey, Kent Hamilton, and Zhenan Jiang. Motors employing rebco corc and mgb2 superconductors for ac stator windings. *IEEE Transactions on Applied Superconductivity*, PP:1–1, 09 2021.

[4] João Arnaud, João F. P. Fernandes, and Paulo J. Costa Branco. Modifying the pulsed-field-magnetization technique for hts bulks in electrical machines without magnetic field sensors. *IEEE Transactions on Applied Superconductivity*, 28(4):1–4, 2018.

[5] Y J Hwang, M C Ahn, T S Lee, W S Lee, and T K Ko. Experimental study of the effects of alternating fields on hts coils according to the winding insulation conditions. *Superconductor Science and Technology*, 26(8):085021, jul 2013.

[6] B Dolisy, S Mezani, T Lubin, and J Lévêque. Fabrication and test of an axial-field hts rotating machine with integrated magnetic coupling. *Superconductor Science and Technology*, 30(3):035015, feb 2017.

[7] A Colle, T. Lubin, S. Ayat, O. Gosselin, and J. Leveque. Test of a flux modulation superconducting machine for aircraft. *Journal of Physics: Conference Series*, 1590(1):012052, jul 2020.

[8] Toshiyuki Yanamoto, Mitsuru Izumi, Katsuya Umemoto, Tamami Oryu, Youhei Murase, and Masahide Kawamura. Load test of 3-mw hts motor for ship propulsion. *IEEE Transactions on Applied Superconductivity*, 27(8):1–5, 2017.

[9] Anup Patel, Algirdas Baskys, Simon C. Hopkins, Vladislav Kalitka, Alexander Molodyk, and Bartek A. Glowacki. Pulsed-field magnetization of superconducting tape stacks for motor applications. *IEEE Transactions on Applied Superconductivity*, 25(3):1–5, 2015.

[10] Timing Qu, Peng Song, Xiaoyu Yu, Chen Gu, Longnian Li, Xiaohang Li, Dewen Wang, Boping Hu, Duxing Chen, Pan Zeng, and Zhenghe Han. Development and testing of a 2.5 kw synchronous generator with a high temperature superconducting stator and permanent magnet rotor. *Superconductor Science and Technology*, 27(4):044026, mar 2014.

[11] Giuseppe Messina, Edoardo Tamburo De Bella, and Luigi Morici. Hts axial flux permanent magnets electrical machine prototype: Design and test results. *IEEE Transactions on Applied Superconductivity*, 29(5):1–5, 2019.

[12] Taketsune Nakamura, Masaaki Yoshikawa, Ken-ichi Ikeda, Tomoharu Karashima, Takuro Ogasa, Ryohei Nishino, Yoshitaka Itoh, Toshihisa Terazawa, Mitsuho Furuse, and Satoshi Fukui. Load test and variable speed control of a 50-kw-class fully superconducting induction/synchronous motor for transportation equipment. *IEEE Transactions on Applied Superconductivity*, 29(5):1–5, 2019.

[13] João F P Fernandes, Luís F D Bucho, F Ferreira da Silva, Inês S P Peixoto, Silvio Vaschetto, and P J Costa Branco. Alternative analytical models for hts tapes considering their ac hysteretic and resistive losses. *Superconductor Science and Technology*, 37(3):035004, jan 2024.

[14] European Commission and Directorate-General for Climate Action. *Going climate-neutral by 2050 – A strategic long-term vision for a prosperous, modern, competitive and climate-neutral EU economy*. Publications Office, 2019.

[15] European Commission, Directorate-General for Mobility, Transport, Directorate-General for Research, and Innovation. *Flightpath 2050 – Europe's vision for aviation – Maintaining global leadership and serving society's needs*. Publications Office, 2011.

[16] I Marino, A Pujana, G Sarmiento, S Sanz, J M Merino, M Tropeano, J Sun, and T Canosa. Lightweight mgb2 superconducting 10 mw wind generator. *Superconductor Science and Technology*, 29(2):024005, dec 2015.

[17] Mustafa Farhadi and Osama Mohammed. Energy storage technologies for high-power applications. *IEEE Transactions on Industry Applications*, 52(3):1953–1961, 2016.

[18] Yessica Arellano-Prieto, Elvia Chavez-Panduro, Pierluigi Salvo Rossi, and Francesco Finotti. Energy storage solutions for offshore applications. *Energies*, 15(17), 2022.

[19] João F. P. Fernandes, Pedro P. C. Bhagubai, and Paulo J. C. Branco. Recent developments in electrical machine design for the electrification of industrial and transportation systems. *Energies*, 15(17), 2022.

[20] S. R. Trout and S. Constantinides. Using permanent magnets at low temperature. *Tech. Rep. TN 0302, Arnold Magnetic Technologies*, 2015.

[21] Ai Chengliu, Huang Yuanfeng, and Wang Haifeng. Main losses study of cryogenic induction motor for submerged liquid natural gas pump. In *2015 18th International Conference on Electrical Machines and Systems (ICEMS)*, pages 133–136, 2015.

[22] Marco Biasion, F. P. João Fernandes, Paulo José da Costa Branco, Silvio Vaschetto, Andrea Cavagnino, and Alberto Tenconi. A comparison of cryogenic-cooled and superconducting electrical machines. In *2021 IEEE Energy Conversion Congress and Exposition (ECCE)*, pages 4045–4052, 2021.

[23] Hui Min Kim, Ki Wook Lee, Do Gyun Kim, Jong Hoon Park, and Gwan Soo Park. Design of cryogenic induction motor submerged in liquefied natural gas. *IEEE Transactions on Magnetics*, 54(3):1–4, 2018.

[24] Marco Biasion, João F. P. Fernandes, Silvio Vaschetto, Andrea Cavagnino, and Alberto Tenconi. Superconductivity and its application in the field of electrical machines. In *2021 IEEE International Electric Machines & Drives Conference (IEMDC)*, pages 1–7, 2021.

[25] Donald Gubser. Superconductivity: An emerging power-dense energy-efficient technology. *Applied Superconductivity, IEEE Transactions on*, 14:2037 – 2046, 01 2005.

[26] Swarn Kalsi, Konrad Weeber, H. Takesue, C. Lewis, H.-W Neumueller, and R.D. Blaugher. Development status of rotating machines employing superconducting field windings. *Proceedings of the IEEE*, 92:1688 – 1704, 11 2004.

[27] R.M. Scanlan, A.P. Malozemoff, and D.C. Larbalestier. Superconducting materials for large scale applications. *Proceedings of the IEEE*, 92(10):1639–1654, 2004.

[28] S. S. Kalsi. *Applications of High Temperature Superconductors to Electric Power Equipment*. New Jersey, US: John Wiley & Sons, 2011.

[29] M. K. Wu, J. R. Ashburn, C. J. Torng, P. H. Hor, R. L. Meng, L. Gao, Z. J. Huang, Y. Q. Wang, and C. W. Chu. Superconductivity at 93 k in a new mixed-phase y-ba-cu-o compound system at ambient pressure. *Phys. Rev. Lett.*, 58:908–910, Mar 1987.

[30] David C. Larbalestier and Paul C. Canfield. Superconductivity at 100—where we've been and where we're going. *MRS Bulletin*, 36:590–593, 2011.

[31] Gustavo Sarmiento, Santiago Sanz, Ainhoa Pujana, Jose María Merino, Iker Marino, Matteo Tropeano, Davide Nardelli, and Gianni Grasso. Design and testing of real-scale mgb2 coils for suprapower 10-mw wind generators. *IEEE Transactions on Applied Superconductivity*, 26(3):1–6, 2016.

[32] Xiaowei Song, Carsten Buhrer, Anders Molgaard, Rasmus S. Andersen, Patrick Brutsaert, Markus Bauer, Jesper Hansen, Anders V. Rebsdorf, Jurgen Kellers, Tiemo Winkler, Anne Bergen, Marc Dhalle, Sander Wessel, Marcel ter Brake, Jan Wiezoreck, Hans Kyling, Hermann Boy, and Eric Seitz. Commissioning of the world's first full-scale mw-class superconducting generator on a direct drive wind turbine. *IEEE Transactions on Energy Conversion*, 35(3):1697–1704, September 2020.

[33] Vicente Climente-Alarcon, Anis Smara, Anup Patel, Bartek A. Glowacki, Algirdas Baskys, and Thomas Reis. Magnetization and losses for an improved architecture of trapped-flux superconducting rotor. *Journal of Propulsion and Power*, 36(1):101–108, 2020.

[34] Wolfgang Stautner, Phillip J. Ansell, and Kiruba S. Haran. Cheeta: An all-electric aircraft takes cryogenics and superconductivity on board: Combatting climate change. *IEEE Electrification Magazine*, 10(2):34–42, 2022.

[35] Justin S. Gray, John T. Hwang, Joaquim R. R. A. Martins, Kenneth T. Moore, and Bret A. Naylor. OpenMDAO: An open-source framework for multidisciplinary design, analysis, and optimization. *Structural and Multidisciplinary Optimization*, 59(4):1075–1104, April 2019.

[36] Hongye Zhang, Zezhao Wen, Francesco Grilli, Konstantinos Gyftakis, and Markus Mueller. Alternating current loss of superconductors applied to superconducting electrical machines. *Energies*, 14(8), 2021.

[37] Bárbara Maria Oliveira Santos, Fernando Jorge Monteiro Dias, Frederic Trillaud, Guilherme Gonçalves Sotelo, and Rubens de Andrade Junior. A review of technology readiness levels for superconducting electric machinery. *Energies*, 16(16), 2023.

[38] Mark Ainslie, Weijia Yuan, and T.J. Flack. Numerical analysis of ac loss reduction in hts superconducting coils using magnetic materials to divert flux. *Applied Superconductivity, IEEE Transactions on*, 23:4700104–4700104, 06 2013.

[39] Mingyang Wang, Min Zhang, Meng Song, Zhuyong Li, Fangliang Dong, Zhiyong Hong, and Zhijian Jin. An effective way to reduce ac loss of second-generation high temperature superconductors. *Superconductor Science and Technology*, 32(1):01LT01, nov 2018.

[40] Haran Karmaker, Dean Sarandria, Man Tak Ho, James Feng, Devdatta Kulkarni, and Gabriel Rupertus. High-power dense electric propulsion motor. *IEEE Transactions on Industry Applications*, 51(2):1341–1347, 2015.

[41] Swarn Kalsi, Kent Hamilton, Robert George Buckley, and Rodney Alan Badcock. Superconducting ac homopolar machines for high-speed applications. *Energies*, 12(1), 2019.

[42] Calvin C.T. Chow, Mark D. Ainslie, and K.T. Chau. High temperature superconducting rotating electrical machines: An overview. *Energy Reports*, 9:1124–1156, 2023.

[43] Inês S. P. Peixoto, F. Ferreira da Silva, João F. P. Fernandes, Silvio Vaschetto, and Paulo J. Costa Branco. A distributed equivalent-permeability model for the 3-d design optimization of bulk superconducting electromechanical systems. *IEEE Transactions on Applied Superconductivity*, 33(6):1–10, 2023.

[44] D J Gameiro Carvalho, F Ferreira da Silva, J F P Fernandes, and P J da Costa Branco. Finite-element recipes for hts-coated conductors and hts tape topologies. *Superconductor Science and Technology*, 36(10):103001, sep 2023.

[45] Luning Hao, Fangliang Dong, Jintao Hu, Qi Wang, Haigening Wei, Ismail Patel, Adil Shah, Yuyang Wu, and Tim Coombs. 3d electromagnetic modelling for high-temperature superconducting dynamo flux pumps using t-a formulation. *High Voltage*, n/a(n/a), 2024.

[46] Inês S. P. Peixoto, Sofia Viarengo, João F. P. Fernandes, Fabio Freschi, Laura Savoldi, and Silvio Vaschetto. Electromagnetic modeling of the copper layers influence for ac losses in rebco coated conductors based on t-a formulation. *IEEE Transactions on Applied Superconductivity*, 35(5):1–5, 2025.

[47] Inês S.P. Peixoto, Yusuke Sogabe, João F. P. Fernandes, Silvio Vaschetto, and Naoyuki Amemiya. Mitigation of superconducting ac losses in axial flux synchronous machines with multifilament coated superconductors. *IEEE Transactions on Applied Superconductivity*, 35(5):1–5, 2025.

[48] Marco Biasion, Ines S. P. Peixoto, Joao F. P. Fernandes, Silvio Vaschetto, Gerd Bramerdorfer, and Andrea Cavagnino. Iron loss characterization in laminated cores at room and liquid nitrogen temperature. In *2022 IEEE Energy Conversion Congress and Exposition (ECCE)*, pages 1–8, 2022.

[49] Inês S. P. Peixoto, Silvio Vaschetto, João F. P. Fernandes, Paulo J. Da Costa Branco, Alberto Tenconi, and Andrea Cavagnino. Modeling approach for superconducting ac windings: Case study on axial flux pm machines. In *2023 IEEE Energy Conversion Congress and Exposition (ECCE)*, pages 3790–3795, 2023.

[50] Abdallah Uosef, Lorenzo Mantione, Marco Bassani, Ines Peixoto, Lucia Frosini, Carlo Concari, and Silvio Vaschetto. Superconducting ac machines and cryogenic power electronics for reliable and power-dense energy conversion. In *2024 International Conference on Electrical Machines (ICEM)*, pages 1–8, 2024.

[51] Inês S. P. Peixoto, Lorenzo Perilli, Federica Graffeo, João F. P. Fernandes, Paulo J. da Costa Branco, and Silvio Vaschetto. A slot model for loss estimation in superconducting ac electrical machine windings. In *2024 International Conference on Electrical Machines (ICEM)*, pages 1–7, 2024.

[52] D. Breyel, T. L. Schmidt, and A. Komnik. Rydberg crystallization detection by statistical means. *Phys. Rev. A*, 86:023405, Aug 2012.

[53] H. K. Onnes. Further experiments with liquid helium. on the change of electric resistance of pure metals at very low temperatures, etc. iv. the resistance of pure mercury at helium temperatures. *Communications from the Physical Laboratory of the University of Leiden*, 133a:3, 1913.

[54] H. K. Onnes. Further experiments with liquid helium. on the change of electric resistance of pure metals at very low temperatures, etc. iv. the resistance of pure mercury at helium temperatures. 133b:29, 1913.

[55] Walther Meissner and Robert Ochsenfeld. Ein neuer effekt bei eintritt der supraleitfähigkeit. *Naturwissenschaften*, 21:787–788, 1933.

[56] F. London, H. London, and F. A. Lindemann. The electromagnetic equations of the supraconductor. *Proceedings of the Royal Society of London. Series A - Mathematical and Physical Sciences*, 149(866):71–88, 1935.

[57] J. Bardeen, L. N. Cooper, and J. R. Schrieffer. Theory of superconductivity. *Phys. Rev.*, 108:1175–1204, Dec 1957.

[58] A.A. Abrikosov. The magnetic properties of superconducting alloys. *The Journal of physics and chemistry of solids*, 2(3):199–208, 1957.

[59] CERN. *CAS - CERN Accelerator School : Superconductivity in Particle Accelerators: Hamburg, Germany 17 - 24 May 1995. CAS - CERN Accelerator School : Superconductivity in Particle Accelerators*, Geneva, 1996. CERN.

[60] A. A. Abrikosov. Nobel lecture: Type-ii superconductors and the vortex lattice. *Rev. Mod. Phys.*, 76:975–979, Dec 2004.

[61] A.A. Abrikosov. The magnetic properties of superconducting alloys. *Journal of Physics and Chemistry of Solids*, 2(3):199–208, 1957.

[62] David Larbalestier, Alex Gurevich, D. Feldmann, and A. Polyanskii. High-tc superconducting materials for electric power applications. *Nature*, 414(3):368–77, 12 2001.

[63] Mohammad Yazdani-Asrami, Alireza Sadeghi, and Milind D. Atrey. Selecting a cryogenic cooling system for superconducting machines: General considerations for electric machine designers and engineers. *International Journal of Refrigeration*, 140:70–81, 2022.

[64] Rainer Wesche. *Physical Properties of High-Temperature Superconductors*. 05 2015.

[65] F Gömöry, J Šouc, M Vojenčiak, E Seiler, B Klinčok, J M Ceballos, E Pardo, A Sanchez, C Navau, S Farinon, and P Fabbricatore. Predicting ac loss in practical superconductors. *Superconductor Science and Technology*, 19(3):S60, jan 2006.

[66] Naoyuki Amemiya and Z Jiang. A review on ac loss characteristics of high *t_c* superconductors. *Progress in Superconductivity and Cryogenics*, 8(4):1–7, 2006.

[67] Naoyuki Amemiya, Satoshi Kasai, Keiji Yoda, Zhenan Jiang, George A Levin, Paul N Barnes, and Charles E Oberly. Ac loss reduction of ybco coated conductors by multifilamentary structure. *Superconductor science and technology*, 17(12):1464–1471, 2004.

[68] Wilfred James Carr. Ac loss and macroscopic theory of superconductors. 2001.

[69] IEEE CSC & ESAS Superconductivity News Forum. Invited presentation 1s-p02 at the virtual cryogenics and superconductivity society of japan, 101st virtual spring meeting, May 2021. Presented at the 101st Virtual Spring Meeting, May 19-21, 2021, featured in the IEEE CSC & ESAS Superconductivity News Forum (Global Edition), December 2021.

[70] Samith Sirimanna, Thanatheepan Balachandran, Noah Salk, Jianqiao Xiao, Dongsu Lee, and Kiruba Haran. Electric propulsors for zero-emission aircraft: Partially superconducting machines. *IEEE Electrification Magazine*, 10:43–56, 06 2022.

[71] D Uglietti. A review of commercial high temperature superconducting materials for large magnets: from wires and tapes to cables and conductors. *Superconductor Science and Technology*, 32(5):053001, apr 2019.

[72] Xavier Obradors and Teresa Puig. Coated conductors for power applications: Materials challenges. *Superconductor Science and Technology*, 27:044003, 03 2014.

[73] Super Power Inc. 2G HTS Wire Specification. https://superpower-inc.com/specification.aspx, 2006., Accessed: Feb. 6, 2024.

[74] R Ries, F Gömöry, M Mošat', T Kujovič, C Hintze, and P Gil. Effect of off-axis bending on microstructural and transport properties of coated conductor tape. *Superconductor Science and Technology*, 36(1):014006, dec 2022.

[75] Naoyuki Amemiya, Yusuke Sogabe, Mao Shigemasa, Takuya Sobue, Takayuki Hirano, Satoshi Yamano, and Hisaki Sakamoto. Magnetization loss and current transport characteristics of scsc cables with metal cores. *IEEE Transactions on Applied Superconductivity*, 33(5):1–7, 2023.

[76] Yusuke Sogabe, Yudai Mizobata, and Naoyuki Amemiya. Coupling time constants and ac loss characteristics of spiral copper-plated striated coated-conductor cables (scsc cables). *Superconductor Science and Technology*, 33(5):055008, apr 2020.

[77] Mao Shigemasa, Yusuke Sogabe, Akira Takahashi, and Naoyuki Amemiya. Impact of number of layers on magnetization losses of spiral copper-plated multifilament coated conductors. *IEEE Transactions on Applied Superconductivity*, 33(5):1–6, 2023.

[78] D C van der Laan, J D Weiss, and D M McRae. Status of corc® cables and wires for use in high-field magnets and power systems a decade after their introduction. *Superconductor Science and Technology*, 32(3):033001, feb 2019.

[79] Naoyuki Amemiya, Mao Shigemasa, Akira Takahashi, Ning Wang, Yusuke Sogabe, Satoshi Yamano, and Hisaki Sakamoto. Effective reduction of magnetisation losses in copper-plated multifilament coated conductors using spiral geometry. *Superconductor science and technology*, 35(2):25003–, 2022.

[80] G Fuchs, S Gruss, P Verges, G Krabbes, K.-H Müller, J Fink, and L Schultz. High trapped fields in bulk ybco encapsulated in steel tubes. *Physica C: Superconductivity*, 372-376:1131–1133, 2002.

[81] J H Durrell, A R Dennis, J Jaroszynski, M D Ainslie, K G B Palmer, Y-H Shi, A M Campbell, J Hull, M Strasik, E E Hellstrom, and D A Cardwell. A trapped field of 17.6 t in melt-processed, bulk gd-ba-cu-o reinforced with shrink-fit steel. *Superconductor Science and Technology*, 27(8):082001, jun 2014.

[82] Giuseppe Messina, Mohammad Yazdani-Asrami, Fabrizio Marignetti, and Antonio della Corte. Characterization of hts coils for superconducting rotating electric machine applications: Challenges, material selection, winding process, and testing. *IEEE Transactions on Applied Superconductivity*, 31(2):1–10, 2021.

[83] Andrea Musso, Giuliano Angeli, Massimo Ascade, Marco Bocchi, Pier Luigi Ribani, Valerio Rossi, Angelo Valzasina, and Marco Breschi. Electrical characteristics of hts coils with and without insulation in a layer-wound configuration. *IEEE Transactions on Applied Superconductivity*, 31(5):1–5, 2021.

[84] Thibault Lécrevisse, Xavier Chaud, Philippe Fazilleau, Clément Genot, and Jung-Bin Song. Metal-as-insulation hts coils. *Superconductor Science and Technology*, 35(7):074004, may 2022.

[85] Seungyong HAHN, Kwangmin KIM, KIMKwanglok KIM, Haigun LEE, and Yukikazu IWASA. Current status of and challenges for no-insulation hts winding technique. *TEION KOGAKU (Journal of Cryogenics and Superconductivity Society of Japan)*, 53(1):2–9, 2018.

[86] G. Messina, L. Morici, U. Besi Vetrella, G. Celentano, M. Marchetti, R. Viola, and P. Sabatino. Ac loss measurements of a trapezoidal shaped hts coil using an electrical method. *International Journal of Superconductivity*, 2014(1):391329, 2014.

[87] Mitsuho Furuse, Masaaki Yoshikawa, Yoshitaka Itoh, Satoshi Fukui, and Taketsune Nakamura. Fabrication and testing of racetrack-shaped double-pancake coil for stator windings of induction-synchronous motor. *IEEE Transactions on Applied Superconductivity*, 25(3):1–4, 2015.

[88] Simon Otten, Anna Kario, Andrea Kling, and Wilfried Goldacker. Bending properties of different rebco coated conductor tapes and roebel cables at t=77 k. *Superconductor Science and Technology*, 29(12):125003, oct 2016.

[89] Justin J. Scheidler, Thomas Tallerico, Wesley A. Miller, and William Torres. *Progress Toward the Critical Design of the Superconducting Rotor for NASA's 1.4 MW High-Efficiency Electric Machine*.

[90] Weijia Yuan, M. D. Ainslie, W. Xian, Z. Hong, Y. Chen, Y. Yan, R. Pei, and T. A. Coombs. Theoretical and experimental studies on $j_c$ and ac losses of 2g hts coils. *IEEE Transactions on Applied Superconductivity*, 21(3):2441–2444, 2011.

[91] Hideaki Maeda and Yoshinori Yanagisawa. Recent developments in high-temperature superconducting magnet technology (review). *IEEE Transactions on Applied Superconductivity*, 24(3):1–12, 2014.

[92] Richard A. Matula. Electrical resistivity of copper, gold, palladium, and silver. *Journal of Physical and Chemical Reference Data*, 8:1147–1298, 1979.

[93] Jérôme Fleiter and Amalia Ballarino. In-field electrical resistance at 4.2 k of rebco splices. *IEEE Transactions on Applied Superconductivity*, 27(4):1–5, 2017.

[94] Refrigerating American Society of Heating and Inc. Air-Conditioning Engineers. 47.2.3.1 superconductivity, 2022.

[95] J G Hust and A B Lankford. Thermal conductivity of aluminum, copper, iron, and tungsten for temperatures from 1 k to the melting point:, 1984-01-01 05:01:00 1984.

[96] Luís F. D. Bucho, João F. P. Fernandes, Marco Biasion, Silvio Vaschetto, and Andrea Cavagnino. Experimental assessment of cryogenic cooling impact on induction motors. *IEEE Transactions on Energy Conversion*, 37(4):2629–2636, 2022.

[97] Anne Bergen, Rasmus Andersen, Markus Bauer, Hermann Boy, Marcel ter Brake, Patrick Brutsaert, Carsten Bührer, Marc Dhallé, Jesper Hansen, Herman ten Kate, Jürgen Kellers, Jens Krause, Erik Krooshoop, Christian Kruse, Hans Kylling, Martin Pilas, Hendrik Pütz, Anders Rebsdorf, Michael Reckhard, Eric Seitz, Helmut Springer, Xiaowei Song, Nir Tzabar, Sander Wessel, Jan Wiezoreck, Tiemo Winkler, and Konstantin Yagotyntsev. Design and in-field testing of the world's first rebco rotor for a 3.6 mw wind generator. *Superconductor Science and Technology*, 32(12):125006, oct 2019.

[98] Xiaowei Song, Carsten Bührer, Anders Mølgaard, Rasmus S. Andersen, Patrick Brutsaert, Markus Bauer, Jesper Hansen, Anders V. Rebsdorf, Jürgen Kellers, Tiemo Winkler, Anne Bergen, Marc Dhalle, Sander Wessel, Marcel ter Brake, Jan Wiezoreck, Hans Kyling, Hermann Boy, and Eric Seitz. Commissioning of the world's first full-scale mw-class superconducting generator on a direct drive wind turbine. *IEEE Transactions on Energy Conversion*, 35(3):1697–1704, 2020.

[99] Keitaro Muranaka, Taketsune Nakamura, Shinya Okajima, Takuro Ogasa, Naoyuki Amemiya, and Yoshitaka Itoh. Experimental and analytical studies on variable speed control of high-temperature superconducting induction/synchronous motor. *IEEE Transactions on Applied Superconductivity*, 26(4):1–5, 2016.

[100] K Umemoto, K Aizawa, M Yokoyama, K Yoshikawa, Y Kimura, M Izumi, K Ohashi, M Numano, K Okumura, M Yamaguchi, Y Gocho, and E Kosuge. Development of 1 mw-class hts motor for podded ship propulsion system. *Journal of Physics: Conference Series*, 234(3):032060, jun 2010.

[101] H W Neumüller, W Nick, B Wacker, M Frank, G Nerowski, J Frauenhofer, W Rzadki, and R Hartig. Advances in and prospects for development of high-temperature superconductor rotating machines at siemens. *Superconductor Science and Technology*, 19(3):S114, feb 2006.

[102] Gunar Klaus, Markus Wilke, Joachim Frauenhofer, Wolfgang Nick, and Heinz-Werner Neumuller. Design challenges and benefits of hts synchronous machines. In *2007 IEEE Power Engineering Society General Meeting*, pages 1–8, 2007.

[103] Masataka Iwakuma, Akira Tomioka, Masayuki Konno, Yoshiji Hase, Toshihiro Satou, Yoshihiro Iijima, Takashi Saitoh, Yutaka Yamada, Teruo Izumi, and Yuu Shiohara. Development of a 15 kw motor with a fixed ybco superconducting field winding. *IEEE Transactions on Applied Superconductivity*, 17(2):1607–1610, 2007.

[104] Masataka Iwakuma, Yoshiji Hase, Takehiro Satou, Akira Tomioka, Masayuki Konno, Yasuhiro Iijima, Takashi Saitoh, Yutaka Yamada, Teruo Izumi, and Yuh Shiohara. Production and test of a rebco superconducting synchronous motor. *IEEE Transactions on Applied Superconductivity*, 19(3):1648–1651, 2009.

[105] Vicente Climente-Alarcon, Anis Smara, Lukasz Tomkow, Bartek A. Glowacki, and Thomas Reis. Testing of surface mounted superconducting stacks as trapped-flux magnets in a synchronous machine. *IEEE Transactions on Applied Superconductivity*, 30(5):1–8, 2020.

[106] Anis Smara, Nikolay Mineev, Vicente Climente-Alarcon, Anup Patel, Algirdas Baskys, Bartek A Glowacki, and Thomas Reis. An experimental assessment of rotor superconducting stack demagnetization in a liquid nitrogen environment. *Superconductor Science and Technology*, 32(8):085009, jul 2019.

[107] Fernando Jorge Monteiro Dias, Guilherme Gonçalves Sotelo, Rubens de Andrade, and Frederic Trillaud. Response of a trapped flux superconducting motor to two drive methods. *IEEE Transactions on Applied Superconductivity*, 32(8):1–6, 2022.

[108] Zhen Huang, Min Zhang, Wei Wang, and T. A. Coombs. Trial test of a bulk-type fully hts synchronous motor. *IEEE Transactions on Applied Superconductivity*, 24(3):1–5, 2014.

[109] Kirill Modestov, Konstantin Kovalev, Alexander Dubensky, and Sergey Zhuravlev. Brushless nonsteel hts generator with combined excitation with trapped field plates on the rotor. *IEEE Transactions on Applied Superconductivity*, 28(4):1–5, 2018.

[110] António J. Arsénio, Francisco Ferreira da Silva, João F. P. Fernandes, and Paulo J. Costa Branco. Optimization of the guiding stability of a horizontal axis hts zfc radial levitation bearing. *Actuators*, 10(12), 2021.

[111] P. J. da Costa Branco and J. A. Dente. Design and experiment of a new maglev design using zero-field-cooled ybco superconductors. *IEEE Transactions on Industrial Electronics*, 59(11):4120–4127, 2012.

[112] Shengnan Zou, Víctor M R Zermeño, A Baskys, A Patel, Francesco Grilli, and B A Glowacki. Simulation and experiments of stacks of high temperature superconducting coated conductors magnetized by pulsed field magnetization with multi-pulse technique. *Superconductor Science and Technology*, 30(1):014010, nov 2016.

[113] Haran Karmaker, Dean Sarandria, Man Tak Ho, James Feng, Devdatta Kulkarni, and Gabriel Rupertus. High power dense electric propulsion motors. In *Industry Applications Society 60th Annual Petroleum and Chemical Industry Conference*, pages 1–7, 2013.

[114] Hidehiko Sugimoto, Teppei Tsuda, Takaya Morishita, Yoshinori Hondou, Toshio Takeda, Hiroyuki Togawa, Tomoya Oota, Kazuya Ohmatsu, and Shigeru Yoshida. Development of an axial flux type pm synchronous motor with the liquid nitrogen cooled hts armature windings. *IEEE Transactions on Applied Superconductivity*, 17(2):1637–1640, 2007.

[115] Yazid Statra, Hocine Menana, Bruno Douine, and Thierry Lubin. Axial-field synchronous machine with hts armature windings: Realization and preliminary tests. *IEEE Transactions on Applied Superconductivity*, 32(4):1–5, 2022.

[116] I. Muta, H. Tsukiji, T. Hoshino, and E. Mukai. Electrical characteristics of fully superconducting synchronous generator in persistent excitation mode. *IEEE Transactions on Magnetics*, 28(1):434–437, 1992.

[117] Jungwook Sim, Myungjin Park, H. Lim, G. Cha, Junkeun Ji, and Jikwang Lee. Test of an induction motor with hts wire at end ring and bars. *IEEE Transactions on Applied Superconductivity*, 13(2):2231–2234, 2003.

[118] Jungwook Sim, Kwangyoun Lee, Guesso Cha, and Ji-Kwang Lee. Development of a hts squirrel cage induction motor with hts rotor bars. *IEEE Transactions on Applied Superconductivity*, 14(2):916–919, 2004.

[119] Taesoo Song, Akira Ninomiya, and Takeshi Ishigohka. Experimental study on induction motor with superconducting secondary conductors. *IEEE Transactions on Applied Superconductivity*, 17(2):1611–1614, 2007.

[120] Taketsune Nakamura, Yoshitaka Itoh, Masaaki Yoshikawa, Tatsuo Nishimura, Takuro Ogasa, Naoyuki Amemiya, Yoshimasa Ohashi, Satoshi Fukui, and Mitsuho Furuse. Tremendous enhancement of torque density in hts induction/synchronous machine for transportation equipments. *IEEE Transactions on Applied Superconductivity*, 25(3):1–4, 2015.

[121] Taketsune Nakamura, Tenghui Dong, Jun Matsuura, Takanobu Kiss, Kohei Higashikawa, Shigeru Sato, and Peihong Zhang. Experimental and theoretical study on power generation characteristics of 1 kw class fully high temperature superconducting induction/synchronous generator using a stator winding with a bending diameter of 20 mm. *IEEE Transactions on Applied Superconductivity*, 32(6):1–5, 2022.

[122] John H Durrell, Mark D Ainslie, Difan Zhou, Philippe Vanderbemden, Tom Bradshaw, Susannah Speller, Mykhaylo Filipenko, and David A Cardwell. Bulk superconductors: a roadmap to applications. *Superconductor Science and Technology*, 31(10):103501, sep 2018.

[123] Kiruba S. Haran, David Loder, Timothy O. Deppen, and Lijun Zheng. Actively shielded high-field air-core superconducting machines. *IEEE Transactions on Applied Superconductivity*, 26(2):98–105, 2016.

[124] Anjela Koblischka-Veneva, Michael R. Koblischka, Kévin Berger, Quentin Nouailhetas, Bruno Douine, Miryala Muralidhar, and Masato Murakami. Comparison of temperature and field dependencies of the critical current densities of bulk ybco, $mgb_2$, and iron-based superconductors. *IEEE Transactions on Applied Superconductivity*, 29(5):1–5, 2019.

[125] Tobias Dietl, Jörg Karger, K. Kaupe, Alfred Dr. Pfemeter, Phillip A. Weber, A. Zakrzewski, and Andreas Strohmayer. Polaris - design of liquid hydrogen turbo-electric transport aircraft. 2018.

[126] Joseph Palmer and Essam Shehab. Modelling of cryogenic cooling system design concepts for superconducting aircraft propulsion. *IET Electrical Systems in Transportation*, 6(3):170–178, 2016.

[127] Boyang Shen, Francesco Grilli, and Tim Coombs. Overview of h-formulation: A versatile tool for modeling electromagnetics in high-temperature superconductor applications. *IEEE Access*, 8:100403–100414, 2020.

[128] Wafa Ali Soomro, Youguang Guo, Haiyan Lu, Jianxun Jin, Boyang Shen, and Jianguo Zhu. Numerical investigation of high-temperature superconducting-coated-conductors subjected to rotating magnetic fields. *Solids*, 3(4):569–577, 2022.

[129] Min Zhang and T A Coombs. 3d modeling of high-tc superconductors by finite element software. *Superconductor Science and Technology*, 25(1):015009, dec 2011.

[130] Edgar Berrospe-Juarez, Frederic Trillaud, Víctor M R Zermeño, and Francesco Grilli. Advanced electromagnetic modeling of large-scale high-temperature superconductor systems based on h and t-a formulations. *Superconductor Science and Technology*, 34(4):044002, feb 2021.

[131] Solovyov Mykola and Gömöry Fedor. A–v formulation for numerical modelling of superconductor magnetization in true 3d geometry. *Superconductor Science and Technology*, 32(11):115001, sep 2019.

[132] Alexandre Arsenault, Frédéric Sirois, and Francesco Grilli. Implementation of the h-$\phi$ formulation in comsol multiphysics for simulating the magnetization of bulk superconductors and comparison with the h-formulation. *IEEE Transactions on Applied Superconductivity*, 31(2):1–11, 2021.

[133] Inês S. P. Peixoto, F. Ferreira da Silva, João F. P. Fernandes, and P. J. da Costa Branco. 3d equivalent space-varying permeability model of hts bulks for computation of electromagnetic forces. *IEEE Transactions on Applied Superconductivity*, 31(5):1–7, 2021.

[134] Edgar Berrospe-Juarez, Víctor M R Zermeño, Frederic Trillaud, and Francesco Grilli. Real-time simulation of large-scale hts systems: multi-scale and homogeneous models using the t–a formulation. *Superconductor Science and Technology*, 32(6):065003, apr 2019.

[135] Boyang Shen, Francesco Grilli, and Tim Coombs. Review of the ac loss computation for hts using h formulation. *Superconductor Science and Technology*, 33(3):033002, feb 2020.

[136] Naoyuki Amemiya, Shun ichi Murasawa, Nobuya Banno, and Kengo Miyamoto. Numerical modelings of superconducting wires for ac loss calculations. *Physica C: Superconductivity*, 310(1):16–29, 1998.

[137] S. Sugita and H. Ohsaki. Numerical analysis of ac losses in rebco thin film for coated conductor and fault current limiter. *Physica C: Superconductivity*, 392-396:1150–1155, 2003. Proceedings of the 15th International Symposium on Superconductivity (ISS 2002): Advances in Superconductivity XV. Part II.

[138] Felix Huber, Wenjuan Song, Min Zhang, and Francesco Grilli. The t-a formulation: an efficient approach to model the macroscopic electromagnetic behaviour of hts coated conductor applications. *Superconductor Science and Technology*, 35(4):043003, mar 2022.

[139] Tara Benkel, Mayraluna Lao, Yingzhen Liu, Enric Pardo, Simon Wolfstädter, Thomas Reis, and Francesco Grilli. T–a-formulation to model electrical machines with hts coated conductor coils. *IEEE Transactions on Applied Superconductivity*, 30(6):1–7, 2020.

[140] Alexandre Arsenault, Frédéric Sirois, and Francesco Grilli. Efficient modeling of high-temperature superconductors surrounded by magnetic components using a reduced h–$\phi$ formulation. *IEEE Transactions on Applied Superconductivity*, 31(4):1–9, 2021.

[141] C. P. Bean. Magnetization of hard superconductors. *Physical review letters*, 8(6):250–253, 1962.

[142] Charles P. Bean. Magnetization of high-field superconductors. *Reviews of Modern Physics (U.S.)*, 36(1):31–39, 1964.

[143] Ernst Helmut Brandt and Mikhail Indenbom. Type-ii-superconductor strip with current in a perpendicular magnetic field. *Phys. Rev. B*, 48:12893–12906, Nov 1993.

[144] Y. B. Kim, Charles F. Hempstead, and A. R. Strnad. Magnetization and critical supercurrents. *Physical Review*, 129:528–535, 1963.

[145] Y. B. Kim, C. F. Hempstead, and A. R. Strnad. Critical persistent currents in hard superconductors. *Physical review letters*, 9(7):306–309, 1962.

[146] P. W. Anderson. Theory of flux creep in hard superconductors. *Physical review letters*, 9(7):309–311, 1962.

[147] F. Gömöry. Improvement of the self-field critical current of a high-Tc superconducting tape by the edge cover from soft ferromagnetic material. *Applied Physics Letters*, 89(7):072506, 08 2006.

[148] Antonio Morandi. 2d electromagnetic modelling of superconductors. *Superconductor Science and Technology*, 25(10):104003, sep 2012.

[149] P. W. Anderson and Y. B. Kim. Hard superconductivity: Theory of the motion of abrikosov flux lines. *Rev. Mod. Phys.*, 36:39–43, Jan 1964.

[150] Hongye Zhang, Min Yao, Kevin Kails, Philip Machura, Markus Mueller, Zhenan Jiang, Ying Xin, and Quan Li. Modelling of electromagnetic loss in hts coated conductors over a wide frequency band. *Superconductor Science and Technology*, 33(2):025004, jan 2020.

[151] Masahiro Nii, Naoyuki Amemiya, and Taketsune Nakamura. Three-dimensional model for numerical electromagnetic field analyses of coated superconductors and its application to roebel cables. *Superconductor Science and Technology*, 25(9):095011, jul 2012.

[152] H. Tsuboi and K. Kunisue. Eddy current analysis of thin plates taking account of the source current distributions and its experimental verifications. *IEEE Transactions on Magnetics*, 27(5):4020–4023, 1991.

[153] Katsutoku Takeuchi, Naoyuki Amemiya, Taketsune Nakamura, Osamu Maruyama, and Takeshi Ohkuma. Model for electromagnetic field analysis of superconducting power transmission cable comprising spiraled coated conductors. *Superconductor Science and Technology*, 24(11):119501, oct 2011.

[154] Leonid Prigozhin. Solution of thin film magnetization problems in type-ii superconductivity. *Journal of Computational Physics*, 144(1):180–193, 1998.

[155] Huiming Zhang, Min Zhang, and Weijia Yuan. An efficient 3d finite element method model based on the t–a formulation for superconducting coated conductors. *Superconductor Science and Technology*, 30(2):024005, dec 2016.

[156] M. Sjostrom, B. Dutoit, and J. Duron. Equivalent circuit model for superconductors. *IEEE Transactions on Applied Superconductivity*, 13(2):1890–1893, 2003.

[157] Francesco Grilli, Enric Pardo, Antti Stenvall, Doan N. Nguyen, Weijia Yuan, and Fedor Gömöry. Computation of losses in hts under the action of varying magnetic fields and currents. *IEEE Transactions on Applied Superconductivity*, 24(1):78–110, 2014.

[158] Jiahui Zhu, Zhenyu Zhang, Huiming Zhang, Min Zhang, Ming Qiu, and Weijia Yuan. Electric measurement of the critical current, ac loss, and current distribution of a prototype hts cable. *IEEE Transactions on Applied Superconductivity*, 24(3):1–4, 2014.

[159] Jae-Ho Kim, Chul Han Kim, Gopal Iyyani, Jozef Kvitkovic, and Sastry Pamidi. Transport ac loss measurements in superconducting coils. *IEEE Transactions on Applied Superconductivity*, 21(3):3269–3272, 2011.

[160] Richard P. Feynman, Robert B. Leighton, and Matthew Sands. *The Feynman Lectures on Physics*. Addison-Wesley Pub. Co., Reading, Mass., 1963. Vols. 1-3, 1963-1965.

[161] W T Norris. Calculation of hysteresis losses in hard superconductors carrying ac: isolated conductors and edges of thin sheets. *Journal of Physics D: Applied Physics*, 3(4):489, apr 1970.

[162] Sofia Viarengo, Lucas Brouwer, Paolo Ferracin, Fabio Freschi, Nicolo’ Riva, Laura Savoldi, and Xiaorong Wang. A new coupled electrodynamic t – a and thermal model for the critical current characterization of high-temperature superconducting tapes and cables. *IEEE Access*, 11:107548–107561, 2023.

[163] Bertrand Dutoit, Francesco Grilli, and Frédéric Sirois. *Numerical Modeling of Superconducting Applications: Simulation of Electromagnetics, Thermal Stability, Thermo-Hydraulics and Mechanical Effects in Large-Scale Superconducting Devices*. World Scientific Publishing Company, 11 2022.

[164] Kiruba S Haran, Swarn Kalsi, Tabea Arndt, Haran Karmaker, Rod Badcock, Bob Buckley, Timothy Haugan, Mitsuru Izumi, David Loder, James W Bray, Philippe Masson, and Ernst Wolfgang Stautner. High power density superconducting rotating machines—development status and technology roadmap. *Superconductor Science and Technology*, 30(12):123002, nov 2017.

[165] Satoshi Fukui, Shogo Tsukamoto, Kazuki Nohara, Jun Ogawa, Takao Sato, and Taketsune Nakamura. Study on ac loss reduction in hts coil for armature winding of ac rotating machines. *IEEE Transactions on Applied Superconductivity*, 26(4):1–5, 2016.

[166] Satoshi Fukui, Jun Ogawa, Jun Takahashi, Yuta Kobu, Takao Sato, and Taketsune Nakamura. Study on ac loss characteristics of 3-phase hts coils with iron core and its reduction. *IEEE Transactions on Applied Superconductivity*, 29(5):1–5, 2019.

[167] Giulio De Donato, Fabio Giulii Capponi, and Federico Caricchi. Fractional-slot concentrated-winding axial-flux permanent-magnet machine with core-wound coils. *IEEE Transactions on Industry Applications*, 48(2):630–641, 2012.

[168] Yazid Statra, Hocine Menana, and Bruno Douine. 3d semi-analytical modeling and optimization of fully hts ironless axial flux electrical machines. *Physica C: Superconductivity and its Applications*, 574:1353660, 2020.

[169] Silvio Vaschetto, Alberto Tenconi, and Gerd Bramerdorfer. Sizing procedure of surface mounted pm machines for fast analytical evaluations. In *2017 IEEE International Electric Machines and Drives Conference (IEMDC)*, pages 1–8, 2017.

[170] Matías Jiménez Molina, Federica Graffeo, Silvio Vaschetto, Alberto Tenconi, and Andrea Cavagnino. Fast procedure for the electromagnetic sizing of axial flux pm motors. In *2024 International Conference on Electrical Machines (ICEM)*, pages 1–8, 2024.

[171] G. De Donato, F. Giulii Capponi, and F. Caricchi. Fractional-slot concentrated-winding axial-flux permanent magnet machine with core-wound coils. In *2010 IEEE Energy Conversion Congress and Exposition*, pages 1066–1073, 2010.

[172] ASTM International. Standard test method for alternating-current magnetic properties of toroidal core specimens using the voltmeter-ammeter-wattmeter method, 2018.

[173] Fausto Fiorillo. *Characterization and Measurement of Magnetic Materials*. Elsevier Academic Press, 2004.

[174] Andreas Krings and Juliette Soulard. Experimental characterization of magnetic materials for electrical machine applications. In *2015 IEEE Workshop on Electrical Machines Design, Control and Diagnosis (WEMDCD)*, pages 85–89, 2015.

[175] Runar Mellerud, Christian Hartmann, Casper Leonard Klop, Sindre Austad, and Jonas Kristiansen Nøland. Design of a power-dense aviation motor with a low-loss superconducting slotted armature. *IEEE Transactions on Applied Superconductivity*, 33(8):1–13, 2023.

[176] G. Bertotti, A. Boglietti, M. Chiampi, D. Chiarabaglio, F. Fiorillo, and M. Lazzari. An improved estimation of iron losses in rotating electrical machines. *IEEE Transactions on Magnetics*, 27(6):5007–5009, 1991.

[177] G. Bertotti. General properties of power losses in soft ferromagnetic materials. *IEEE Transactions on Magnetics*, 24(1):621–630, 1988.

[178] Naoyuki Amemiya, Zhenan Jiang, Yasuhiro Iijima, Kazuomi Kakimoto, and Takashi Saitoh. Total ac loss of ybco coated conductor carrying ac transport current in ac transverse magnetic field with various orientations. *Superconductor Science and Technology*, 17(8):983, jun 2004.

[179] A. Formisano, F. Marignetti, R. Martone, G. Masullo, A. Matrone, R. Quarantiello, and M. Scarano. Performance evaluation for a hts transformer. *IEEE Transactions on Applied Superconductivity*, 16(2):1501–1504, 2006.

[180] W.J. Carr and C.E. Oberly. Filamentary ybco conductors for ac applications. *IEEE Transactions on Applied Superconductivity*, 9(2):1475–1478, 1999.

[181] D. W. Hazelton and V. Selvamanickam. Superpower's ybco coated high-temperature superconducting (hts) wire and magnet applications. *Proceedings of the IEEE*, 97(11):1831–1836, 2009.

[182] Naoyuki Amemiya, Yifan Zhao, Xijie Luo, Guangwei Xu, Yang Li, and Yusuke Sogabe. Current-sharing between filaments and voltage – current characteristics of copper-plated multifilament coated conductors. *IEEE Transactions on Applied Superconductivity*, 32(6):1–5, 2022.

[183] Francesco Grilli and Anna Kario. How filaments can reduce ac losses in hts coated conductors: a review. *Superconductor Science and Technology*, 29(8):083002, jul 2016.

[184] Naoyuki Amemiya, Mao Shigemasa, Akira Takahashi, Ning Wang, Yusuke Sogabe, Satoshi Yamano, and Hisaki Sakamoto. Effective reduction of magnetisation losses in copper-plated multifilament coated conductors using spiral geometry. *Superconductor Science and Technology*, 35(2):025003, dec 2021.

[185] Yufan Yan, Peng Song, Wenrong Li, Jie Sheng, and Timing Qu. Numerical investigation of the coupling effect in corc cable with striated strands. *IEEE Transactions on Applied Superconductivity*, 30(4):1–5, 2020.

[186] Marco Casali. *Experimental Analysis and Numerical Simulation of Quench in Superconducting HTS Tapes and Coils*. PhD thesis, alma, Marzo 2014.

[187] António José Arsénio dos Santos Costa. *Conception, study, optimization, and prototyping of a horizontal axis HTS ZFC radial levitation bearing*. PhD thesis, January 2022.

[188] Xin Zhao, Jin Fang, Zhenan Jiang, Wenjuan Song, Nengwen Liu, Yuan Gao, Xiaohang Li, Fanhui Zeng, Yajun Xia, Rod A Badcock, Nicholas J Long, Mike P Staines, Robert G Buckley, Xinyu Fang, Yulong Li, Bo Liu, Jinyin Zhang, Wen Han, Li Li, Jin Wang, and Peiqing Gao. Design, development, and testing of a 6.6 mva hts traction transformer for high-speed train applications. *Superconductor Science and Technology*, 36(8):085009, jun 2023.

[189] Neil D. Glasson, Mike P. Staines, Zhenan Jiang, and Nathan S. Allpress. Verification testing for a 1 mva 3-phase demonstration transformer using 2g-hts roebel cable. *IEEE Transactions on Applied Superconductivity*, 23(3):5500206–5500206, 2013.

[190] A Dadhich, F Grilli, L Denis, B Vanderheyden, C Geuzaine, F Trillaud, D Sotnikov, T Salmi, G Hajiri, K Berger, T Benkel, G dos Santos, B M O Santos, F G R Martins, A Hussain, and E Pardo. Electromagnetic-thermal modeling of high-temperature superconducting coils with homogenized method and different formulations: a benchmark. *Superconductor Science and Technology*, 37(12):125006, nov 2024.

[191] Frank P. Incropera. *Fundamentals of Heat and Mass Transfer*. John Wiley & Sons, Inc., Hoboken, NJ, USA, 2006.

[192] Bruce R. Munson, Donald F. Young, Theodore H. Okiishi, and Wade W. Huebsch. *Fundamentals of Fluid Mechanics*. John Wiley & Sons, Hoboken, NJ, 7th edition, 2013.

[193] Inc. JAHM Software. Material property database: Mpdb software, 2024. Accessed: 2024-10-18.

[194] J Šouc, E Pardo, M Vojenčiak, and F Gömöry. Theoretical and experimental study of ac loss in high temperature superconductor single pancake coils. *Superconductor Science and Technology*, 22(1):015006, nov 2008.

# Appendix A

# Manufacturer REBCO Properties

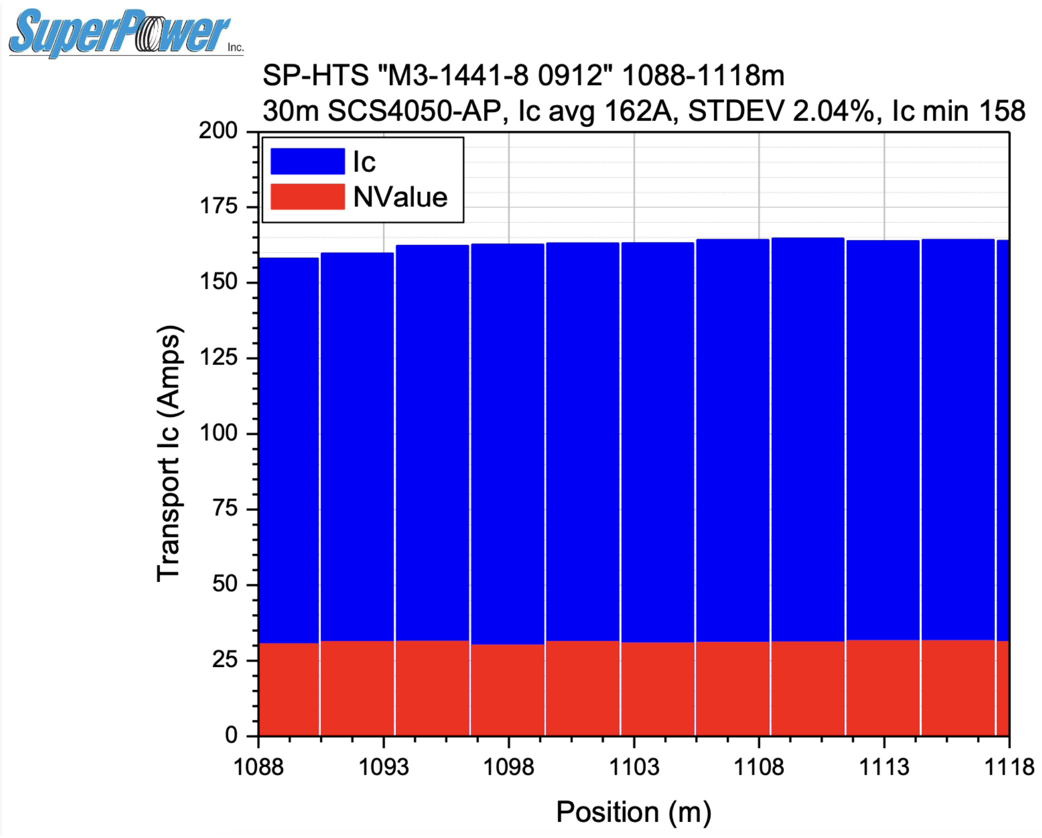

Fig. A.1 Superconducting critical parameters test as given by supplier (Superpower Inc.)